COMPARISON OF FIVE REGULARIZATION METHODS FOR THE SOLUTION OF INVERSE
ELECTROCARDIOGRAPHY PROBLEM

A THESIS SUBMITTED TO
THE GRADUATE SCHOOL OF NATURAL AND APPLIED SCIENCES
OF
MIDDLE EAST TECHNICAL UNIVERSITY

BY

ALPEREN GÜÇLÜ

IN PARTIAL FULLFILMENT OF THE REQUIREMENTS
FOR
THE DEGREE OF MASTER OF SCIENCE
IN
ELECTRICAL AND ELETRONICS ENGINEERING

FEBRUARY 2013

Approval of the thesis:

COMPARISON OF FIVE REGULARIZATION METHODS FOR THE SOLUTION OF INVERSE ELECTROCARDIOGRAPHY PROBLEM

submitted by **ALPEREN GÜÇLÜ** in partial fulfillment of the requirements for the degree of **Master of Science in Electrical and Electronics Engineering Department, Middle East Technical University** by,

Prof. Dr. Canan Özgen
Dean, Graduate School of **Natural and Applied Sciences** _____

Prof. Dr. İsmet Erkmen
Head of Department, **Electrical and Electronics Engineering** _____

Assoc. Prof. Dr. Yeşim Serinağaoğlu Doğrusöz
Supervisor, **Electrical and Electronics Engineering Dept., METU** _____

Examining Committee Members:

Prof. Dr. Murat Eyüboğlu
Electrical and Electronics Engineering Dept., METU _____

Assoc. Prof. Dr. Yeşim Serinağaoğlu Doğrusöz
Electrical and Electronics Engineering Dept., METU _____

Prof. Dr. Nevzat Güneri Gençer
Electrical and Electronics Engineering Dept., METU _____

Assoc. Prof. Dr. İlkay Ulusoy
Electrical and Electronics Engineering Dept., METU _____

Prof. Dr. Gerhard-Wilhelm Weber
Institute of Applied Mathematics, METU _____

Date: 11.02.2013

I hereby declare that all information in this document has been obtained and presented in accordance with academic rules and ethical conduct. I also declare that, as required by these rules and conduct, I have fully cited and referenced all material and results that are not original to this work.

Name, Last name   : ALPEREN GÜÇLÜ

Signature   :

ABSTRACT

COMPARISON OF FIVE REGULARIZATION METHODS FOR THE SOLUTION OF INVERSE ELECTROCARDIOGRAPHY PROBLEM

Güçlü, Alperen

M.S., Department of Electrical and Electronics Engineering

Supervisor: Assoc. Prof. Dr. Yeşim Serinağaoğlu Doğrusöz

September 2012, 84 pages

Understanding heart's electrical activity is very important because coronary problems -such as heart attacks, arrhythmia and stroke- are the leading cause of death in the world. Forward and inverse problems of electrocardiography (ECG) are methods that provide detailed information about the electrical activity of the heart. Forward problem of electrocardiography is the estimation of body surface potentials from equivalent cardiac sources. Inverse problem of electrocardiography can be described as estimation of the electrical sources in the heart using the potential measurements obtained from the body surface. Due to spatial smoothing and attenuation that occur within the thorax, inverse ECG problem is ill-posed and the transfer matrix is ill-conditioned. Thus, regularization is needed to find a stable and accurate solution. In this thesis, epicardial potentials used as equivalent cardiac sources to represent electrical activity of the heart and performances of five different regularization methods are compared. These regularization methods are Tikhonov regularization, truncated singular value decomposition, least squares QR factorization, truncated total least squares, and Lanczos truncated total least squares. Results are assessed qualitatively using correlation coefficient (CC) and relative difference measurement star (RDMS) measures. In addition, real and reconstructed surface potential distributions are compared qualitatively. Body surface potential measurements are simulated with different levels of measurement noise. Geometric errors are also included by changing the size and the location of the heart in the mathematical torso model. According to our test results, the performances of the regularization methods in solving the inverse ECG problem depend on the form and amount of the noise.

Keywords: Inverse electrocardiography problem, regularization

ÖZ

TERS ELEKTROKARDİYOGRAFİ PROBLEMİNİN ÇÖZÜMÜNDE BEŞ DEĞİŞİK
DÜZENLİLEŞTİRME YÖNTEMİNİN KARŞILAŞTIRILMASI

Güçlü, Alperen
Yüksek Lisans, Elektrik ve Elektronik Bölümü
Tez Yöneticisi: Doç. Dr. Yeşim Serinağaoğlu Doğrusöz

Eylül 2012, 84 sayfa

Kalp krizi, aritmi ve felç gibi koroner problemlerin dünyada önde gelen ölüm sebeplerinden olması nedeniyle kalbin elektriksel aktivitesinin anlaşılması çok önemlidir. İleri ve ters elektrokardiyografi (EKG) problemleri, kalbin elektriksel aktivitesi hakkında detaylı bilgi veren metotlardır. İleri EKG problemi, vücut yüzey potansiyellerinin eşdeğerli kardiyak kaynaklarından tahmin edilmesidir. Ters elektrokardiyografi problemi ise kalpteki elektriksel kaynakların tahmini için vücut yüzeyinden elde edilen potansiyel ölçümlerinin kullanılması olarak tanımlanabilir. Göğüs kafesinde meydana gelen yumuşama ve zayıflamadan dolayı, ters EKG problemi kötü konumlanmıştır ve transfer matrisi kötü durumdadır. Bundan dolayı sabit ve doğru bir çözüm bulmak için düzenlileştirme gerekmektedir. Bu tezde kalbin elektriksel aktivitesini temsil etmek için epikardiyal potansiyeller eşdeğer kardiyak kaynakları olarak kullanılmıştır ve beş farklı düzenlileştirme metodunun performansları karşılaştırılmıştır. Bunlar; TSVD, LSQR, TTLS, Lanczos TTLS ve Tikhonov düzenlileştirme metotlarıdır. Sonuçlar ilinti sayısı ve RDMS ölçümleri kullanılarak niteliksel olarak incelenmiştir. Ek olarak gerçek ve yeniden düzenlenmiş yüzey potansiyel dağılımları niteliksel olarak karşılaştırılmıştır. Vücut yüzey potansiyel ölçümleri değişik seviyedeki ölçüm gürültüleri ile simule edilmiştir. Ayrıca geometrik hata olarak, kalbin şekli ve matematiksel gövde modelindeki yeri değiştirilmiştir. Test sonuçlarımıza göre, ters EKG probleminin çözümünde, düzenlileştirme metotlarının performansları gürültünün şekline ve miktarına göre değişmektedir.

Anahtar Kelimeler: Ters elektrokardiyografi problemi, düzenlileştirme metotları

To My Family

ACKNOWLEDGEMENTS

TABLE OF CONTENTS

LIST OF TABLES

TABLES

LIST OF FIGURES

FIGURES

CHAPTER 1

INTRODUCTION

Heart is one of the most vital organs in our body; any disorder in heart functioning -such as heart attacks, stroke and arrhythmia- can result in death. According to World Health Organization (WHO) statistics, in middle-income and high-income countries heart diseases are the primary cause of death; in low-income countries, heart diseases ranked as the fourth most important reason of death [1]. All over the world, heart diseases are the main cause of death with 12.8% prevalence [1]. Thus, early diagnosis and treatment of heart diseases is very crucial.

A normal heart functions as a result of well-organized electrical activity, and pathologies of the heart result in deviations from this behavior. Thus, knowledge about the electrical activity of the heart is very essential for diagnosing heart disorders. Classical 12-lead electrocardiography (ECG) is one of the mostly used diagnostic tools for measuring the electrical activity of the heart. Cardiologists use features such as the rate of the measured signal and its shape to assess the electrical activity of the heart and to diagnose different cardiac illnesses. The main problems with this method are the Brody and respiration effects [2], smoothing and attenuation of cardiac signals due to inhomogeneities within the thorax and the low spatial resolution of cardiac electrical source projections recorded on the body surface by this method [3]. Thus, 12-lead ECG may result in incorrect or insufficient assessment of the electrical activity of the heart. To decrease these effects, catheters inserted into the cardiac veins or through the torso may be used to measure the electrical activity of the heart, but usage of catheters are limited due to highly invasive nature of this method.

An alternative method to overcome the low resolution weakness of the 12 lead ECG is the Body Surface Potential Mapping (BSPM) method [4]. BSPM uses 64 to 256 electrodes to measure the cardiac electrical activity on a larger part of torso than that covered by the 12 lead ECG method; thus providing a better representation of the electrical activity of the heart on the body surface. As a result, one major advantage of BSPM is that the entire chest surface is explored. Another advantage is that BSPM is more sensitive in detecting local electrical events [5]. However attenuation and smoothing effects are also present in the BSPM. To overcome this difficulty, researchers have pursued estimating cardiac electrical sources from the body surface potential maps (BSPMs). This problem can be studied in two main categories, the forward problem in which the body surface potentials resulting from equivalent cardiac sources are calculated. This yields a mathematical model of the relationship between the cardiac sources and the BSPMs. On the other hand, inverse problem of ECG is the estimation of equivalent cardiac sources from recorded BSPMs; the objective is to obtain high resolution images of heart's electrical activity.

The cardiac electrical activity can be modeled in terms of various equivalent source models; some of these equivalent sources are fixed dipole, moving dipole, multiple dipoles, multipoles, epicardial potential distributions, heart-surface activation isochrones, and the transmembrane potential distributions in the 3 dimensional myocardium. In this study, we focus on the inverse ECG problem in terms of epicardial potential distribution.

The inverse problem of electrocardiography is ill-posed which means that even small perturbations lead to serious errors in the solutions. Because of this ill-posedness, inverse ECG problem needs a regularization process in order to estimate the preferred solution. There are many different regularization and statistical estimation methods in literature used to solve the inverse ECG problem and to reconstruct the desired epicardial source distribution. Some of these regularization methods are Tikhonov regularization [6, 7, 8], Truncated Singular Value Decomposition (TSVD) [7, 9], Least Square-QR (LSQR) [10, 11], Truncated Total Least Squares (TTLS) [12, 13], Lanczos TTLS [13],

Multiple constraints approach [14], State space models [15, 16, 17, 18, 19], Bayesian Maximum a Posteriori (MAP) estimation [20, 21]and model based approaches [22, 23]. In this thesis, we have implemented the first four of these methods proposed in literature for inverse ECG solution. In addition to those methods, Lanczos TTLS method is also applied as a regularization method for inverse ECG problem and performance of Lanczos TTLS is compared with other methods. In literature, TTLS and LSQR are only compared with Tikhonov regularization or TSVD for the solution of Inverse ECG problem. The main motivation of this thesis is to compare performances of all of the five regularization methods that solve the inverse ECG problem by arranging and ignoring singular values of the transfer matrix.

1.1. Scope of the Thesis

In this thesis, performances of Tikhonov regularization, TSVD, TTLS, LSQR and Lanczos TTLS methods are compared under various noise scenarios that one can run into in clinical studies. Among these methods, LSQR, TTLS and Lanczos TTLS are implemented in MATLAB. These methods are compared with TSVD and Tikhonov regularization methods, which have already been implemented by Per Christian Hansen in his Regularization toolbox [24].

The noise conditions we have considered are the measurement noise and the geometric noise. Measurement noise is characterized as different levels of independent and identically distributed Gaussian noise and geometric errors are implemented as the shift in heart's location and change in the heart's size.

Each method has a 'regularization parameter' that needs to be optimized for best results. Therefore, we have implemented various regularization parameter selection methods to assess which parameter selection method should be preferred in each application. The regularization parameter selection methods we have implemented are maximum correlation coefficient approach, the L-curve method [88], the generalized cross validation (GCV) method [25, 26] and the composite residual smoothing operator (CRESO) [6, 27, 28].

Performances of the regularization methods and regularization parameter selection methods are compared quantitatively using Relative Difference Measurement Star (RDMS), and Correlation Coefficient (CC), And qualitatively using a scientific visualization application named Map3d developed by Utah Nora Eccles Harrison Cardiovascular Research and Training Institute [29].

1.2. Contributions of the Thesis

- The methods implemented and compared in this thesis are all based on arranging and ignoring singular values of the transfer matrix. They have been compared in literature in mostly pairs and sometimes triplets; however they have not been rigorously tested and compared under the same conditions. In this thesis, we achieve this goal by applying each method to data simulated under the same conditions and we assess strengths, weaknesses and limitations of each method.
- TTLS have been used to solve the inverse ECG problem before, however Lanczos TTLS, which is a computationally more efficient and less time consuming algorithm than TTLS, has not been applied to this problem.
- There have been studies for Tikhonov regularization that assess different regularization parameter selection algorithms [25, 26, 27, 30], however for the more recent methods such as the LSQR and the TTLS methods, there is no such evaluation. In this thesis, we include this comparison.

1.3. Outline of the Thesis

In this thesis, second chapter contains the background information about the electrocardiography and the methods evaluated in this thesis. In that chapter, first anatomy and physiology of the heart is given. Then, the forward and inverse problems of ECG are defined along with a literature survey on these topics.

In the third chapter, we present the definition of inverse problem of ECG. Then the theories of the methods included in our study are represented. These methods are Tikhonov regularization, TSVD, LSQR Method, TTLS and Lanczos TTLS.

The fourth chapter of this thesis is devoted to results and discussions. The performances of parameter selection methods, CRESO, GCV, L-curve and max CC methods are compared for the regularization methods. Then, Tikhonov regularization, TTLS, LSQR, Lanczos TTLS, TSVD methods are compared with each other for different noise levels.

In the last chapter, conclusions of this study and future work will be given.

CHAPTER 2

BACKGROUND INFORMATION

According to statistics, heart diseases are the main cause of death all over the world [5]. Fom this reason, understanding the heart's functions is an important research topic for engineering and medicine areas. In this chapter, we present the background and literature search on the heart's electrophysiology and understanding and obtaining its electrical source distribution. First,anatomy and electrophysiological properties of the heart will be explained, and then action potential generation and electrocardiography will be discussed. The source models representing electrical activity of heart will be considered. In the last part, the forward and inverse problems of ECG will be presented along with a detailed summary of past research carried out in these areas.

2.1. Anatomy of the Heart

The heart is the electro mechanical pump of the body, which pumps oxygen and nutrition rich blood to every part of the body. In a normal person, it weights between $250 - 350$ g. It is located anterior to the vertebral column and posterior to sternum. The heart is in a sac called pericardium. The pericardium has a double walled structure, which protects the heart and prevents overfilling with blood [31, 32].

Besides pericardium, the heart's outer wall has three layers:
- Epicardium is the outer layer of the heart wall and covers the heart. The potentials on epicardium are called epicardial potentials and generally used for modeling the electrical activity of the heart in the inverse and forward problems of electrocardiography.
- Myocardium is the muscular middle layer of the heart wall. Contraction of the myocardium pumps blood from the ventricles and relaxation of the myocardium helps the ventricles to receive the blood. The main aim of three dimensional electrocardiographical imaging is to determine the myocardial electrical activity.
- Endocardium is the inner layer of the heart wall. Since it is in contact with blood, endocaridum has a smooth surface to help blood flow. Endocardial potentials are also used as cardiac sources for electrocardiographical imaging.

The heart is mainly divided into four parts:
- Right ventricle is the lower right part of the heart, which receives blood from the right atria and pumps the blood to the lungs by main pulmonary artery. It is separated from the left ventricle by the ventricular septum.
- Left ventricle is the lower left part of the heart receiving blood from the left atria and pumps the blood to the whole body by aorta.
- Right atrium receives de-oxygenated blood from the body by superior and inferior venae. It is separated from the left atrium by the atrial septum.
- Left atrium is the upper left part of the heart, which receives oxygen rich blood from the lungs by pulmonary veins.

The heart has four valves to prevent backflow of blood:
- Aortic valve is located between the left ventricle and the aorta.
- Pulmonary valve is located between the right ventricle and the pulmonary artery.
- The mitral valve is between the left ventricle and the left atrium.
- The tricuspid valve is between the right ventricle and the right atrium.

5
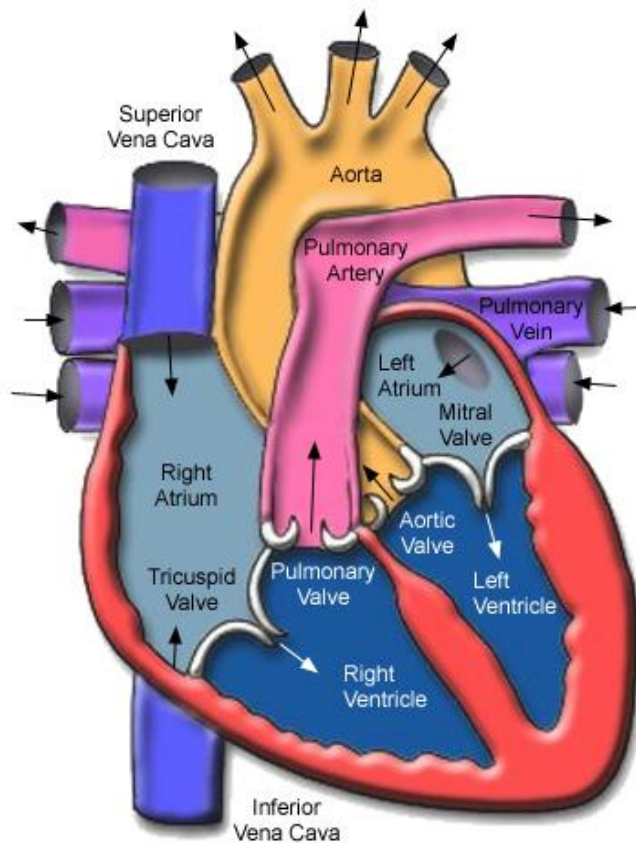
Figure 2.1: The anatomy of the heart and vessels [33]

These valves work only in one direction. The aortic and pulmonary valves prevent the backflow of blood from arteries to ventricles. The mitral and tricuspid valves permits blood to move from atria to ventricles but prevents flow in the opposite direction.

The heart works as a blood pump in the body. The right ventricle pumps oxygen poor blood to the lungs, then oxygenated blood returns to the left atrium from the lungs. This movement of blood is called pulmonary circulation. In systemic circulation, oxygen and nutrition rich blood is pumped from the left ventricle to the whole body and the de-oxygenated blood returns to the right atrium. Since in the systemic circulation the left heart sends blood to the whole body, left part of the heart wall is thicker and has a stronger muscular structure than the right part.

2.2. Action Potential Generation

Every cell in our body has mainly three parts: cytoplasm is a semi fluid part containing organelles, nucleus is the control center of the cell and the cell membrane is the outer boundary of cell. Cell membrane controls the entrance and exit of some materials. Cell membrane also allows ions to pass from different ion channels. Since ions are charged materials, cell membrane has an electrical potential. The cell membrane maintains a stable negative potential at rest and thus the cell membrane can be thought as a small battery. The transmembrane potential (TMP), which is the potential difference across the cell membrane, is given as:

$$V_m = \varphi_i - \varphi_e \tag{2.1}$$

where φ_i, and φ_e are the intracellular and the extracellular potentials, respectively.

Some cells in our body can reverse the negative potential across their cell membrane; these cells are called the excitable cells. This potential change is established by change of membrane permeability to certain ions and the corresponding change in potential is called the action potential. Muscle cells, heart cells and nerve cells are the excitable cells in our body. Different parts of heart muscles have

6

different action potential characteristics. Figure 2.2 shows the action potential characteristic of a ventricular myocyte [34].

The cardiac action potential has five phases [34, 35].

- Phase 4 is the period during which the cell remains at resting cell membrane potential. In this phase the heart is in the diastole period. Phase 4 ends when the cell is stimulated by an external electrical stimulus such as the adjacent cell. Some cells have the ability to depolarize spontaneously without external stimulus. They are called the pacemaker cells which are located at the Sinoatrial Node.
- Phase 0 is the rapid depolarization phase. When the stimulus reaches a threshold value, cell membrane opens fast sodium channels, so the sodium conductance in cell membrane increases. Because of inflow of the sodium ions, the cell membrane has a positive voltage.
- Phase 1 is the period during which fast sodium ion channels begin to close. At the same time, the cell loses potassium and chloride ions, and this loss causes the small downward deflection in the action potential.
- Phase 2 is the plateau phase. At plateau stage there is a balance between inward movement of calcium ions and outward movement of potassium ions.
- Phase 3 is the rapid repolarization phase. At this stage fast calcium channels are closed and there is an outward current because of the movement of potassium ions, causing negative membrane potential.
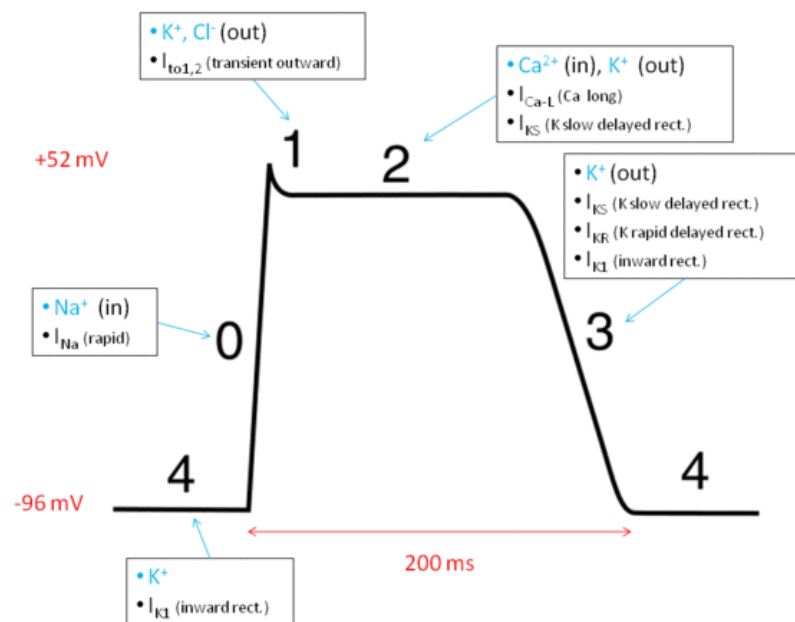
Figure 2.2: Action potential generated by a heart tissue [34]

2.3. Electrical Activity of the Heart

Heart has specialized cells which are capable of initiating electrical activity without another nerve supply. The electrical activity of the heart depends on a series of specialized cardiac cells as shown in Figure 2.3 [10]:

- **Sinoatrial Node** has self excitatory cells which are situated at the wall of the right atrium, close to the superior vena cava. Since SA cells determine the heart rate, they are called the heart's pacemakers. Contraction of heart starts by electrical activity of the SA node. The stimulation caused by the SA node is transferred to nearby cells and action potential is

generated at each cell. By this way, stimulation spreads through the right and the left atria, causing them to contract.

- **Atrioventricular node** is located between the right atrium and the right ventricle. Wave of electrical activity spreading from SA node reaches to the Atrioventricular node. Here, the speed of conduction decreases, so the transmission between atria and ventricles is delayed. This delay helps atria to finish its contraction before the ventricles are activated and most of the blood in the atria fills the ventricles.
- **Bundle of His** is a special conduction system between the AV node and the ventricles.
- **Left and Right Bundle branches** transmit impulses from the Bundle of His to the ventricles; transmission velocity increases here.
- **Purkinje fibers** spread cardiac electrical activity to ventricular myocytes and the heart's electrical conduction path finishes here. The velocity of propagation is higher at bundle branches and the Purkinje fibers to ensure that the electrical activity spreads immediately over the ventricles.

AV node and Purkinje fibers also have the ability to initiate APs, but the heart rate of a healthy heart is determined by the SA node.
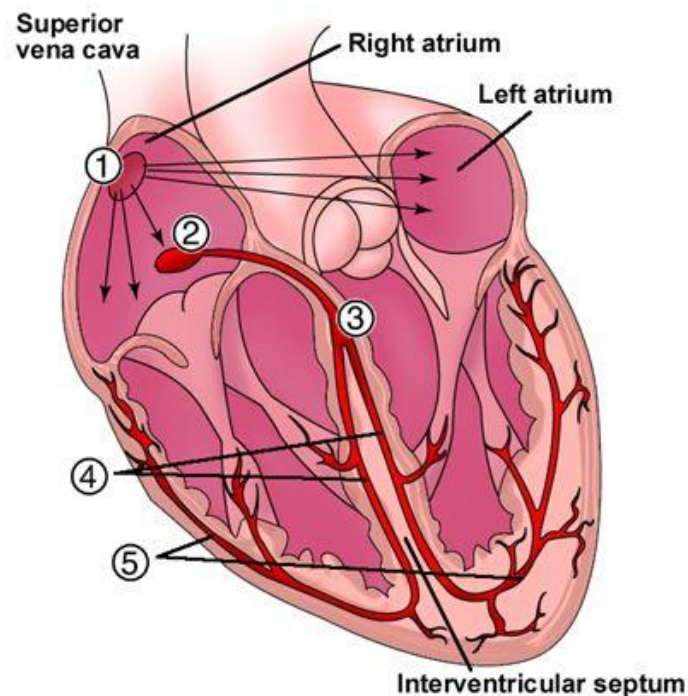
Figure 2.3: Cardiac Conduction System 1) Sinoatrial node (Pacemaker) 2) Atrioventricular node 3) Atrioventricular Bundle (Bundle of His) 4) Left & Right Bundle branches 5) Purkinje Fibers [35]

2.4. Electrocardiography

While describing the formation and the properties of the action potential, we concentrated on the cellular electrical activity of the heart muscle cells. In practice, this activity cannot be clinically measured from humans; only in-vitro laboratory experiments on tissue samples makes it possible to measure and study the action potentials. The electrical activity of all heart cells are recorded from body surface by a method called electrocardiography [36]. The most commonly used method is the classical 12-lead electrocardiography. The positions of the ten electrodes used in the 12-lead electrocardiography method are shown in Figure 2.4.

The recording produced by electrocardiography method is called electrocardiogram. A typical electrocardiogram is shown in Figure 2.5. Electrocardiogram is the superposition of electrical activity of different specialized cardiac cells as shown in Figure 2.6.

The electrocardiogram is composed of mainly three parts:

- P wave reflects the depolarization of left and right atriums. The depolarization of atria is triggered by the electrical activity of SA node. Atrial abnormalities cause changes in duration, amplitude or frequency of the P wave. In atrial fibrillation, the P wave disappears and replaced with an improper wave. The duration from the beginning of the P wave to start of QRS complex is called PR interval. This interval reflects the time for the atriums to depolarize and the impulse to conduct to ventricles. This interval is 200 milliseconds at a normal person, the longer interval means AV block at the heart.

- QRS interval reflects the ventricular depolarization and atrial repolarization. Since the left ventricle has more muscle cells, the majority of QRS signal reflects left ventricular depolarization. The first negative deflection is called the Q wave, the first positive deflection is the R wave and the second negative deflection is called S wave. Since the conduction velocity in the bundle of His and the Purkinje fibers is large, the QRS complex looks sharp rather than rounded like P wave. The major causes of duration change in the QRS complex are cardiac arrhythmias, conduction abnormalities, ventricular hypertrophy, myocardial infarction and infra nodal conduction abnormalities.

- T wave period reflects the repolarization of ventricles. From the beginning of the QRS complex to the peak of the T wave is referred to as the absolute refractory period. The last half of the T wave is referred to as the relative refractory period. The normal QT interval, which is defined as the time between the beginning of the Q wave and the end of the T wave, is approximately 0.45 seconds. Prolongation of the QT interval may be a cause of sudden cardiac death.
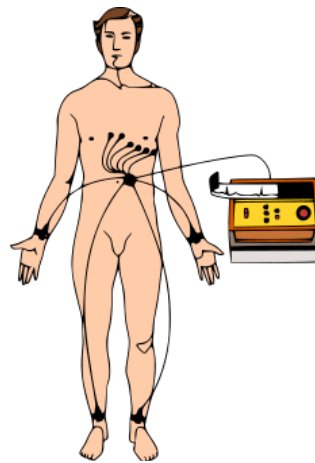
Figure 2.4: Position of 10 electrodes used for 12 Lead ECG [37]
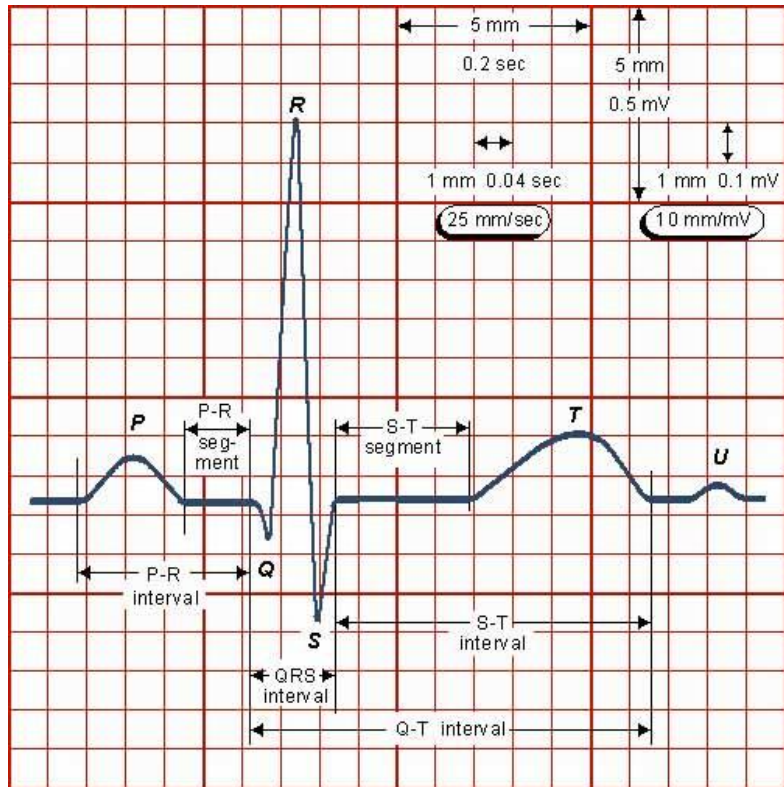
Figure 2.5: The normal Electrocardiogram [34]
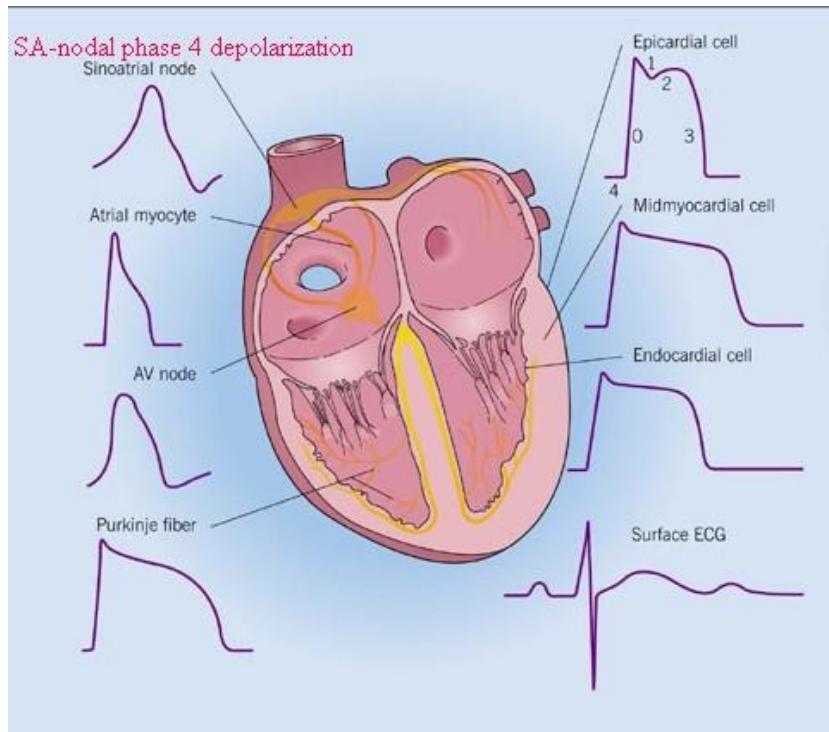
Figure 2.6: Different Forms of Cardiac Action Potential [38]

2.5. Forward Problem of Electrocardiography

The current generated by the electrical activity of the heart propagates through our body and reaches the body surface. Forward problem of ECG studies the relationship between cardiac sources and body surface potentials. The potentials generated on the body surface are affected by the electrical and geometrical properties of the torso. The forward ECG takes into account different properties of torso, while estimating body surface potentials generated from the heart potentials.

Different application areas of Forward ECG are [39]:

- Simulation of ECG with computer heart models: First a propagation algorithm is selected and activation times of all model points are calculated. Then equivalent source representations are used to calculate the ECG.
- Finding effects of torso inhomogeneities on ECG: The effects of materials with different conductivities are investigated, such as Brody effect, in which the effect of high conductivity blood in ventricular cavities is searched.
- Simulation of defibrillation currents: Different defibrillation simulations can be done to observe their effects.

There are three stages for finding a transfer matrix that relates torso potentials to heart surface potentials. These are defining an equivalent model for the heart's electrical activity, obtaining geometrical information and numerical solution of the forward problem.

2.5.1. Defining heart's electrical activity

Different simplified equivalent models are used to represent heart's electrical activity. These models can be grouped as:
- Current source models:
  - Fixed Dipole [40, 41],
  - Moving Dipole [40, 41],
  - Multipole [41, 42].
- Surface Source Models:
  - The Uniform Double Layer Model [41],
  - The Equivalent Double Layer Model [41, 43],
  - Epicardial and Endocardial Potential Models [44, 45, 46],
  - Transmembrane potential model [47],
  - Activation time based models [43].

2.5.1.1. The Dipole

Dipole is a current source which has two monopoles separated by a small distance. Dipole potential is infinity near the source, therefore dipole model can be used to define potentials away from the actual cardiac sources [40]. Dipole can only model the electrical activity restricted to a small part of the myocardium [41].

The dipole is characterized by six parameters: three for its location and three for its vector strength. For defining electrical activity of the heart, fixed and moving dipoles are used. Fixed dipoles have a fixed location; therefore they are only characterized by three vector strength parameters. The accuracy of modeling increases with number of parameters, but computational difficulty also increases.

The dipole can be used as a current generator during the whole QRS cycle. The body surface potentials can be modeled 80% accurately by a single dipole. The accuracy of this model can be increased by using multiple dipoles [41].

2.5.1.2. The Multipole

Heart may be modeled by using multipole current sources which have more than two magnetic poles. Different types of multipoles are: quadrupoles which have four poles and octupoles with eight

poles. The multipole representation can be expressed as a sum of multiple poles located at a common origin. The multipole model involves totally eleven parameters; three position parameters for the entire multipole system, three for dipole elements and five for quadrupole elements. This model was tested as a cardiac source model by Arthur [48] and the accuracy of the model is measured as 95% with the quadrupole elements. Because of the increasing parameter number, the computation gets more difficult which leads to decrease in the usage of multipole model [41, 42].

2.5.1.3. The Uniform Double Layer

The uniform double layer model represents heart's electrical activity by elementary current dipoles located on the myocardium. The propagation of surface current dipoles through myocardium represents depolarization wavefronts [41]. Since it is not easy to measure the potentials on the myocardium, the equivalent double layer method is mostly preferred [43].

2.5.1.4. The Equivalent Double Layer Model

The equivalent double layer model represents the electrical activity of the heart as double layer current dipole source sheets located on the heart layers endocaridum and epicardium, surrounding the myocardium. By using the solid angle theorem, the equivalent double layers located on the endocaridum and the epicardium are equal to uniform double layer located on the myocardium [41, 43].

2.5.1.5. Epicardial and Endocardial Potential Models

Epicardial and endocardial potential models are the widely used model for representing electrical activity of the heart. Since potentials are represented on the surface of the epicardium and endocardium layer, these equivalent sources are also called as surface potential maps.

Advantages of using surface potential model are [44, 45, 46]:

- Epicardial potentials can be measured by sock electrodes and endocardial potentials can be measured by catheter measurements, therefore solutions can be verified [49, 50].
- The solution of the problem is unique, because cardiac sources are located on the epicardial or endocardial layer.
- The effects of blood masses are avoided, because epicardium is the outer layer of the heart.
- The problem can be represented linearly.

The disadvantages of surface potential model are:

- The problem becomes higly ill-posed, because of smoothing and discretization effects in the thorax. To overcome ill-posedness, different regularization or statistical methods are used and different filters are applied.
- Epicardial potentials are given in terms of the transmembrane potentials of the whole heart instead of only neighbor nodes; therefore it has a more complicated structure [49].
- Surface potential models are less tolerated to geometrical errors [51, 52].

2.5.1.6. Transmembrane Potential Model

The voltage difference between interior and exterior of the cell membrane is called as transmembrane potential. In this method, the cardiac is modeled as the transmembrane potentials at the myocardium. Transmembrane potential model become popular because the problem can be formulated as a linear problem, but the obtained solution is not unique; therefore additional constraints are needed [47].

2.5.1.7. Activation Time Based Models

There is a potential difference between activated and inactive tissues during the propagation of activation in the heart. Some researchers modeled inverse problem by using this wavefront [43].

These models try to find activation time of tissues therefore deals with less parameter than surface models and this method is better posed than surface models. However, the solutions cannot be verified by measurements different than surface models. Other disadvantages are more complex calculations are needed because of non- linearity of the problem and the isotropy assumptions for myocardium causes some limitations for solution [39, 50].

2.5.2. Obtaining the Geometrical Information

Geometric information of cardiac and torso tissues should be determined first to solve the forward problem of electrocardiography. The mostly used methods for obtaining anatomical information of tissues are Computed Tomography (CT) or Magnetic Resonance Imaging (MRI). Drawbacks of these methods are, the equipments used are heavy and it is not easy to carry these equipments. Also these imaging systems are expensive [44]. Another method for obtaining the geometrical properties of body is electrical impedance tomography (EIT) which is cheaper and more mobile method when compared with CT and MRI. EIT measures the conductivities of tissues, but the major drawbacks of the EIT are the decrease in resolution when used for thicker tissues and it is not clinically used [53]. Cheng *et al.*used ultrasound to obtain the heart model and a hand held laser scanner to obtain the outer structures [54].

2.5.3. Numerical Solution of the Forward Problem

Numerical methods to solve the Forward problem of ECG can be separated into two classes: surface methods and volume methods. In surface methods, the torso is divided into regions with isotropic conductivity and only the boundaries of these regions are considered. Surface methods are also named the Boundary Element Method. In volume methods, the torso is separated into simple 3D volume elements or represented by three dimensional grids of discrete point elements. Volume methods are better in dealing with anisotropies in the torso. Volume methods include finite-difference, finite-element, and finite-volume methods.

2.5.3.1. Boundary Element Method (BEM)

Boundary element Method (BEM) uses surface integrals to calculate torso potentials generated by the electrical activity of the heart. Different from the volume methods, for BEM only the boundaries between regions with different conductivities should be modeled [39]. The advantage of BEM is the decrease in the number of unknown parameters and computational load. Especially, the decrease in the computational load made BEM a popular Forward solution method and commonly used in ECG, electroensephalography (EEG) and magnetoencephalography (MEG) [55]. On the other hand, BEM is not a suitable method for dealing with anisotropic regions [56].

Quality of meshes generated for modeling the region of interest is important to have accurate results, therefore scientists tried to use mesh elements with different size and type. Scientists also implemented adaptive methods such as h-adaptive BEM to increase accuracy, in these adaptive methods the meshes are regenerated to get better results during the calculation [55, 56].

2.5.3.2. Finite Difference Method (FDM)

In this method, torso geometry is represented as a three dimensional resistive network modeling body's geometric and conductivity properties. This system is composed of 3D grid of node points, resistor element values connecting these nodes are selected according to conductivity and geometry values of tissues between these nodes. Linear difference equations are established by using Ohm's and Kirchhoff's laws. These equations are solved iteratively and the potential distribution at each point is obtained [57]. The FDM was firstly used by Walker and Kilpatrick for defining electrocardiographic problems.

The FDM easily models complicated structures in the body, and an important property of FDM is that, accurate information about every element in the model is obtained, so the fields may be investigated in detail [57]. The disadvantage of FDM is its computational difficulty and large storage requirements, because of the large number of computational elements [39].

2.5.3.3. Finite Element Method (FEM)

In this method, torso is divided into volume elements; the most widely used volume elements are tetrahedra and hexahedra [39]. FEM is a suitable method for dealing with complex geometries and inhomogeneities in the torso. However the volume elements should be simple and easy to analyze. To handle the inhomogeneities and complex geometry of the torso, a large number of simple volume elements should be used, which increases the computational complexity of the problem [58].

A modified type of FEM is meshless FEM. The fundamental difference between meshless FEM and traditional FEM is the construction of shape functions. Meshless FEM uses only the node distribution, but conventional FEM uses both node distribution and connection between the nodes. Simulations show that meshless FEM shows a slightly better performance than conventional FEM in terms of accuracy, convergence and stability [59].

2.5.3.4. Finite Volume Method (FVM)

FVM is very similar to FDM; the difference between these two methods is that instead of using differential equations, surface integrals are discretized in FVM [60].

2.6. Inverse Problem of Electrocardiography

Inverse problem is obtaining information about an object or a system of interest, by using observed measurements. Solutions for these inverse problems are used in many areas of science and mathematics such as astronomy, physics, statistics, geophysics, computer vision and medical imaging.

Inverse problem of electrocardiography (ECG) is obtaining and understanding heart's electrical activity, by using measured torso potentials. To obtain an inverse ECG solution, patient's body anatomy and physical properties should also be known. Inverse solution of ECG is very important because, it gives information about possible cardiac abnormalities, effects of drugs may be monitored by using inverse ECG solutions.

The main difficulty in inverse problems is their ill-posed nature, which means there is not a unique solution for the inverse problem, because different solutions can be obtained for different source models. For this reason, obtaining a solution is not a very easy task. To overcome non-uniqueness of inverse ECG problem, simplified cardiac models are used. As explained before these cardiac source models are fixed dipole, multipole, moving dipole, the equivalent double layer model, the uniform double layer model, epicardial potential model, endocardial potential model, transmembrane potential model, activation time based models. According to the selected source model, different implicit constraints are applied for determination of model parameters from body surface potentials [86, 87]. Among these models, epicardial potential distribution is the most popular one and in this thesis, epicardial potential distribution is used to define heart's electrical activity. By using epicardial potential distribution, there is a unique model for solution of inverse ECG problem; however, ill-posedness still exists. There are always geometrical and measurement errors in the inverse ECG system. In case of small error in the system, the solution becomes unstable and oscillates in an unknown way. To overcome this ill-posedness, different regularization methods are used. Some of these methods use both spatial and temporal properties of the problem and others are not interested with temporal properties of the problem and only implement spatial constraints. In this thesis, we will focus on spatial methods that try to decrease the effect of singular values and arrange the condition number of the transfer matrix.

2.6.1. Spatio-Temporal Methods

Cardiac sources are correlated both in time and space, thus inverse ECG methods using both spatial and temporal properties would be more appropriate to solve the problem. These methods are usually referred to as the spatio-temporal methods. Their goal is to use more prior information by adding temporal constraints to the problem to decrease reconstruction error. In this section, spatio-temporal approaches will be investigated.

2.6.1.1. Multiple Constraints Approach

Brooks *et al*. [14] imposed multiple constraints instead of using single constraint for the solution of inverse ECG problem. In their study, they used an extra constraint within the standard Tikhonov regularization setting. They combined two spatial constraints and they also used one spatial and one temporal constraint which they call joint time/space (JTS) regularization. They also defined a new regularization parameter selection method called the L-surface for simultaneously selecting two optimum regularization parameters for both constraints. They validated their results by simulations using dipole sources and measured epicardial potentials. Their results show that JTS regularization give better solutions than using only spatial constraints and applying two spatial constraints decrease dependence to on a particular constraint and smaller regularization parameters are enough.

Gavgani *et al*. [61] used genetic algorithm to estimate multiple regularization parameter for Tikhonov regularization. They validated their results by using a realistic heart torso model and obtained that performance of Tikhonov regularization is improved by using genetic algorithm based multiple constraints.

2.6.1.2. Admissible Solution Approach

In literature, there are also methods trying to impose as many constraints as may be available. In this method, no regularization parameter is selected instead the nature and size of the constraints is defined. This method is suggested by Ghandi *et al*. [62] and they used multiple spatial constraints, temporal constraints and weighted constraints and tried to find a solution to meet collection of constraints set. For this purpose, an iterative algorithm is implemented which employs a constraint at every iteration. They stated the advantages of the admissible solution as:
- Regularization parameters are replaced with direct bounds which are easier to implement.
- Large number of constraints can be implemented without changing solution method.
- Since, method employs single constraints iteratively; effectiveness of each constraint on the solution can be examined.

2.6.1.3. State Space Models

State space models which is also known as the Kalman filter and the Kalman smoother use spatial and temporal properties of inverse ECG problem [15, 16, 17, 18, 19]. The spatio-temporal relationship between two consecutive time instants is defined by a matrix called the state transition matrix (STM). The main complexity in the Kalman filter approach is the determination of STM. In their study, Berrier *et al*. [15] used an identity matrix multiplied with a scalar as a STM relating only the next value of epicardial potential by the present value. Their study showed that Kalman filter gives better results than the spatial Tikhonov regularization and the temporal Twomey regularization methods. Goussard *et al*. used epicardial potentials to calculate the STM [16, 17]. They concluded that proper definition of STM is patient dependent and very important for Kalman filter approach, because Kalman filter can give better or worse results than Tikhonov or Twomey regularization methods depending on the STM choice.

2.6.1.4. Bayesian Maximum A Posteriori (MAP) Estimation

The Bayesian MAP estimation method needs prior information about the epicardial potentials to define the *a* priori probability density function (PDF) and maximizes the a posteriori PDF. Bayesian MAP approach can be solved separately for all time instants which makes it a spatial method [20] or, it can be used as a spatio-temporal method by taking advantage of the temporal correlations in addition to the spatial correlations of the epicardial potentials [21].

2.6.2. Spatial Methods

Spatial methods use only spatial properties of the ill-posed problem and does not interest with temporal properties. Some of the spatial methods in the literature are Tikhonov regularization [6, 7, 8], TSVD [7, 9], LSQR [10, 11], TTLS [12, 13], Lanczos TTLS [13]. Some methods like Bayesian MAP can be used as both spatial and spatio-temporal method. Here, we will focus on the spatial methods that we used in this thesis, which eliminate singular values causing error in the solution of the inverse ECG problem or arrange condition number of the transfer matrix by modifying it to a

more suitable value. These methods do not need special a priori information such as the priori PDF, or the STM. They use well-defined spatial constraints to solve the problem.

2.6.2.1. Tikhonov Method

Tikhonov regularization is the most commonly used method for the solution of inverse ECG problem. Tikhonov regularization aims to minimize the cost function by imposing some constraints on the magnitude or derivatives of epicardial potentials. It is a method based on linear least squares, which deals with only measurement errors on the torso potentials and largely effected by geometric errors.

Regularization parameter selection methods for Tikhonov method are inspected in different papers. Johnston *et al*. [6] compared performances of CRESO, L curve and their proposed method zero crossing method. Performances of these parameter selection algorithms were tested by concentric sphere model and realistic torso model. According to the results, all of the methods gave similar results, but estimation of the regularization parameter value using the zero crossing method is much simpler. In a study by Shou *et al*. [7], a concentric sphere model and a realistic heart-lung-torso model were used and torso meshes were obtained by h-adaptive BEM Method. By using these simulation environments, performances of parameter selection methods; GCV, L-curve and the discrepancy principle (DP) methods were compared. Simulations done for measurement error case and all methods gave similar results for small noises. With increasing noise, DP yielded better results, but it needed prior information about noise, therefore L-curve and GCV were more useful.

Tikhonov method was used as a performance measurement criterion by Robert D. Throne *et al*. [8]. In this study, performance of Generalized Eigensystem (GES) technique was compared with Tikhonov regularization and TSVD methods. According to simulations made using a realistic heart torso model, GES gave better results than another in terms of the residual error.
There is also a modified version of Tikhonov regularization which is called the Twomey regularization. Here, a priori information about the desired epicardial potentials is needed [63]. Therefore, Twomey method is not used as much as the Tikhonov method.

2.6.2.2. Truncated Singular Value Decomposition

TSVD is another most commonly used inverse ECG solution method. TSVD is based on truncation method, which means ignoring small singular values. Because of ignoring small singular values, high frequency components are ignored; therefore, the solution is smooth. TSVD is also a linear least squares based method and is effected by geometrical errors like other least squares based methods. Tikhonov and TSVD are usually used as reference methods for assessing the performances of different regularization methods.

Performance of TSVD is compared with Tikhonov regularization and Truncated Total Least Squares by Shou *et al*. [9]. In their study, same real heart-torso model with previous study is used [7]; only the ventricular region of the heart is included and the electrical activity of the heart was represented by a radial current dipole source. The transfer matrix was obtained by BEM. GCV method was used for regularization parameter selection. For only the measurement error case, all methods have similar results, but with increasing noise Tikhonov regularization and TTLS gave slightly better results than the TSVD. In a second simulation, geometry error was also added; in this case TTLS gave better results, because it can also handle geometrical errors.

2.6.2.3. Least-Squares QR Method

LSQR is an iterative method based on Lanczos bidiagonalization and QR factorization, which is practical when transfer matrix A is large and sparse [10]. Performance of LSQR method is compared with different regularization methods. Jiang *et al*. [11] compared the performance of LSQR method with well-known regularization methods Tikhonov regularization and the TSVD method. Genetic algorithm was also used to optimize the LSQR based inverse ECG solutions. A realistic heart-torso model was used for simulation protocol. Epicardial potentials were modeled by a single dipole and different levels of Gaussian measurement errors were added to torso potentials. During computer simulation, iteration number of the LSQR method, the regularization parameter value of the Tikhonov regularization method and the truncation level of the TSVD method were selected by the

L-curve method. For different measurement and geometrical error values LSQR gave better results than the TSVD and Tikhonov regularization. By increasing the noise level, advantage of LSQR became clearer. It was also observed that combining LSQR with genetic algorithm gave better results.

2.6.2.4. Truncated Total Least Squares

TTLS method is similar to the TSVD method; the main difference is that in TTLS, singular values of (**A**,**Y**) matrix are found and small singular values are neglected in the reconstruction [13]. Since, singular values of (**A**,**Y**) are computed, TTLS method is effective for both measurement and geometrical errors.

TTLS method was compared with the traditional regularization methods Tikhonov regularization and the TSVD method by Shou *et al*. [12]. To measure the performances of these algorithms, a realistic heart- lung-torso model was used and forward problem of ECG was solved by using h-adaptive BEM method. The epicardial potentials were generated from a current dipole inside the heart and normalized to ±10 mV. GCV method was used for parameter selection for all regularization methods. Two different simulations were conducted for 30 dB and 50 dB measurement errors with no geometric error and with geometric error. In general, geometric error is simulated as moving heart in a direction and solving the inverse ECG problem for this situation, but in this article geometric error is characterized by adding a random error matrix to the transfer matrix.

In the first simulation without the geometric error case, it was observed that with increasing error second order TSVD, TTLS and Tikhonov give worse results than zero and first order. It was also observed that all methods perform similarly, but TTLS and Tikhonov give slightly better results than TSVD. In the second simulation geometric error was also added to the system. It was observed that, TTLS gives better results than other two for different geometric error levels, especially in the no measurement error case. It was also stated that TTLS is a fast algorithm and applicable for real time applications.

2.6.2.5. Lanczos TTLS

Lanczos TTLS algorithm is a modified version of TTLS method. The complexity of SVD algorithm is $O(mn^2)$, therefore when the dimension of transfer matrix is large, it is computationally difficult to calculate the SVD of the transfer matrix. There are partial singular value computation algorithms [88] for calculating SVD of (**A**,**Y**) for a sufficiently large truncation parameter. However, sparsity and structure of the transfer matrix is lost by these algorithms. For these reasons, iterative methods based on Lanczos bidiagonalization, which do not change the transfer matrix, are considered. Thus, in this thesis we also included a Lanczos bidiagonalization based TTLS approach [13].

This method has not been used to solve the inverse ECG problem, however applications in other inverse problems have been reported. For example, in [13], it was used to solve discretization of Phillips's test problem [64]. Fierro *et al*. compared performance of Lanczos TTLS with Tikhonov regularization and singular value decomposition based methods TTLS and TSVD. For simulations, a transfer matrix was used with size 64×32, based on Phillips problem [64]. Performances of three algorithms were compared for high and low level noises. For the high noise case, TTLS and Lanczos TTLS gave better results than others. The histograms obtained based on 1000 tests were very similar for TTLS and Lanczos TTLS. For the low level noise case, all methods gave similar results. Average number of flops for TTLS, Lanczos TTLS and full bidiagonalization were also compared. According to test results, it was observed that Lanczos TTLS is ten times faster than the TTLS for some cases. And for larger transfer matrices, this ratio increases according to sparsity and structure of the transfer matrix. Finally, they concluded that TTLS method has a filtering effect in discrete ill-posed problems and gives better results than TSVD for most cases. Lanczos bidiagonalization based iterative Lanczos TTLS method has more accurate results than TTLS for large sized sparse and structured matrices.

2.6.3. Other Methods

2.6.3.1. Genetic Algorithm (GA) in the Solution of Inverse ECG Problem

Studies in the literature show that GA cannot be used as a regularization method individually for solving the inverse ECG problem; however, it gives better results when combined with other regularization methods [65]. Jiang *et al.* [65] used GA to optimize results obtained by Tikhonov regularization method. They used a concentric sphere heart torso model in their simulations and they obtained better results with lower residual error and higher correlation coefficient. In another study by Jiang *et al.* [66], they both used TSVD and Tikhonov as additional constraints for the GA. A realistic heart torso model was used for their simulation and they concluded that genetic algorithm is helpful to improve the performances of TSVD and Tikhonov, especially at higher noise levels. Gavgani *et al.* [61] showed that GA can be used for determination of the regularization parameters in the multiple constraints approach. In other studies [67, 68] LSQR was also combined with the GA to improve the results.

2.6.3.2. Model based Approaches

Patient specific models are also used for inverse ECG problem. Farina *et al*. [22] used MRI images to obtain patient specific thorax model. Then a cellular automaton model was used to obtain the transmembrane potentials within the cardiac tissue by using an anatomical model of the patient's heart generated from the MRI images. Then, the forward ECG problem was solved. The simulated transmembrane potentials were used as a priori information for Twomey and stochastic regularization methods in the solution of the inverse ECG problem. According to their results, stochastic regularization gave the best results, and Twomey was better than Tikhonov regularization.

In another study, He *et al*. [23] proposed a new method to obtain cardiac transmembrane potentials by using an anisotropic heart model. They used CT and MRI images to obtain a realistic heart torso model. Then they simulated body surface potentials by using this realistic heart torso model. Simulated body surface potentials were compared with the measured ones and by assessing the error between these measured and simulated potentials, the source configuration was altered to obtain better solutions. By this way, they have developed a spatio-temporal approach to obtain cardiac transmembrane potentials on 3-D the myocardium.

2.6.3.3. Other Approaches

There are also different approaches for solving the inverse ECG problem. Three dimensional cardiac bioelectrical sources modeled by current dipoles can be estimated by using Laplacian weighted minimum norm method (LWMN) [69]. In that study the inverse solution was improved by using a recursive weighting strategy due to smoothing effects of the Laplacian operator. They also conducted computer simulations using realistic heart torso models to measure performance of the method. Results showed that this method can be used for localizing cardiac electrical activity in the 3-D myocardium.

Generalized eigensystem (GES) approach [70] was also used to solve the inverse ECG problem. This method uses finite element method to generate a truncated eigenvector expansion for stabilizing inversion. Throne *et al.* [71] also used the GES technique for the solution of inverse ECG and compared it with Tikhonov regularization and TSVD by using a realistic heart torso model. Their study showed that GES gives better solutions. The study carried out by Nash *et al*. [72] is important because they measured potentials from both the heart and the body surfaces of a pig simultaneously during an acute period of regional ventricular ischemia. They plan to use their database of recordings to validate the inverse ECG approach.

CHAPTER 3

METHODS

In this chapter, theory of inverse ECG problem and the methods used to find a solution will be explained. As explained before, inverse ECG is the determination of unknown electrical activity of the heart from measured body surface potentials. The inverse problem of ECG is ill posed, hence the forward transfer matrix is ill conditioned. Therefore, regularization methods are used to find a solution for inverse ECG problem. At this section, the details of Tikhonov, TSVD, LSQR, TTLS and Lanczos TTLS will be given.

3.1. Problem Definition

Epicardial potentials and body surface potentials are related by the following linear equation in the forward problem of ECG:

$$\mathbf{Y} = \mathbf{AX} + \mathbf{N}, \tag{3.1}$$

where $\mathbf{X} \in \mathrm{R}^{nxt}$ is the matrix of unknown epicardial potentials, $\mathbf{Y} \in \mathrm{R}^{mxt}$ is the matrix of body surface potential measurements, $\mathbf{N} \in \mathrm{R}^{mxt}$ is the matrix representing Gaussian measurement errors and $\mathbf{A} \in \mathrm{R}^{mxn}$ is the forward transfer matrix. Here, we assume that there are m measurement electrodes on the body surface, n nodes on the epicardial surface, and the signals are measured at t different time instances.

For a time instant, visual representations of epicardial and torso potentials are given in Figure 3.1. In our problem epicardial potentials are measured from 490 nodes on the heart and body surface potentials are measured from 771 nodes.

Equation 3.1 can be also stated in vector notation for every time instance as:

$$\mathbf{y}(k) = \mathbf{Ax}(k) + \mathbf{n}(k) \qquad k = 1,2,\dots,t , \tag{3.2}$$

where k represents each time instance and the solution is found for every time instances, but the notation that we are going to use in this section is in the matrix form as in Equation 3.1.
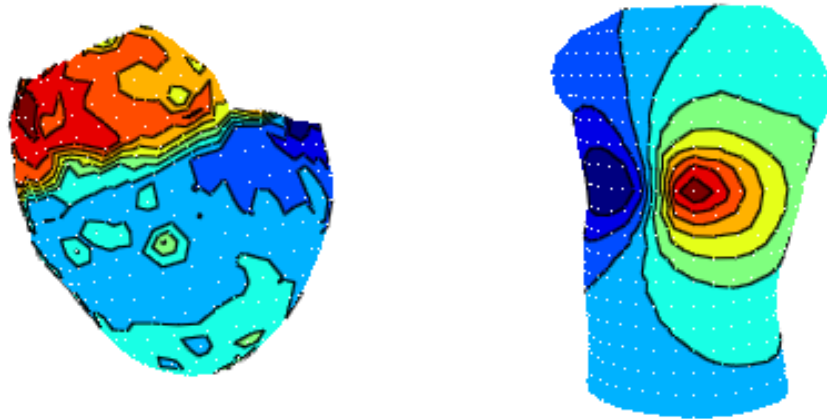
Figure 3.1: Visual representation of epicardial and torso potentials for a time instance

3.2. Properties of the transfer matrix A

The transfer matrix **A** is obtained as the solution of the forward problem of ECG. Boundary Element Method (BEM) is used for the solution of the forward problem [56].

In our case, the transfer **A** matrix is not square, for this reason direct inverse cannot be obtained. For full rank non square matrix $\mathbf{A} \in \mathrm{R}^{mxn}$, where $m \geq n$, the left inverse of **A** matrix is calculated as:

$$\mathbf{A}^{-1} = (\mathbf{A}^T \mathbf{A})^{-1} \mathbf{A}^T , \tag{3.3}$$

but transfer matrix **A** is not full rank at our problem, therefore Equation 3.3 is not applicable. Pseudo inverse of transfer matrix **A** can be obtained, but it may not give good results. This is related with condition number or singular values of transfer matrix. The condition number is another parameter for defining a matrix as an ill-conditioned or well-conditioned matrix. The condition number of the matrix **A** is defined as the multiplication of the norm of **A** and the norm of inverse of **A**:

$$C = \|\mathbf{A}\| \|\mathbf{A}^{-1}\| . \tag{3.4}$$

The norm of **A** is defined as:

$$\|\mathbf{A}\| = \max_{1 \leq j \leq n} \sum_{i=1}^{n} |a_{ij}| . \tag{3.5}$$

Alternatively, it can be defined as ratio of largest singular value to the smallest singular value of **A**. The condition number of a matrix is greater than or equal to 1. When the condition number of matrix is close to 1, it means the matrix is well-conditioned and the inverse of matrix can be calculated accurately. Matrices with large condition number are called ill-posed matrices and their inverse cannot be calculated correctly. When the condition number is infinity, it means that matrix is not invertible.

Figure 3.2 shows the singular values of transfer matrix **A**, when the figure is inspected it is seen that the largest singular value of **A** matrix is 1.5 and the smallest one is near zero, therefore the condition number of our forward matrix **A** is equal to 2.88×10^{13}, which means that **A** is an ill-conditioned matrix.
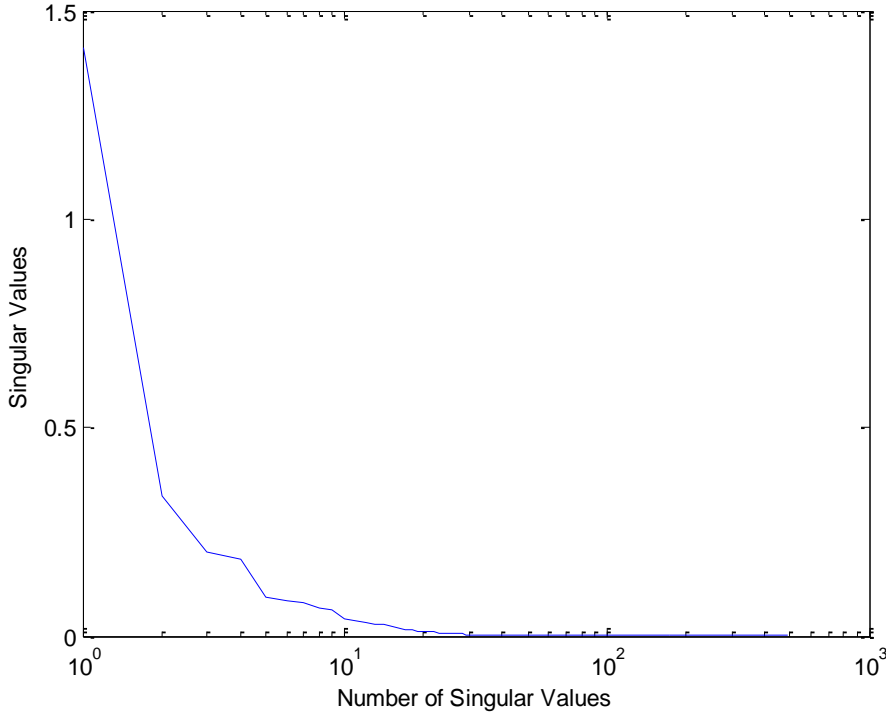
Figure 3.2: Singular values of **A** matrix

3.3. Inverse Solution Methods

Due to this ill-posedness, any small noise causes large perturbation in the inverse solution making it unreliable and often meaningless. Since there is noise on the measurements, the transfer matrix is not error free. Different regularization methods have been used in literature to solve this problem. In the rest of this chapter, we present some of the regularization methods that we used in our thesis study to find estimated epicardial potentials (X_{est}).

3.3.1. Truncated Singular Value Decomposition (TSVD)

The singular value decomposition (SVD) is a method for solving ill-posed linear problems. When singular value decomposition is used to define transfer matrix $A \in R^{mxn}$ where $\geq n$:

$$A = USV^T = \sum_{i=1}^{n} u_i s_i v_i^T \quad , \tag{3.6}$$

where
$U = \{u_1, u_2, \dots, u_m\} \in R^{mxm}$ and $U^TU = I^{mxm}$,
$V = \{v_1, v_2, \dots, v_n\} \in R^{nxn}$ and $V^TV = I^{nxn}$.

The columns of U and V are left and right singular matrix respectively. S is a diagonal matrix containing singular values ($s_1, s_2, \dots, s_m$) of A, and the off-diagonal elements are 0.

$$S = \begin{bmatrix} s_1 & 0 & 0 & 0 & 0 \\ 0 & s_2 & 0 & 0 & 0 \\ 0 & 0 & \ddots & 0 & 0 \\ 0 & 0 & 0 & \ddots & 0 \\ 0 & 0 & 0 & 0 & s_m \\ 0 & 0 & 0 & 0 & 0 \end{bmatrix}$$

The main idea behind SVD method is calculating the eigenvectors and eigenvalues of A^TA and AA^T. The columns of U consists eigenvectors of A^TA and columns of V are the eigenvectors of AA^T respectively. The square roots of A^TA or AA^T are the singular values, where the diagonal matrix S consists of singular values $s_1 \geq s_2 \geq \dots \geq s_n \geq 0$.

TSVD is a commonly used method for solving the inverse ECG problem [39]. It is based on finding the singular value decomposition of the coefficient A matrix, and finding a regularized solution by ignoring small singular values.

The inverse of the transfer matrix A can be written as:

$$A^{-1} = \sum_{i}^{n} u_i^T \frac{1}{s_i} v_i \ , \tag{3.7}$$

by using Singular Value Decomposition. Then, the solution of Equation (3.1) can be written as by multiplying both sides of equation with A^{-1}:

$$X = \sum_{i=1}^{n} u_i^T \frac{AX + N}{s_i} v_i \ = \sum_{i=1}^{n} u_i^T \frac{AX}{s_i} v_i + \sum_{i=1}^{n} u_i^T \frac{N}{s_i} v_i \ . \tag{3.8}$$

From (3.8), it can be seen that the effect of small singular values are large on the solution. For this purpose, an optimum truncation parameter k for every time instance is determined and the k-largest singular values are used in the solution:

$$A_k = US_kV^T = \sum_{i}^{k} u_i s_i v_i^T \ , \qquad (k \leq n) \quad . \tag{3.9}$$

When the truncation level k is chosen properly, the condition number of A_k matrix is small. Estimated solution X_{est} can be written as by truncating small singular values:

$$\mathbf{X}_{est} = \sum_{i=1}^{k} \mathbf{u}_i^T \frac{\mathbf{AX}}{s_i} \mathbf{v}_i + \sum_{i=1}^{k} \mathbf{u}_i^T \frac{\mathbf{N}}{s_i} \mathbf{v}_i \quad . \tag{3.10}$$

Truncating k singular values is equivalent to applying a filter f_i to the solution found at (3.12), where f_i is:

$$\begin{aligned} f_i &= 1 & i < k \ , \\ f_i &= 0 & n > i > k \ . \end{aligned}$$

By using filter factors, $\mathbf{X}_{est}$ can be written as:

$$\mathbf{X}_{est} = \sum_{i=1}^{n} \mathbf{u}_i^T f_i \frac{\mathbf{AX}}{s_i} \mathbf{v}_i + \sum_{i=1}^{n} \mathbf{u}_i^T f_i \frac{\mathbf{N}}{s_i} \mathbf{v}_i \quad . \tag{3.11}$$

3.3.2 Tikhonov Regularization

Tikhonov regularization is one of the most popular regularization methods to deal with the ill posed nature of the inverse ECG problem [73]. In this method, the solution is chosen to minimize the cost function consisting of the residual error norm and a constraint norm:

$$\hat{\mathbf{x}}_\lambda = \mathrm{argmin}_{\mathbf{x}}\{\|\mathbf{Ax} - \mathbf{y}\|^2 + \lambda^2 \|\mathbf{Rx}\|^2\} \quad , \tag{3.12}$$

where λ is the regularization parameter controlling the relative weights of the residual and constraint norms, $\hat{\mathbf{x}}_\lambda$ is the solution for a specific regularization parameter λ, and $\mathbf{R}$ is the regularization matrix defining the constraint to be used for regularization. For "zero order" Tikhonov regularization, $\mathbf{R}$ matrix is chosen as the identity matrix ($\mathbf{R} = \mathbf{I}$), for "first order" Tikhonov regularization, $\mathbf{R}$ is chosen as the surface gradient operator ($\mathbf{R} = \mathbf{G}$) and for "second order" Tikhonov regularization, it is the surface Laplacian operator ($\mathbf{R} = \mathbf{L}$). In this study, we use the zero-order Tikhonov regularization method, because it is more appropriate for solution of inverse ECG [74].

For Tikhonov problem (3.5), there are two alternative representations:

$$(\mathbf{A}^T\mathbf{A} + \lambda^2\mathbf{R}^T\mathbf{R})\mathbf{x} = \mathbf{A}^T\mathbf{y} \quad , \tag{3.13}$$

$$\min \ \left\| \begin{pmatrix} \mathbf{A} \\ \lambda\mathbf{R} \end{pmatrix} \mathbf{x} - \begin{pmatrix} \mathbf{y} \\ 0 \end{pmatrix} \right\|_2 \quad . \tag{3.14}$$

From Equations (3.13) and (3.14), we see that there is a unique solution $\mathbf{X}_{est}$, if the null space of $\mathbf{A}$ intersects with the null space of $\mathbf{R}$ (i.e., $N(\mathbf{A}) \cap N(\mathbf{R}) = \{0\}$) in other words, the coefficient matrix has full rank [24].

$$\mathbf{X}_{est} = \mathbf{A}_\lambda \mathbf{y} \quad , \tag{3.15}$$

where

$$\mathbf{A}_\lambda = (\mathbf{A}^T\mathbf{A} + \lambda^2\mathbf{R}^T\mathbf{R})^{-1}\mathbf{A}^T \quad , \tag{3.16}$$

is the Tikhonov regularized inverse.

Tikhonov method is equivalent to applying filter factors to singular value decomposition representation of $\mathbf{X}$:

$$\mathbf{X}_{est} = \sum_{i=1}^{n} \frac{s_i^2}{s_i^2 + \lambda^2} \frac{\mathbf{u}_i^T \mathbf{y}}{s^i} \mathbf{v}_i \quad . \tag{3.17}$$

The first term $f_i(\lambda) = \frac{s_i^2}{s_i^2 + \lambda^2}$ in Equation (3.17) is called the filter factor and it ignores the amplification of small singular values. By using this filter factor, Equation (3.11) is written as:

$$\mathbf{X}_{est} = \sum_{i=1}^{n} f_i \frac{\mathbf{u}_i^T \mathbf{y}}{s_i} \mathbf{v}_i \quad . \tag{3.18}$$

From Equation (3.18), it is obvious that larger singular values have larger effect and the determination of regularization parameter λ is important. There are different ways to find an optimal regularization parameter; the L-Curve approach [30], Generalized Cross Validation (GCV) method [25, 26], Composite Residual and Smoothing Operator (CRESO) [27] and maximum correlation coefficient method [75]. These methods will be explained later.

3.3.3. Least Squares QR (LSQR) Method

Least Squares QR (LSQR) [11] is an iterative method for solving the linear systems as in Equation (3.1). LSQR method iteratively produces $\mathbf{X}^{(k)}$ matrices for iteration number $k = 1,2,3..$, after k iterations $\mathbf{X}^{(k)}$ approaches to optimal solution. If a stopping condition for k is not implemented a noise corrupted solution with high relative error is obtained. Determination of correct regularization parameter k is an important stage at LSQR method solution.

LSQR method starts with finding the lower bidiagonal form of $\mathbf{A}$ matrix by using Lanczos Bidiagonalization (LBD) procedure [76], which is an useful tool for finding decompositions of large sparse matrices. LBD computes vectors $\mathbf{u}_j \in \mathbf{I}R^m$, $\mathbf{v}_j \in \mathbf{I}R^n$ which are different than vectors produced by SVD method and scalars α_j, β_j, which meets $\mathbf{B}_k = \mathbf{U}^T \mathbf{A} \mathbf{V}$.

Here, the columns of U_{k+1} and V_k matrices are orthanormal vectors, if exact arithmetic is used:

$$\mathbf{U}_{k+1} = (\mathbf{u}_1, \mathbf{u}_2, \dots, \mathbf{u}_{k+1},) \in R^{m*(k+1)} \quad , \qquad \mathbf{U}_{k+1}^T \mathbf{U}_{k+1} = \mathbf{I}_{k+1} \quad ,$$

$$\mathbf{V}_k = (\mathbf{v}_1, \mathbf{v}_2, \dots, \mathbf{v}_{k+1},) \in R^{n*k} \quad , \qquad \mathbf{V}_k^T \mathbf{U}_k = \mathbf{I}_k \quad .$$

$\mathbf{B}_k \in R^{(k+1)*k}$ is a lower bidiagonal matrix:

$$\mathbf{B}_{k=} \begin{bmatrix} \alpha_1 & 0 & 0 & 0 & 0 \\ \beta_2 & \alpha_2 & 0 & 0 & 0 \\ 0 & \beta_3 & \ddots & 0 & 0 \\ 0 & 0 & \ddots & \ddots & 0 \\ 0 & 0 & 0 & \ddots & \alpha_k \\ 0 & 0 & 0 & 0 & \beta_{k+1} \end{bmatrix}$$

The algorithm for Lanczos Bidiagonalization is given below [76]:

- Choose a starting vector $\mathbf{y} \in \mathbf{I}R^m$ and let
  $\beta_1 = \|\mathbf{y}\|_2$, $\mathbf{u}_1 = \frac{\mathbf{y}}{\beta_1}$, $\mathbf{v}_0 = 0$ and α_1
  for $i = 1, 2, ..., k$ do
  $\mathbf{r}_i = \mathbf{A}^T \mathbf{u}_i - \beta_i \mathbf{v}_{i-1}$
  $\alpha_i = \|\mathbf{r}_i\|_2$
  $\mathbf{v}_i = \frac{\mathbf{r}_i}{\alpha_i}$
  $\mathbf{p}_i = \mathbf{A}\mathbf{v}_i - \alpha_i \mathbf{u}_i$
  $\beta_{i+1} = \|\mathbf{p}_i\|_2$
  $\mathbf{u}_{i+1} = \frac{\mathbf{p}_i}{\beta_{i+1}}$
  end

For different k values, the u_{k+1}, v_k vectors, torso potential Y and bidiagonal B_k matrix are related by

$$\mathbf{Y} = \beta_1 \mathbf{u}_1 = \beta_1 \mathbf{U}_{k+1} \mathbf{e}_1 \quad , \tag{3.19}$$

$$\mathbf{A}\mathbf{V}_k = \mathbf{U}_{k+1} \mathbf{B}_k \quad , \tag{3.20}$$

$$\mathbf{A}^T \mathbf{U}_{k+1} = \mathbf{V}_k \mathbf{B}_k^T + \alpha_{k+1} \mathbf{v}_{k+1} \mathbf{e}_{k+1}^T \quad , \tag{3.21}$$

where $\mathbf{e}_k$ is the kth unit vector.

The relations obtained by Lanczos bidiagonalization can be used to solve the least-squares problem:

$$\text{Min} \, \|\mathbf{Y} - \mathbf{A}\mathbf{X}\|_2 \quad . \tag{3.22}$$

Let the epicardial potential at k^{th} iteration:

$$\mathbf{X}^{(k)} = \mathbf{V}_k \mathbf{y}^{(k)} \quad . \tag{3.23}$$

The residual is defined as by using Equations (3.19) and (3.23):

$$\mathbf{r}^{(k)} = \mathbf{Y} - \mathbf{A}\mathbf{X}^{(k)} = \beta_1 \mathbf{u}_1 - \mathbf{A}\mathbf{V}_k \mathbf{y}^{(k)} \quad . \tag{3.24}$$

From Equation (3.20), the residual takes the following form:

$$\mathbf{r}^{(k)} = \mathbf{U}_{k+1}(\beta_1 \mathbf{e}_1 - \mathbf{B}_k \mathbf{y}^{(k)}) \quad . \tag{3.25}$$

To minimize residual $\mathbf{r}^{(k)}$, $\mathbf{t}_{k+1} = \beta_1 \mathbf{e}_1 - \mathbf{B}_k \mathbf{y}^{(k)}$ should be decreased because $\mathbf{U}_{k+1}$ is bounded and orthanormal. Therefore, the least-squares problem changes to

$$\text{Min} \, \|\beta_1 \mathbf{e}_1 - \mathbf{B}_k \mathbf{y}^{(k)}\|_2 \quad , \tag{3.26}$$

which forms a basis for LSQR.

QR decomposition is a popular method to solve the linear least squares problem [77]. When QR factorization of $\mathbf{B}_k$ is calculated, an orthogonal matrix $\mathbf{Q}_k$ and an upper triangular matrix $\mathbf{R}_k$ are produced.

Multiplication of $\mathbf{Q}_k^T$ with $[\mathbf{B}_k \mid \beta_1 \mathbf{e}_1]$ produces a $(k+1) \times (k+1)$ matrix, which consists of three parts: an upper triangular $k \times k$ matrix $\mathbf{R}_k$, a $k \times 1$ vector $\mathbf{f}_k$ and a scalar $\overline{\emptyset}_{k+1}$.

$$\mathbf{Q}_k^T [\mathbf{B}_k \quad \beta_1 \mathbf{e}_1] = \begin{bmatrix} \mathbf{R}_k & \mathbf{f}_k \\ 0 & \emptyset_{k+1} \end{bmatrix} = \begin{bmatrix} p_1 & \theta_2 & 0 & 0 & 0 & \emptyset_1 \\ 0 & p_2 & \theta_3 & 0 & 0 & \emptyset_2 \\ 0 & 0 & \ddots & \ddots & 0 & \vdots \\ 0 & 0 & 0 & \ddots & \theta_k & \vdots \\ 0 & 0 & 0 & 0 & p_k & \emptyset_k \\ 0 & 0 & 0 & 0 & 0 & \overline{\emptyset}_{k+1} \end{bmatrix} .$$

The vectors $\mathbf{y}^{(k)}$ and $\mathbf{t}_{k+1}$ could then be calculated from:

$$\mathbf{f}_k = \mathbf{R}_k \mathbf{B}_k \mathbf{y}^{(k)} \quad , \tag{3.27}$$

$$\mathbf{t}_{k+1} = \mathbf{Q}_k \begin{pmatrix} 0 \\ \overline{\emptyset}_{k+1} \end{pmatrix} \quad . \tag{3.28}$$

By combining Equations (3.23) and (3.27), an estimated solution for k^{th} iteration found by LSQR method:

$$\mathbf{X}^{(k)} = \mathbf{V}_k \mathbf{y}^{(k)} = \mathbf{V}_k \mathbf{R}_k^{-1} \mathbf{f}_k \quad . \tag{3.29}$$

LSQR is an iterative method, so stopping point must be chosen correctly to find an approximate solution $\mathbf{X}^{(k)}$ to true epicardial potential $\mathbf{X}$. Correct stopping point k can be determined by different regularization parameter selection methods.

3.3.4. Truncated Total Least squares (TTLS)

The total least squares (TLS) method is based on least squares approximation, used for the case when coefficient matrix $\mathbf{A}$ and the right hand side matrix $\mathbf{Y}$ have error terms. Truncated total least squares method is a modified TLS method, which filters the effect of small singular values [13, 78, 79]. By this property TTLS seems similar to TSVD, but the main difference is while TTLS discards the redundant information at both $\mathbf{A}$ and $\mathbf{Y}$ matrices, TSVD only deals with coefficient matrix $\mathbf{A}$. An important stage in the solution procedure is the selection of truncation level. The algorithm of TTLS method is given below [13]:

• The singular value decomposititon of augmented matrix $(\mathbf{A}, \mathbf{Y})$ is calculated as explained before:

$$(\mathbf{A}, \mathbf{Y}) = \mathbf{USV}^T = \sum_{i=1}^{n+1} \mathbf{u}_i s_i \mathbf{v}_i^T \quad , \tag{3.30}$$

where $\quad s_1 \geq s_1 \geq \cdots \geq s_{n+1} \quad .$

• A truncation parameter $k \leq \min(n, \text{rank}(\mathbf{A},\mathbf{Y}))$ is selected such as :

$$s_k \geq s_{k+1} \quad and \quad \mathbf{V}_{22} = (v_{n+1,k+1,\dots,}v_{n+1,n+1}) \neq 0$$

Selection of truncation parameter is accomplished by using different regularization parameter selection methods.

• The V matrix is partitioned as:

$$\bar{V} = \begin{pmatrix} \overset{k}{\longleftrightarrow} & \overset{q}{\longleftrightarrow} \\ \bar{V}_{11} & \bar{V}_{12} \\ \bar{V}_{21} & \bar{V}_{22} \end{pmatrix} \begin{matrix} \updownarrow & n \\ \updownarrow & 1 \end{matrix} \tag{3.31}$$

where $q = n - k + 1$

• The minimum norm TTLS solution $\mathbf{x}_k$ is computed as:

$$\mathbf{x}_k = -\mathbf{V}_{12} \, \mathbf{V}_{22}^+ = -\frac{\mathbf{V}_{12} \, \mathbf{v}_{22}^T}{\|\mathbf{V}_{22}\|_2} \quad . \tag{3.32}$$

The pseudo inverse of $\mathbf{V}_{22}$ $(\mathbf{V}_{22}^+)$ exists because the norm of $\mathbf{V}_{22}$ is not zero $(\|\mathbf{V}_{22}\| \neq 0)$. The norm of $\mathbf{x}_k$ is calculated as:

$$\|\mathbf{x}_k\| = \sqrt{\|\mathbf{V}_{22}\|^{-2} - 1} \quad . \tag{3.33}$$

The TLS residual is defined as:

$$\left\|(\mathbf{A}, \mathbf{Y}) - (\widetilde{\mathbf{A}}, \widetilde{\mathbf{Y}})\right\|_F = \sqrt{s_{n+1}^2 + \dots + s_{k+1}^2} \quad . \tag{3.34}$$

$\| \quad \|_F$ is the frobenius norm, which is the square root of the sum of the absolute squares of matrix elements, $\widetilde{\mathbf{A}}$ and $\widetilde{\mathbf{Y}}$ are the error versions of coefficient and body surface potential distribution matrices respectively.
It can be seen that norm of $\mathbf{x}_k$ increases with k while the residual decreases with k.

When $\mathbf{V}_{22}$ is zero or near zero, $\mathbf{x}_k$ becomes very large, therefore it is appropriate to define a threshold value for $\mathbf{V}_{22}$ to limit the solution norm $(\|\mathbf{x}_k\|)$.

3.3.5. Lanczos Truncated Total Least Squares (LTTLS)

When the coefficient matrix is small, SVD matrix can be calculated easily and for different values of truncation parameter (k) the solution may be tested. However when the coefficient matrix is large, the TSVD and TTLS methods become unapplicable, because the SVD algorithm complexity is $O(mn^2)$ and tests for large k values are impractical. For these reasons, methods such as Lanczos bidiagonalization which minimizes size of the coefficient matrix without losing large singular values are used when solving discrete ill positioned problems. The combined version of Lanczos bidiagonalization and TTLS method is named as Lanczos TTLS method.

The Lanczos TTLS method is defined below:
As defined before at LSQR method, by using Lanczos bidiagonalization two matrices $\mathbf{U}_k = (\mathbf{u}_1, ...,\mathbf{u}_{k+1})$ and $\mathbf{V}_k = (\mathbf{v}_1, ..., \mathbf{v}_k)$ and a $(k+1)\times k$ bidiagonal matrix $\mathbf{B}_k$ produced. Where:

$$\mathbf{AV}_k = \mathbf{U}_k\mathbf{B}_k \quad \text{and} \quad \mathbf{Y} = \beta_1\mathbf{u}_1 \; . \tag{3.35}$$

When k is large enough to capture all singular values of $\mathbf{A}$ matrix, the TLS problem can be projected on the subspaces spanned by $\mathbf{U}_k$ and $\mathbf{V}_k$.

The TLS problem is applied to small sized matrix produced by Lanczos bidiagonalization to create a truncated TLS solution. To calculate TTLS solution SVD is applied to $(\mathbf{B}_k, \beta_1\mathbf{e}_1)$ matrix:

$$(\mathbf{B}_k, \beta_1\mathbf{e}_1) = \overline{\overline{\mathbf{U}}}^{(k)}\overline{\overline{\mathbf{S}}}^{(k)}(\overline{\overline{\mathbf{V}}}^{(k)})^T \; . \tag{3.36}$$

The $\overline{\overline{\mathbf{V}}}^{(k)}$ matrix is partitioned as:

$$\bar{V}^{(k)} = \begin{pmatrix} \overline{\bar{V}}_{11}^{(k)} & \overline{\bar{V}}_{12}^{(k)} \\ \overline{\bar{V}}_{21}^{(k)} & \overline{\bar{v}}_{22}^{(k)} \end{pmatrix} \begin{matrix} \updownarrow & k \\ \updownarrow & 1 \end{matrix}$$

$$\tag{3.37}$$

The standard TLS solution y_k is:

$$\bar{\mathbf{y}}_k = -\overline{\overline{\mathbf{V}}}_{12}^{(k)}(\overline{\bar{v}}_{22}^{(k)})^{-1} \; . \tag{3.38}$$

Then the regularized Lanczos TTLS solution $\tilde{\mathbf{x}}_k$ is:

$$\tilde{\mathbf{x}}_k = \mathbf{V}_k\,\bar{\mathbf{y}}_k = -\mathbf{V}_k\,\overline{\overline{\mathbf{V}}}_{12}^{(k)}(\overline{\bar{v}}_{22}^{(k)})^{-1} \; . \tag{3.39}$$

3.4. Regularization Parameter Selection Methods

Regularization parameter is a positive scalar tying to find a balance point while minimizing the norm of solution and norm of residual. Regularization parameter is symbolized as λ or k according to regularization parameter. Selecting small regularization parameter increases effects of high frequency elements of signal. This is called under regularization and no meaningful information about ECG signal is obtained. When large regularization parameter is selected, high frequency elements of signal is suppressed. This case is called over-regularization and causes a smoothing effect on the signal.

For these reasons, selecting a correct regularization parameter is an important stage in the inverse solution of problems. In this section, some of the regularization parameter selection methods; CRESO, GCV, L-curve, MCC will be explained.

3.4.1 .Composite Residual and Smoothing Operator

Composite Residual and Smoothing Operator (CRESO) is a commonly used regularization parameter selection method, applicable for continuous methods such as Tikhonov regularization. CRESO is firstly suggested by Colli Franzone [27].

The regularization parameter selected by CRESO t_{CRE} is the smallest value of $t>0$ which is the maximum of the function $C(t)$ [6, 28]:

$$C(t) = \|\mathbf{X}_t\|^2 + 2t\frac{d}{dt}\|\mathbf{X}_t\|^2 \quad , \tag{3.40}$$

where t is the λ parameter for Tikhonov method.
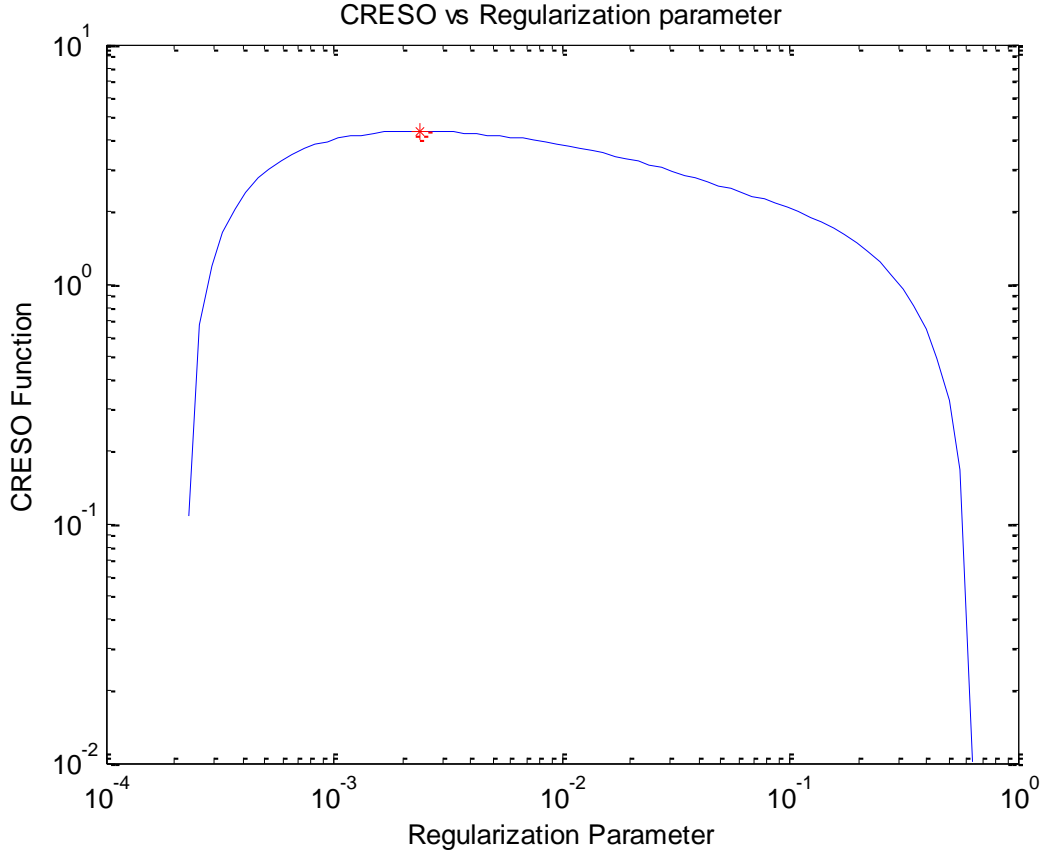
Figure 3.3: CRESO Plot

By using Singular value decomposition of transfer matrix $\mathbf{A} = \mathbf{USV}^T$, where $\mathbf{U}$ and $\mathbf{V}$ are orthanormal vectors and the diagonal entries of $\mathbf{S}$ is the singular values of $\mathbf{A}$ matrix, the solution $\mathbf{X}_t$ can be written as [6]:

$$\mathbf{X}_t = \sum_{i=1}^{n}\left(\frac{s_{ii}\alpha_i}{s_{ii}^2 + t}\right)\vartheta_i \quad , \tag{3.41}$$

where
s_{ii} are the diagonal elements of $\mathbf{S}$ matrix
α_i is the scalar product of $\mathbf{u}_i^T\mathbf{Y}$
$\mathbf{u}_i$ and ϑ_i are the columns of $\mathbf{U}$ and $\mathbf{V}$ matrices.
Since the matrices $\mathbf{U}$ and $\mathbf{V}$ are orthanormal, $\|\mathbf{X}_t\|^2$ can be written as:

$$\|\mathbf{X}_t\|^2 = \sum_{i=1}^{n}\frac{s_{ii}^2\alpha_i^2}{(t+s_{ii}^2)^2} \quad . \tag{3.42}$$

By using (3.42), (3.40) can be written as:

$$C(\lambda) = \sum_{i=1}^{n}\left[\frac{s_{ii}\alpha_i}{s_{ii}^2 + \lambda}\right]^2\left[1 - \frac{4\lambda}{s_{ii}^2 + \lambda}\right] \quad . \tag{3.43}$$

27

For different values of t, the *C(t)* function calculated, when the values are plotted the maximum of the plot is the CRESO regularization parameter t_{cre}.

3.4.2. Generalized Cross-Validation

Generalized cross-validation (GCV) is a mostly used, famous regularization parameter selection method, determining appropriate values of parameters such as the regularization parameters λ in Tikhonov regularization or truncation number *k* in truncated singular value decomposition and truncated total least squares. It is based on statistical considerations, such as a good regularization parameter converges to real data, and predicts missing data values. GCV is based on the idea that if a random element Y_i of right hand side **Y** is skipped, then the calculated solution should guess this observation. The choice of regularization parameter should be free of orthogonal transformation of **Y** [25, 26].
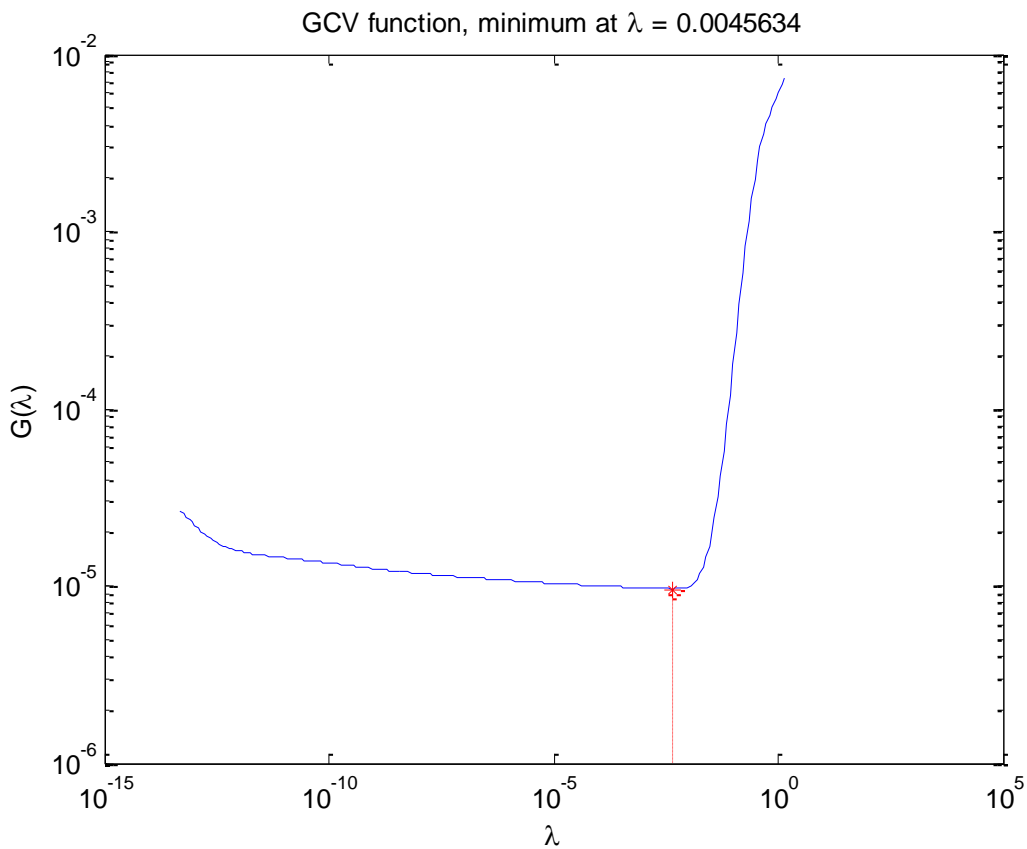
Figure 3.4: GCV Plot

GCV method looks for a regularization parameter value which minimizes mean square error $\|Ax_{lambda} - Y^{exact}\|$ value. Because the exact value of right hand side **Y** element is unknown, GCV methods use the following equation to predict correct regularization parameter:

$$G(\lambda) = \frac{\|Ax_{\lambda} - Y\|_2^2}{\text{trace}(I_m - AA^I)^2} \qquad , \tag{3.44}$$

where A^I is the matrix that produces regularized solution x_{lambda} when multiplied with torso potentials **Y** ($x_{lambda} = A^I Y$). Different from CRESO, GCV is defined for both discrete and continuous regularization parameters.

The denominator can be written as:

28

$$\text{trace}(\mathbf{I}_m - \mathbf{A}\mathbf{A}^I) = m - (n-p) - \sum_{i=1}^{p} f_i = m - p(lambda) \quad , \tag{3.45}$$

where m and n are dimensions of transfer matrix, p is the number of filter factors and f_i is the filter factors.

3.4.3. L-Curve Method

L-curve is a well- known method, firstly introduced by Hansen [80] to find finest regularization parameter. L-curve is a log-log plot of norm of regularized solution $\left\| \mathbf{X}_{est}^i \right\|$ versus norm of the residual solution $\left\| \mathbf{A}\mathbf{X}_{est}^i - \mathbf{Y} \right\|$ for different values of regularization parameter (i) [88].

$$(x_i, y_i) = \left(\log_{10} \left\| \mathbf{A}\mathbf{X}_{est}^i - \mathbf{Y} \right\|, \log_{10} \left\| \mathbf{X}_{est}^i \right\| \right) \text{ for } i = 1,2,....,p \quad , \tag{3.46}$$

where p is the number of regularized solutions.

When a log-log scale the $\left\| \mathbf{X}_{est}^i \right\|$ values are plotted on ordinate against the $\left\| \mathbf{A}\mathbf{X}_{est}^i - \mathbf{Y} \right\|$ values on the abscissa, the graph looks like a 'L' letter. The correct regularization value (i) is found at the point of the maximal curvature of the L-curve which is the value at the vertex of L curve. The value at the vertex corresponds to best approximate solution of Equation (3.1). A typical L-curve is shown in the Figure 3.5 and the corner of the L-curve is marked with red lines:
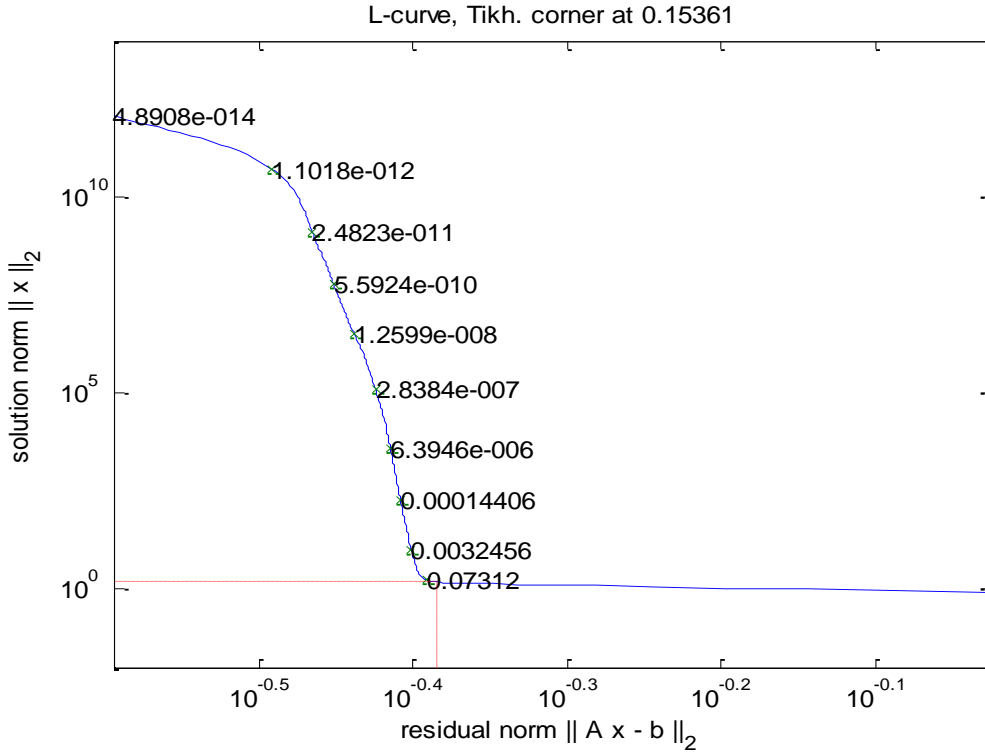
Figure 3.5: A typical L-curve plot

The horizontal part of the L-curve is dominated by the regularization error, while the vertical part shows the sharp increase in the norm caused by propagation errors [88].

3.4.4. Maximum CC Method

Maximum correlation coefficient (MCC) method is not a suitable method for clinical life usage, because it uses real epicardial potentials to determine regularization parameter. In this approach, first

29

the number of regularization number to be tried is decided then upper and lower limits of the regularization parameters also decided. Finally, for all of the regularization parameters, corresponding regularization method solutions are obtained. These results are compared with real epicardial potentials and the one giving maximum cc is selected as a regularization parameter. MCC is important to measure the performance of regularization methods by eliminating effects of the regularization parameter selection methods.

CHAPTER 4

RESULTS AND DISCUSSION

In this chapter, we first explain the simulation data used for solving the inverse problem, and then we give the reconstruction results of inverse ECG problem for different regularization methods.

4.1. Experimental Data

Body surface potentials used in this thesis are obtained from the QRS interval of measured epicardial potentials and a forward transfer matrix, which was conducted as a Tübitak research previously.

The true epicardial potentials used for the simulation of body surface potentials were measured by R. S. MacLeod and his coworkers at the University of Utah, Nora Eccles Harrison Cardiovascular Research and Training Institute (CVRTI) [81, 82]. These epicardial potentials were obtained from an isolated dog heart using a nylon sock electrode with silver wires slipped over the ventricles. The epicardial potentials were measured from 490 points at a rate of 1000 samples per second. To obtain realistic results, a heart taken from a dog was perfused from circulatory system of another dog and placed into an electrolytic filled (500 Ωcm) adolescence human thorax-shaped fiberglass tank.

During measurements, the heart was stimulated from the ventricles to simulate ventricular arrhythmias and the epicardial potentials are recorded for 97 time instants. In Figure 4.1, different time instants during QRS cycle are given and it can be seen that initial activation starts from the ventricle and propagates all over the epicardial surface during time. At time instant 2, most of the epicardial surface is at rest and measured voltages from most of the points are approximately zero. When time passes size of the activated region gets larger and at time instants 39, 51 and 63, most of the epicardial surface activated, therefore larger values are measured at epicardial points. After time instant 70, it can be seen that activation is propagated all over the epicardial surface; however measured voltage values at epicardial nodes start to decrease, because effect of the initial activation starts decreasing.

The forward transfer matrix relating the measured epicardial potentials to the body surface potentials is calculated using BEM [56]. The thorax model used for simulation of the measurements consists of heart, lungs and thorax. The conductivity values of lungs and thorax are selected as reported in literature [83] and a transfer matrix relating torso potentials to epicardial potentials is formed.

This forward transfer matrix calculated by BEM method is then used to obtain body surface potential recordings at 771 nodes on the body surface form epicardial potential measurements from 490 points on the heart surface. First, measured epicardial potentials are multiplied by the transfer matrix to obtain noiseless body surface potentials (torso potentials). Different levels of independent and identically distributed Gaussian noise are added to these noiseless torso potentials to obtain noisy body surface potentials used for simulations. The flowchart for simulating body surface potentials from the epicardial potentials is shown in Figure 4.2.
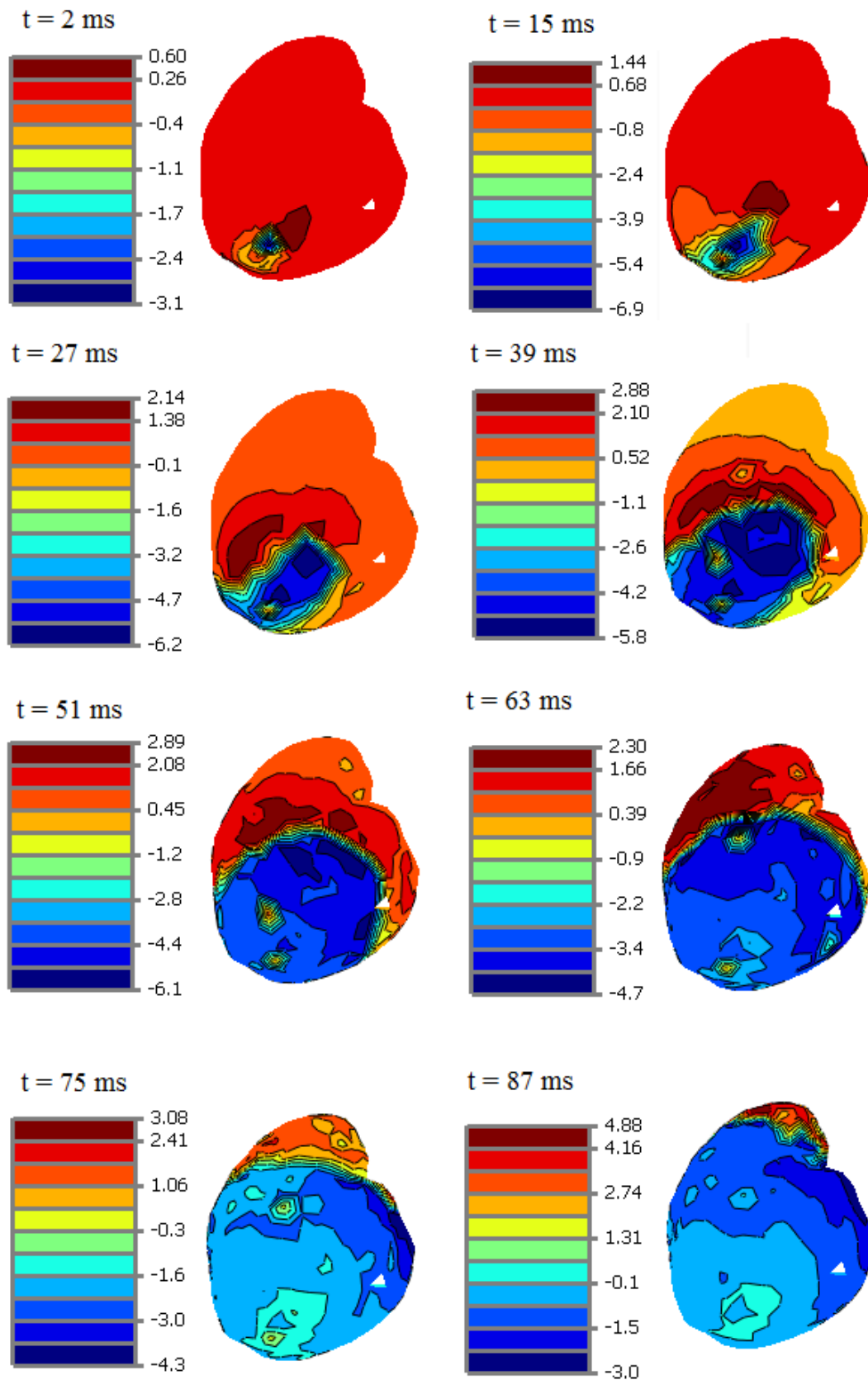
Figure 4.1: Propagation of initial activation on epicardial surface during time
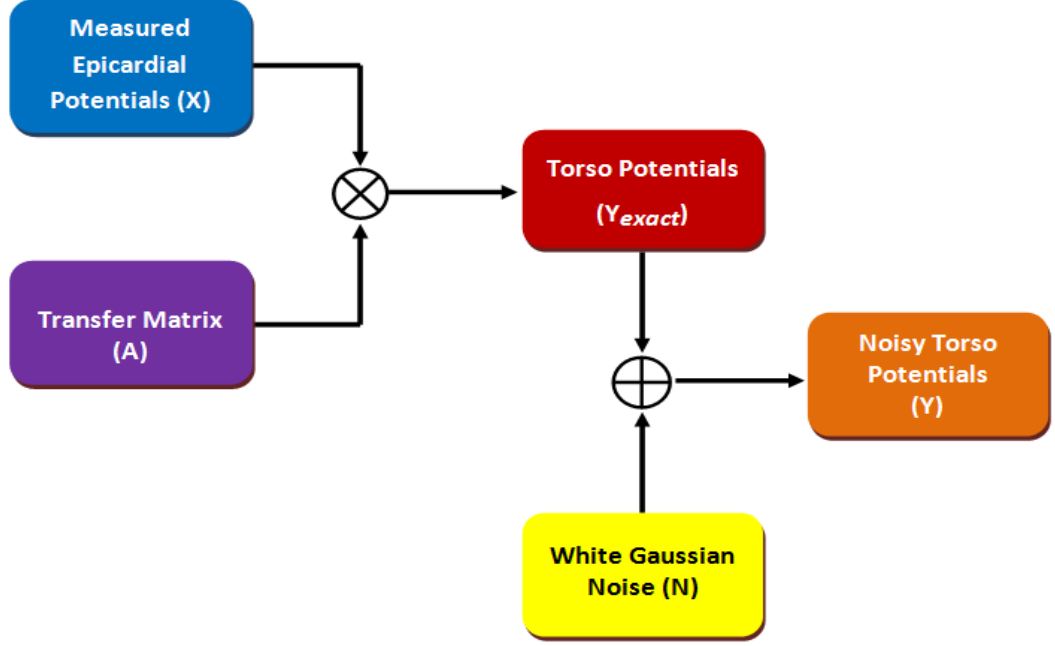
Figure 4.2: Schematic representation of forward problem of ECG

From Figure 4.2, noisy torso potential matrix **Y** can be calculated as:

$$\mathbf{Y}_{exact} = \mathbf{AX} \qquad . \tag{4.1}$$

By using Equation 4.1, Equation 3.1 can be written as:

$$\mathbf{Y} = \mathbf{Y}_{exact} + \mathbf{N} \quad , \tag{4.2}$$

where $\mathbf{A} \in R^{mxn}$ is the transfer matrix, $\mathbf{X} \in R^{nxt}$ is the measured epicardial potentials, $\mathbf{Y}_{exact} \in R^{mxt}$ is the noiseless torso potentials, $\mathbf{N} \in R^{mxt}$ is the white Gaussian noise and $\mathbf{Y} \in R^{mxt}$ is the noisy torso potentials. Here, we assume that there are m measurement electrodes on the body surface, n nodes on the epicardial surface, and the signals are measured at t different time instances.

4.2. Evaluation Criteria

The quantitative comparisons of the reconstructed potentials obtained by different inverse EGC methods are achieved by Relative Difference Measurement Star (RDMS), and Correlation Coefficient (CC):

$$\text{RDMS}(k) = \sqrt{\frac{\mathbf{X}_{est}(:,k)}{\sum_{i=1}^{n} x_{est_i}{}^2(:,k)} - \frac{\mathbf{X}(:,k)}{\sum_{i=1}^{n} x_i{}^2(:,k)}} \quad , \tag{4.3}$$

$$\text{CC}(k) = \frac{\sum_{i=1}^{n}[x_{est_i}(:,k) - \bar{\mathbf{X}}_{est}(:,k)] \cdot [x_i(:,k) - \bar{\mathbf{X}}(:,k)]}{\left\| \mathbf{X}_{est}(:,k) - \bar{\mathbf{X}}_{est}(:,k) \right\|_2 \cdot \left\| \mathbf{X}(:,k) - \bar{\mathbf{X}}(:,k) \right\|_2} \quad , \tag{4.4}$$

where, k is the time instant, n is the number of epicardial nodes, $\mathbf{X}_{est}$ is the estimated solution by regularization methods, $\mathbf{X}$ is the real epicardial potentials, $\bar{\mathbf{X}}_{est}$ is the mean of the estimated solution and $\bar{\mathbf{X}}$ is the mean of the real epicardial potentials. From these formulations, it is obvious that higher CC or lower RDMS values mean that the method performs better.

Another measure to assess the performance of an inverse solution method is to compare the reconstructed activation wavefront to the original one. Since RDMS and CC do not give information about the quality of the wavefront reconstruction, a visual evaluation method is needed. For this purpose a scientific visualization application named Map3d written by Utah Nora Eccles Harrison

Cardiovascular Research and Training Institute is used [29]. By using Map3d program, three-dimensional geometric models and time-based data associated with those models can be displayed and edited.

In Figure 4.3, epicardial potential distribution (left) and the corresponding body surface potential map for a single time instant are shown. In the epicardial potential map, blue regions represent the activated regions, and red regions represent the regions that have not been activated yet. The transition region between those two is the activation wavefront. While visually comparing Map3d figures, two important characteristics are considered:

1. The solution's ability to follow the wavefront without dispersing it much. The dispersion in the wavefront is due to smoothing effects of the regularization methods.

1. The solution's ability to separate the activated or inactivated regions.
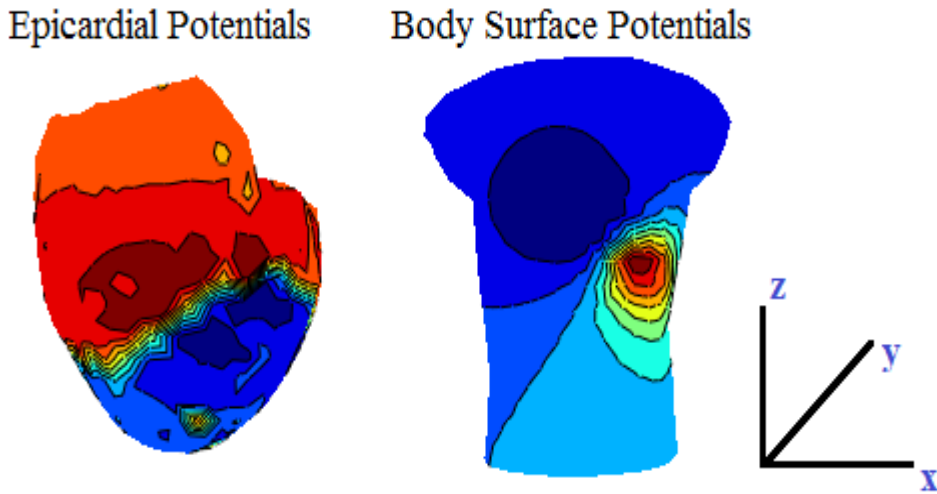
Figure 4.3: Epicardial potential distribution and body surface potential map

Another performance measurement for regularization methods is the process time, faster methods are more preferable.

4.3. Simulations

In this section, we first assess the performances of the regularization parameter selection methods. Applicable regularization parameter selection methods are implemented for each of our regularization methods: Tikhonov, TSVD, LSQR, TTLS and LTTLS. Performance comparison is done for the following parameter selection methods:
- L –curve,
- GCV,
- CRESO,
- Max CC.

According to performances of regularization parameter selection methods, the most appropriate regularization parameter selection method is selected for each regularization method. Among these regularization methods, CRESO is only applicable for continuous methods; therefore it is tested only for Tikhonov method.

Next, performance comparison is done for the following methods:

- Tikhonov Regularization,
- Truncated Singular Value Decomposition Method,
- Least Square – QR Method,
- Truncated Total Least Squares Method,
- Lanczos Truncated Total Least Squares Method.

Each of these methods are compared,

a) by using a regularization parameter determined by the maximum CC method,
b) by using the regularization parameter estimated by the most appropriate parameter selection method for each regularization method. Here, "the most appropriate parameter selection method" means that it was chosen as the method that yields the best results in the first study.

While comparing the performances of our regularization methods, different levels of measurement noise are applied. Measurement noise is simulated as independent and identically distributed (i.i.d.) white Gaussian noise, and the noise level is defined according to average amplitude of noise (σ_n). For our simulations, two different σ_n values are applied: 15 µV and 150 µV, which correspond to 30 dB and 10 dB SNR levels, respectively.

The effects of geometric errors are also important in inverse ECG problem. Studies show that incorrect geometric interpretations are more significant than the conductivity errors in the torso model [52, 84]. For these reasons, the effects of incorrect geometric interpretations of the torso model will be examined in this thesis.

To include geometrical errors in our model, first body surface potential measurements were simulated as shown in Figure 4.4, by using the real transfer matrix, *i.e.*, the matrix found by using the heart-lung-torso model. 15 µV measurement noise was also added to the data. During inverse calculations, a geometric error added transfer matrix is used. To add geometric error to the transfer matrix, a faulty torso mesh is used. We considered two different ways to obtain a faulty mesh:
- Changing the location of the heart in the torso.
- Changing the size of the heart.

These two conditions occur during the movement of the heart while measuring torso potentials from the body surface in real life.

When the effects of a change in the heart's location are examined, the heart is shifted from its original location by 6 to 15 mm in the x, y or z directions. In this study, x-axis points from right to left (of the body), y-axis points from front to back and z-axis points from down to up as seen in Figure 4.3. Then, this faulty mesh is used to calculate the transfer matrix for inverse solution.

The size changes of the heart are simulated by multiplying the heart's real coordinates by a scalar value in a range of 0.6 to 1.4 and this faulty mesh is used to calculate the transfer matrix. For example, multiplying the heart's size by 0.9 means, 10 % decrease in the size of the heart, and multiplication by 1.1 means 10 % increase in the size of the heart. Finally these errors are combined and both the heart's size and the location are changed simultaneously. The geometric error simulation procedure is shown in Figure 4.4.

Figure 4.4: The schematic representation of the simulation procedure to study geometric errors

4.4. Performances of Regularization Parameter Selection Methods

In this section, regularization parameter selection methods L-curve, GCV and max CC have been used to determine the appropriate parameter for each regularization method. The aim of this study is to determine the best regularization selection approach for each method. In addition, CRESO has been included in the parameter selection methods for Tikhonov regularization; CRESO is a continuous function of the regularization parameter, and cannot be used for methods that have integer regularization parameters.

4.4.1. Performances of Regularization Parameter Selection Methods for Tikhonov Regularization

In this section, lambda (λ) value of Tikhonov regularization method is selected by different regularization methods for different noise levels. These methods are L-curve, GCV, CRESO and max CC methods. For comparison of performances of these methods, 15 µV (~30 dB SNR) and 150 µV (~10 dB SNR) Gaussian white noise is added to torso data and inverse ECG problem is solved using Tikhonov regularization method.

In Figure 4.5, average lambda values for different noise levels are illustrated. This figure shows that average lambda values found by L-curve and CRESO methods are larger than other methods. These methods fail when the solution is smooth especially first time instants when the excitation has just started. This problem of L-curve has also been reported in the literature [25]. Among these methods, GCV finds similar lambda values to max CC method especially at 15 µV case. These values are also given in Table 4.1 for 15 µV and 150 µV cases.
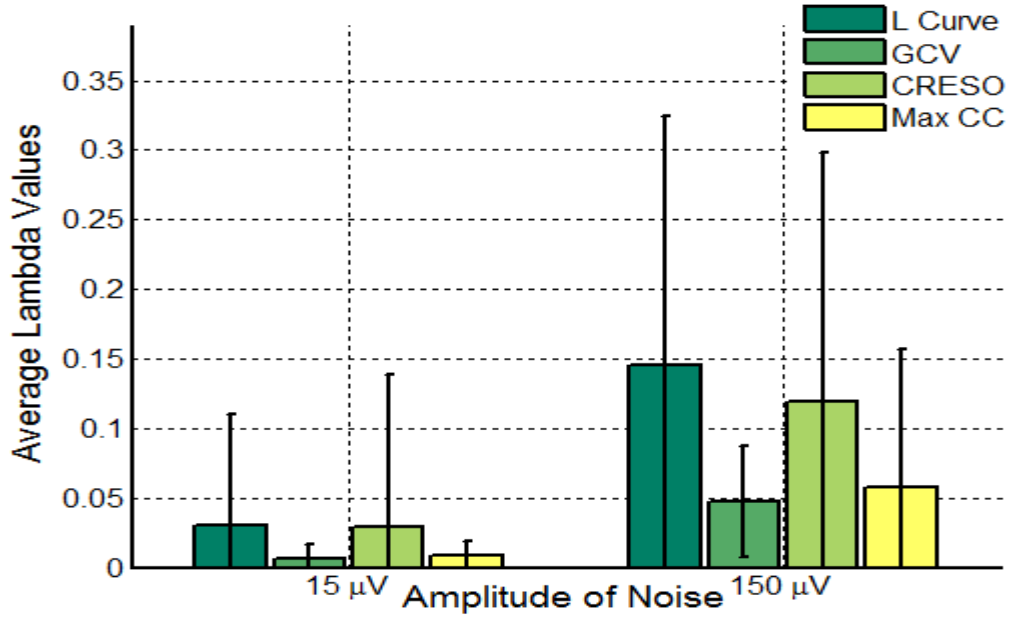
Figure 4.5: Average Lambda Values with respect to Amplitude of noise graph of four regularization parameter selection methods for Tikhonov Method

Table 4.1: Mean and standard deviation values of lambda, CC and RDMS values of different regularization parameter selection methods at 15 and 150 µV measurement noise

	Methods	Avg. Lambda values	CC Values	RDMS
15 µV measurement noise	L-curve	0.0303 ± 0.08	0.77 ± 0.20	0.60 ± 0.21
	GCV	0.0065 ± 0.01	0.78 ± 0.15	0.60 ± 0.18
	Max CC	0.0086 ± 0.01	0.80 ± 0.14	0.58 ± 0.17
	CRESO	0.0287 ± 0.11	0.78 ± 0.19	0.60 ± 0.20
150 µV measurement noise	L-curve	0.1450 ± 0.18	0.58 ± 0.29	0.82 ± 0.26
	GCV	0.0476 ± 0.04	0.64 ± 0.22	0.77 ± 0.22
	Max CC	0.0573 ± 0.10	0.67 ± 0.20	0.75 ± 0.21
	CRESO	0.1187 ± 0.18	0.62 ± 0.26	0.80 ± 0.26

Figure 4.6: a) Average Correlation Coefficient vs Amplitude of noise graph of four regularization parameter selection methods for Tikhonov Method b) Average RDMS vs Amplitude of noise graph of four regularization parameter selection methods for Tikhonov Method

38
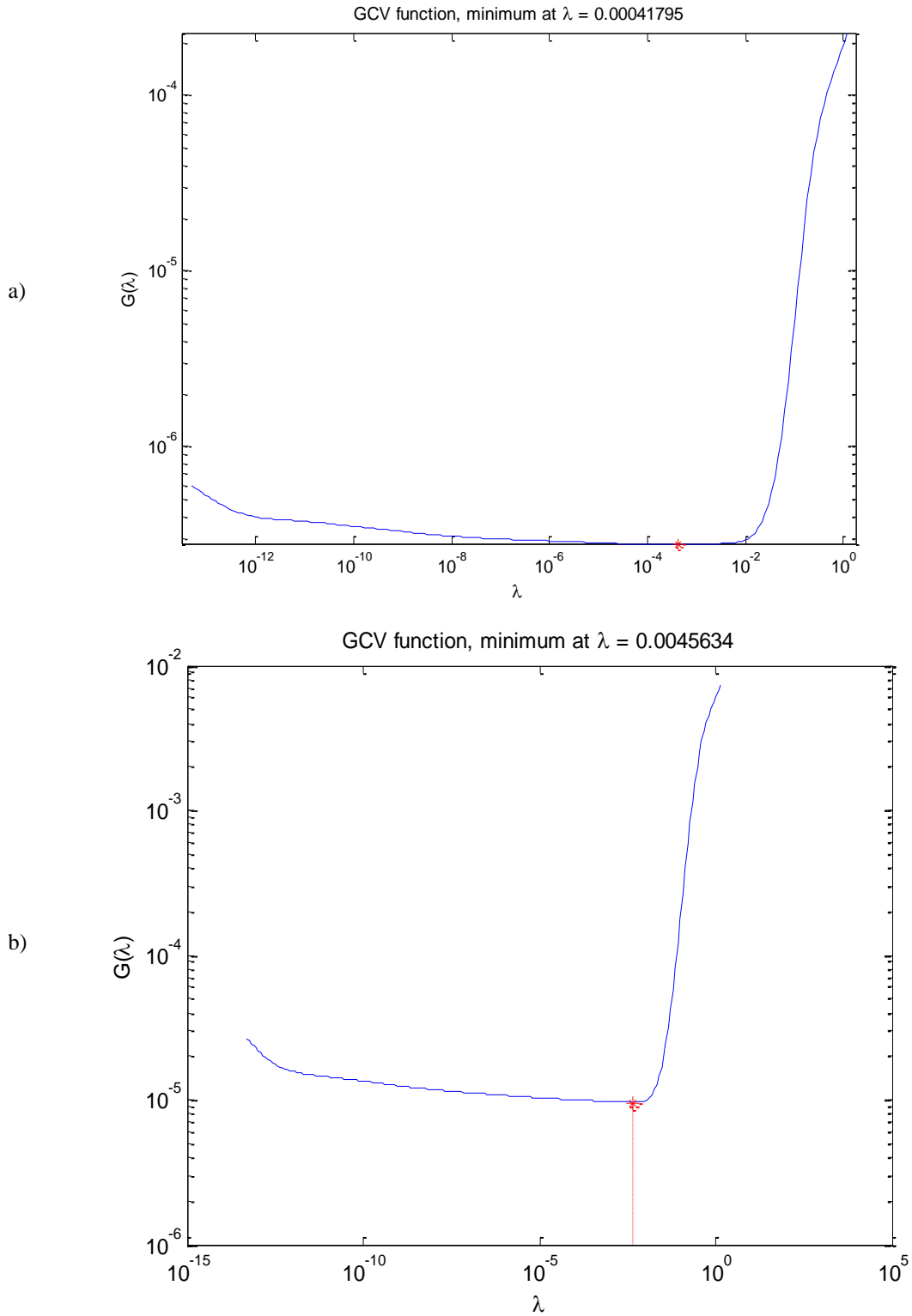
Figure 4.7: Lambda value selected by GCV method at a) time instant 60 ms b) time instant 55 ms.

Figure 4.6.a and Figure 4.6.b show the average CC and RDMS values for the regularization parameter selection methods. When Figure 4.6.a and Figure 4.6.b are inspected, it is seen that GCV, CRESO and L-curve have similar results, and these results are comparable to max CC method. Average and standard deviation values of CC and RDMS values are also given in Table 4.1. According to this table, average CC values for GCV is slightly larger than those obtained for the L-

curve and CRESO methods, because of the failures of the latter methods at initial time instants. Similar results are also obtained when RDMS values are inspected. Among these methods, max CC method gives the best results as we have expected; however it is not applicable in real cases, and only here for comparison purposes. The GCV results reported here have been obtained using a modified GCV approach as explained in the following paragraphs.

Normally, GCV method may cause some spikes (*i.e.*, sudden drops to low CC values) at a few time instants. The reason of this problem is the small lambda value selection of GCV method at some time instants, therefore; at these time instants RDMS values increase and CC values decrease. It is observed that the largest spike occurred at 60 ms after excitation, for this reason GCV function vs. lambda graphs used for lambda selection at 60 ms (problematic case) and at 55 ms (a normal case) are given Figure 4.7.

When Figure 4.7.a is inspected, lambda value selected by the GCV method at this time instant is 4.17×10^{-4}, but according to Figure 4.7.b normal lambda values are 10 times greater than this value. In Figure 4.7.a, it is seen that GCV function has similar values for lambda values larger than 10^{-5}; therefore when there is a flat region near the minimum value of GCV function, the largest lambda value as shown in Figure 4.8 is selected and better results are obtained by this way; the CC value has been 0.37 with the GCV method (lambda = 4.17×10^{-4}), it has been increased to 0.81 with the modified GCV method (lambda = 3.24×10^{-3}).
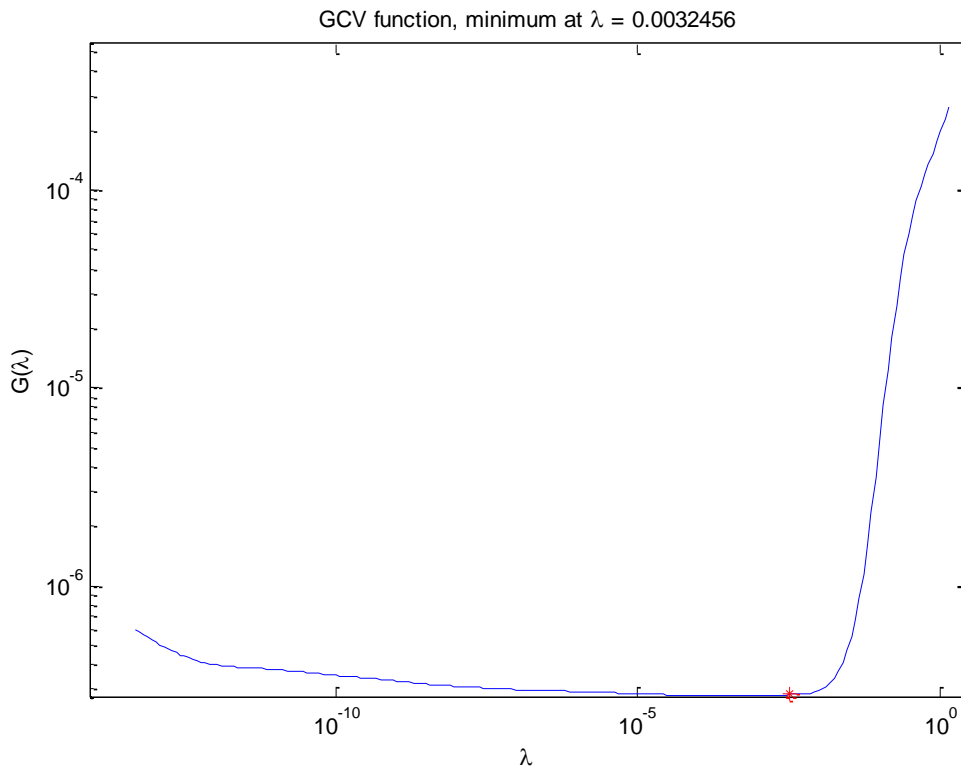
Figure 4.8: Lambda value selected by modified GCV method at time instant 60 ms

4.4.1.1. Discussion on results of regularization parameter selection methods for Tikhonov regularization

When all of the information about performances of regularization parameter selection methods is considered, the best results are obtained by max CC method; however it is not applicable in real cases because epicardial potentials are not known. L-curve and CRESO methods have some problems at initial time instants when the solution is very smooth. CRESO is also applicable for only continuous method, for these reason it is not a widely used method. Among these methods, the

modified GCV is a robust method for determination of lambda value for Tikhonov regularization. It is also given that, GCV and L-curve give very similar average relative error values, but GCV has larger maximum relative errors, when the minimum of GCV curve is very flat [75], by modified GCV this problem is overcomed.

4.4.2. Performances of Regularization Parameter Selection Methods for the LSQR Method

In this section, optimum iteration number for LSQR method is selected by different parameter estimation methods (L-curve, GCV and max CC method), and for different noise levels. For comparison of performances of these methods, 15 µV (30 dB SNR) and 150 µV (10 dB SNR) Gaussian white noise is added to torso data and inverse ECG problem is solved using the LSQR method.


Figure 4.9: Average Iteration Number with respect to Amplitude of noise graph of four regularization parameter selection methods for LSQR Method
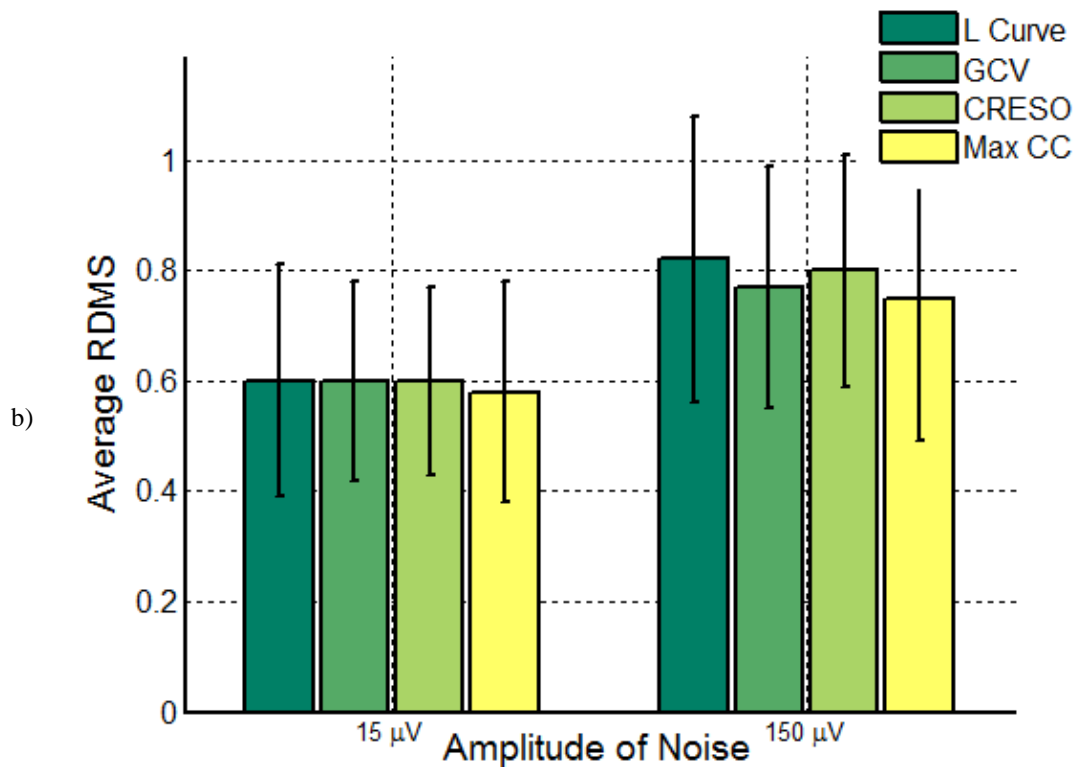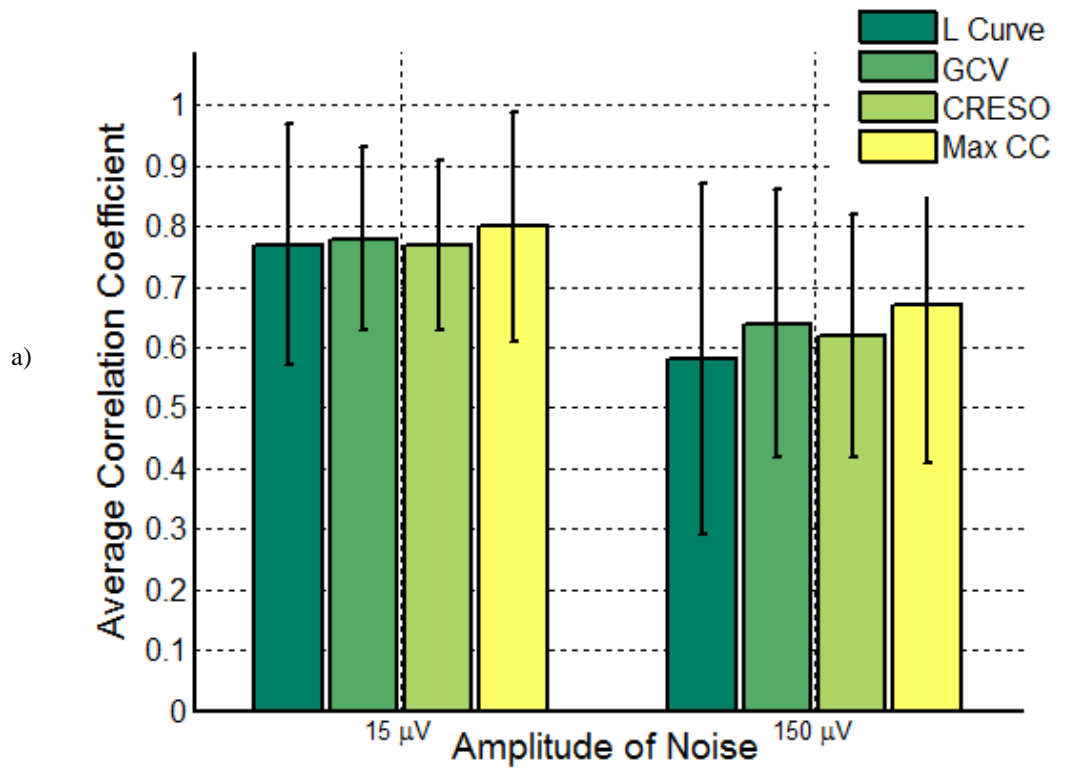
a)

b)

Figure 4.10: a) Average Correlation Coefficient vs Amplitude of noise graph of three regularization parameter selection methods for the LSQR Method b) Average RDMS vs Amplitude of noise graph of three regularization parameter selection methods for the LSQR Method.

In Figure 4.9, average iteration numbers for different noise levels are illustrated. Since non-integer iteration number is meaningless, these averages are rounded to the nearest integer. In this figure, it is seen that average iteration numbers found by the L-curve are larger than those estimated by the GCV method, because similar to Tikhonov case, L-curve fails when the solution is smooth (especially at the first time instants when the excitation has just started and the last time instants at the end of the excitation). Selection of larger iteration numbers causes under smoothing of the solution. Among these methods, GCV finds similar lambda values to max CC method, especially at 150 µV case. These values are also presented at Table 4.2 for the 15 µV and 150 µV cases.

Figure 4.10.a and Figure 4.10.b show the average CC and RDMS values of regularization parameter selection methods. When Figure 4.10.a and Figure 4.10.b are inspected, it is seen that GCV and L-curve have similar results for the 15 µV measurement error case. Averages and standard deviations of CC and RDMS values are also given in Table 4.2. According to this table, average CC values for GCV are larger than those of the L-curve method for the 150 µV case. The L-curve method has especially poor performance at the initial time instants and at some other times when the L-curve does not have a distinctive corner as expected from the L-curve method (for example, see Figure 4.11). Similar results are also obtained when the RDMS values are inspected. Among these methods, max CC method again gives the best results.

Table 4.2: Mean and standard deviation values of iteration number, CC and RDMS values of different regularization parameter selection methods for 15 and 150 µV measurement noise

	Methods	Avg. Iteration Num.	CC Values	RDMS
15 µV measurement noise	L-curve	18 ± 2	0.77 ± 0.20	0.61 ± 0.23
	GCV	17 ± 5	0.80 ± 0.14	0.58 ± 0.17
	Max CC	18 ± 5	0.80 ± 0.14	0.58 ± 0.17
150 µV measurement noise	L-curve	11 ± 8	0.56 ± 0.29	0.86 ± 0.31
	GCV	6 ± 2	0.65 ± 0.20	0.77 ± 0.21
	Max CC	6 ± 2	0.67 ± 0.19	0.75 ± 0.20

LSQR is an iterative method; therefore calculation of filter factors is not possible. For this reason, it is not easy to obtain the denominator of the GCV function given in Equation 3.44. For these cases, sum of the filter factors can be approximated as the number of converged Ritz values [75] and GCV function can be written as:

$$G(k) = \frac{\|\mathbf{A}\mathbf{x}_k - \mathbf{Y}\|_2^2}{m - l_k} \tag{4.5}$$

where, l_k is the number of converged Ritz values. Since iteration number is very small when compared to m, the approximated GCV function can be written as:

$$G(k) = \frac{\|\mathbf{A}\mathbf{x}_k - \mathbf{Y}\|_2^2}{m - k} \tag{4.6}$$

where k is the number of iteration. The GCV function for LSQR, TSVD, TTLS and Lanczos TTLS methods is calculated as given in Equation 4.6.
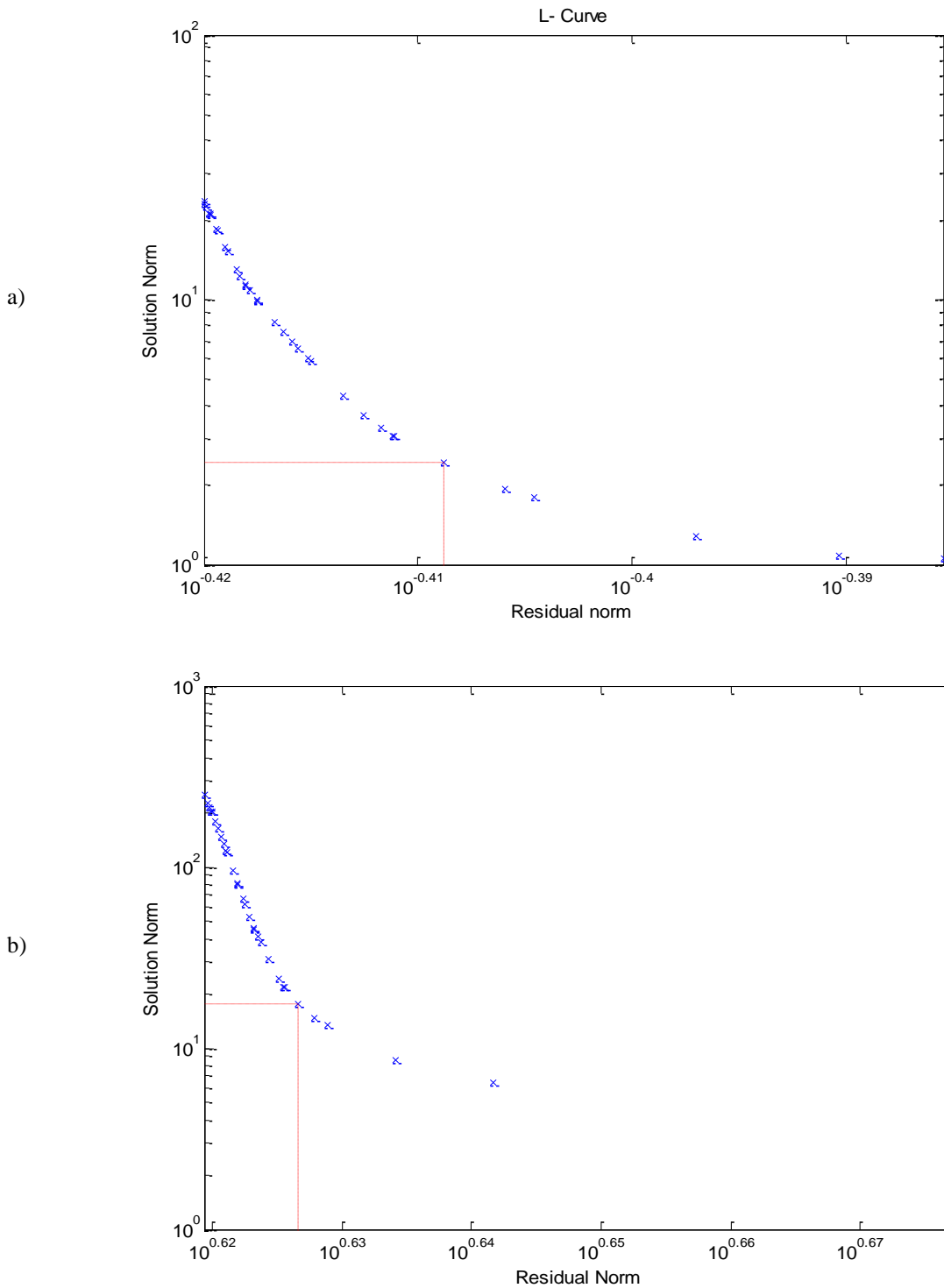
Figure 4.11: a) L-curve plot at time instant 2 for 15 µV case b) L-curve plot at time instant 21 for 150 µV case

Determination of the corner of the L-curve is another difficulty for discrete-parameter methods when compared with the continuous-parameter methods like Tikhonov, because in continuous methods calculation of the derivative of the curve is easy and the curvature of L-curve can be easily computed. For discrete L-curves, corner of the L-curve can be found by different methods such as: spline curve method [85], triangle method [85] and adaptive pruning algorithm [85]. Among these

44

methods, triangle method is used for determination of the corner of the L-curve, because it gives better results than the spline curve method in most cases and implementation is easier among these methods [85]. The key point of the triangle method is to define three points on the curve and select the one with minimum angle. If all angles are smaller than - $\pi/8$, the left point is selected. Selected three points are as follows:

($\underline{P_j}$;P_k;P_n)   where $j = 1;\ ...\ ;\ n-2$ and $k = j + 1;\ ...\ ;\ n$ - 1

The triangle method's algorithm is given below:

- Remove points with zero norm
- Initialize $c_{max} = -2$
- for $k = 1,..., n$- 2
    - for j = k + 1; : : : ; n − 1
        - Compute vectors: $\mathbf{v}_1 = P_k$ - P_j and $\mathbf{v}_2 = P_j$ - P_n
        - Compute: $c = \frac{-\mathbf{v}_1{}^T \mathbf{v}_2}{\|\mathbf{v}_1\|_2 \|\mathbf{v}_2\|_2}$
        - Compute: $w = \det([\mathbf{v}_1 ; \mathbf{v}_2])$
        - if $c > \cos(7*\pi/8)$ and $c > c_{max}$ and $w < 0$
            - Set: *corner* $= j$ and $c_{max} = c$
        - end
    - end
- end

The main problem of the triangle method is increased complexity of the algorithm because of the two for loops which increases complexity to $O(n^2)$.

4.4.2.1. Discussion on results of regularization parameter selection methods for LSQR Method

When all of the information about performances of regularization parameter selection methods is considered, best results are obtained by the max CC method; however it is not applicable in real cases because epicardial potentials are not known. L-curve method has some problems at initial time instants when the solution is very smooth. Furthermore, smooth L-curves with no distinctive corners yield incorrect corner estimates at some of the time instants, especially for the high-noise data. GCV also have some problems when the minimum region is flat, however selecting rightmost point (i.e., the modified GCV method) gives good results. For these reasons, among these methods, the modified GCV is a robust method for determination of the iteration number for the LSQR method.

4.4.3. Performances of Regularization Parameter Selection Methods for TSVD Method

In this section, truncation number for the TSVD method is selected by different regularization parameter estimation methods (L-curve, GCV and max CC method) for different noise levels. For comparison of performances of these methods, 15 µV (30 dB SNR) and 150 µV (10 dB SNR) Gaussian white noise is added to torso data and inverse ECG problem is solved using the TSVD method.
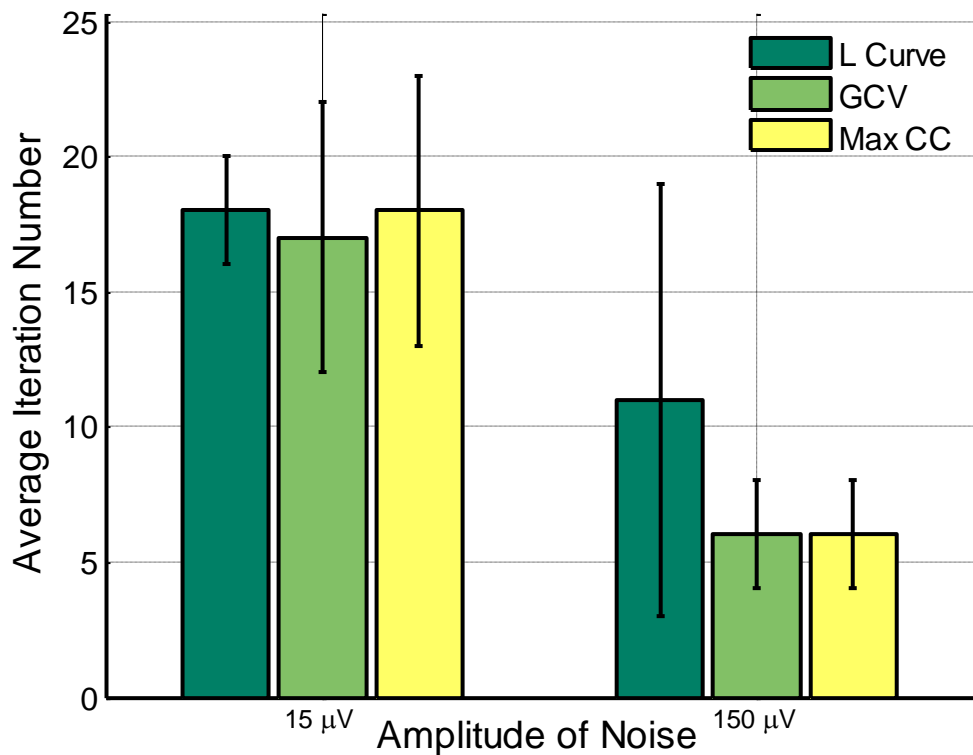
Figure 4.12: Average Truncation Number with respect to Amplitude of noise graph of three regularization parameter selection methods for TSVD Method
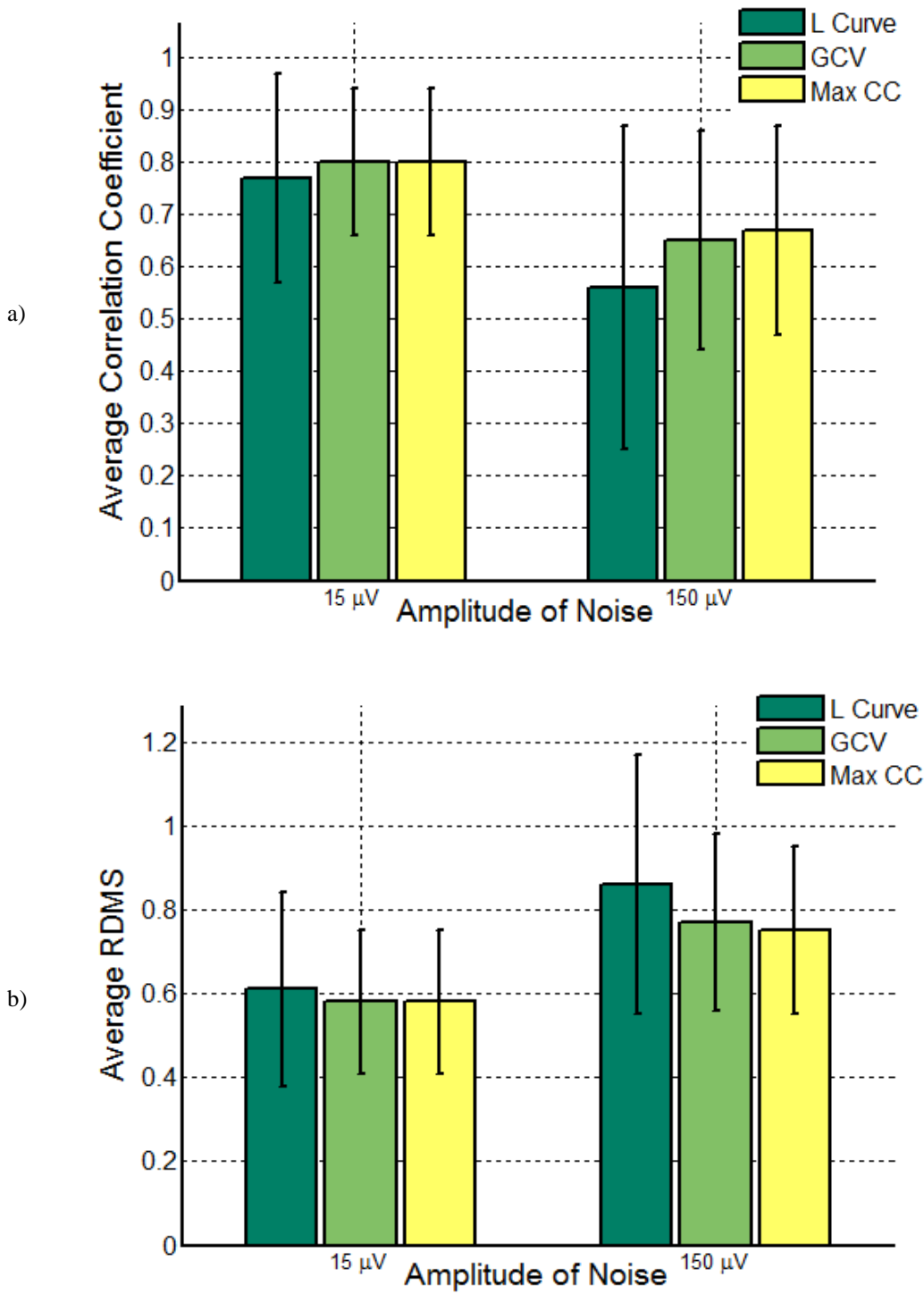
In Figure 4.12, average truncation numbers for different noise levels are illustrated, since non-integer truncation number is meaningless, they are rounded to the nearest integer. In this figure, it is seen that for 15 µV case average truncation numbers found by L-curve and GCV are comparable, but when the amplitude of noise is increased to 150 µV, it is seen that different average truncation numbers are obtained. At 150 µV case, the under smoothing effect of L-curve (larger truncation numbers) and over smoothing property of GCV (smaller truncation numbers) is seen. These values are also given in Table 4.3 for the 15 µV and 150 µV cases.

Table 4.3: Mean and standard deviation values of truncation, CC and RDMS values of different regularization parameter selection methods for 15 and 150 µV measurement noise

	Methods	Avg. Truncation Num.	CC Values	RDMS
15 µV measurement noise	L-curve	27 ± 2	0.77 ± 0.18	0.62 ± 0.20
	GCV	26 ± 5	0.78 ± 0.15	0.60 ± 0.17
	Max CC	26 ± 5	0.79 ± 0.14	0.59 ± 0.17
150 µV measurement noise	L-curve	15 ± 2	0.62 ± 0.22	0.81 ± 0.23
	GCV	12 ± 4	0.64 ± 0.22	0.78 ± 0.21
	Max CC	13 ± 4	0.67 ± 0.18	0.75 ± 0.20

Figure 4.13: a) Average Correlation Coefficient vs Amplitude of noise graph of three regularization parameter selection methods for TSVD Method b) Average RDMS vs Amplitude of noise graph of three regularization parameter selection methods for TSVD Method

a)

b)
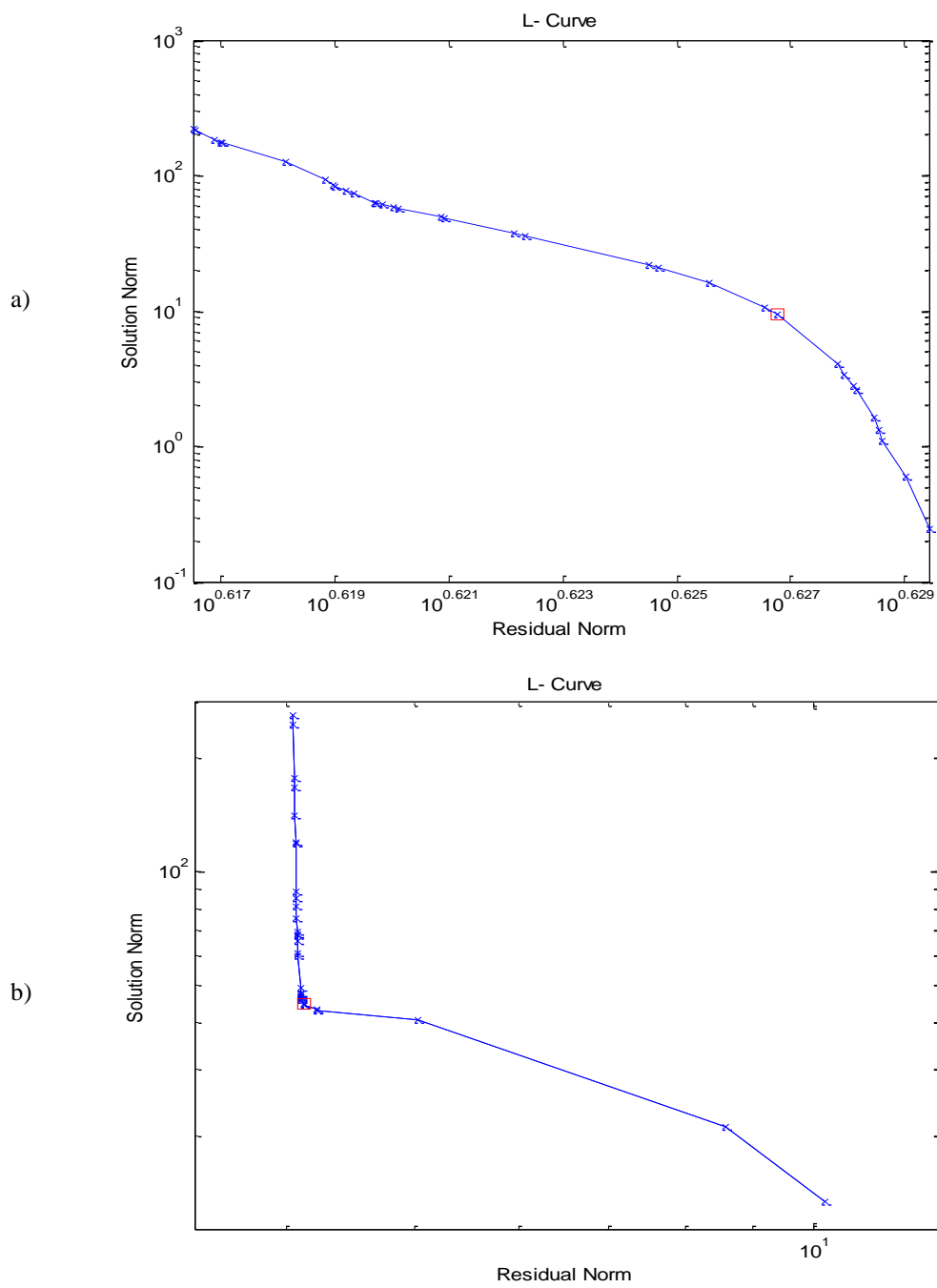
Figure 4.14: a) L-curve plot at time instant 8 for 150 µV case b) L-curve plot at time instant 63 for 150 µV case
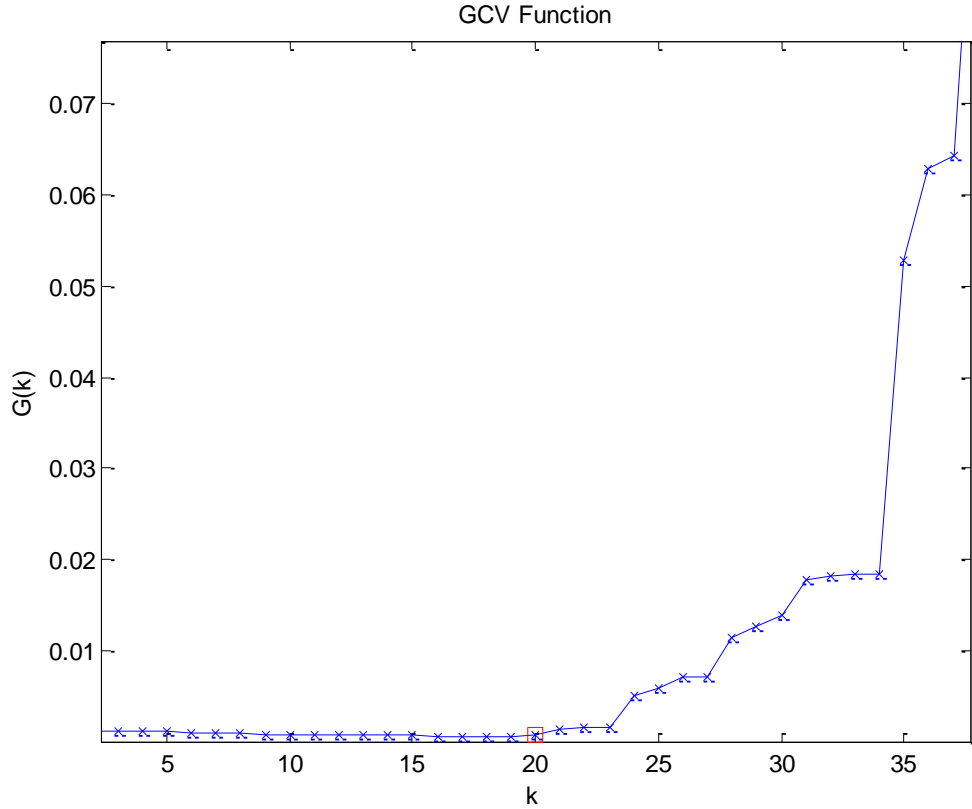
Figure 4.15: GCV plot at time instant 29 for 150 µV case

Figure 4.13.a and Figure 4.13.b show the average CC and RDMS values of regularization parameter selection methods. When Figure 4.13.a and Figure 4.13.b are inspected, it is seen that GCV method is a bit better than L-curve method for 15 µV measurement error case. For 150 µV measurement error case, it is seen that the performance difference between GCV and L-curve is increased and GCV gave better results. Max CC method gives the best results as expected. Average and standard deviation of CC and RDMS values are also given in Table 4.3 for 15 µV and 150 µV cases.

L-curve method produces some problematic curves when solution is very smooth as shown in Figure 4.14.a, because y axis is defined by solution norm and increased noise has a large effect on the produced solutions. In Figure 4.14.b, a better shaped L-curve is seen, which is produced at time instant 63 for the 150 µV case. In Figure 4.15, a GCV plot is shown. Here, the rightmost point along the straight curve is selected to give good results.

4.4.3.1. Discussion on results of regularization parameter selection methods for TSVD Method

Among regularization parameter selection methods, all of the regularization parameter selection methods give very similar results when the 15 µV measurement noise is added to the data. The difference between methods is more significant when the noise level is increased to 150 µV. For the 150 µV case, GCV gives better results for most cases and average value of the correlation coefficient is larger when compared to that obtained by the L-curve method. Previously reported problems with the L-curve are also present in the TSVD method when the solutions are very smooth and the noise level is high. For these reasons GCV seems more reasonable parameter selection method for TSVD.

4.4.4. Performances of Regularization Parameter Selection Methods for TTLS Method

In this section, truncation number for the TTLS method is selected by different regularization methods for different noise levels. These methods are L-curve, GCV and max CC method. For

comparison of performances of these methods, 15 µV (30 dB SNR) and 150 µV (10 dB SNR) Gaussian white noise is added to torso data and inverse ECG problem is solved using the TTLS method.
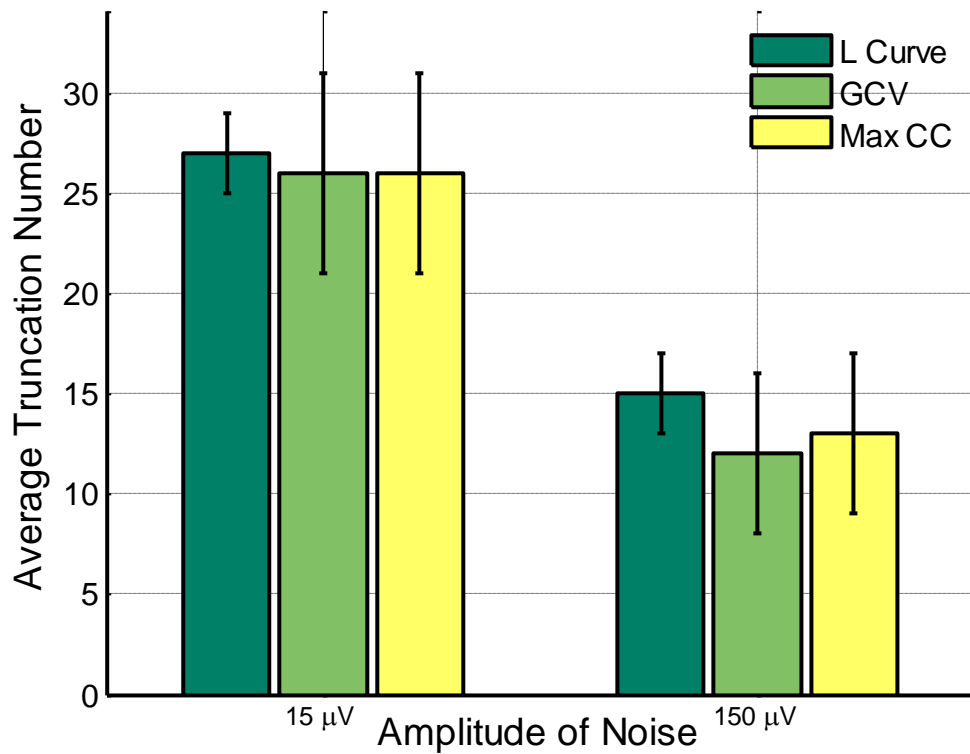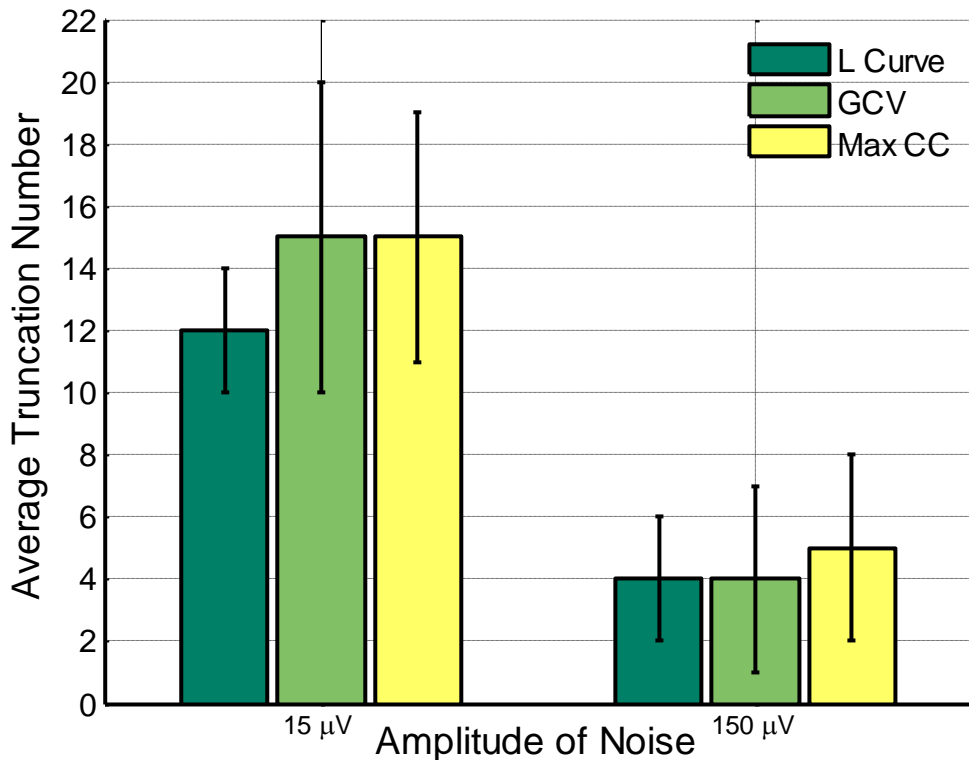

Figure 4.16: Average Truncation Number with respect to Amplitude of noise graph of four regularization parameter selection methods for TTLS Method

In Figure 4.16, average truncation numbers for different noise levels are illustrated. Again, since non-integer truncation number is meaningless, they are rounded to the nearest integer. In this figure, it is seen that for the 15 µV case, average truncation numbers found by the L-curve are much smaller than those found by the GCV method, which is different from the previously presented TSVD, Tikhonov and LSQR cases, because for the first time instants better shaped L-curves are obtained and better parameter values corresponding to the corner can be selected by the triangle algorithm. When noise level is increased to 150 µV, L-curve and GCV obtained smaller average truncation number than the max CC, which means solutions are over smoothed.

In Figure 4.17.a and Figure 4.17.b, the average CC and RDMS graphs are given respectively for the TTLS method when the truncation number is calculated by the L-curve, GCV and max CC methods. From these graphs, it is seen that max CC gives better results than GCV and L-curve as expected and with increasing noise level the performance difference between the max CC method and the others became more significant. GCV and L-curve give poor performances at first 30 ms when average noise amplitude is 150 µV. There are some spikes at some later time instants for the L-curve method; GCV gives more robust results for 15 and 150 µV cases. Average and standard deviation values are also given in Table 4.4. From this table, it can be seen that the truncation numbers used for the TTLS are smaller than the iteration numbers obtained for the LSQR, and the truncation numbers used in the TSVD method.
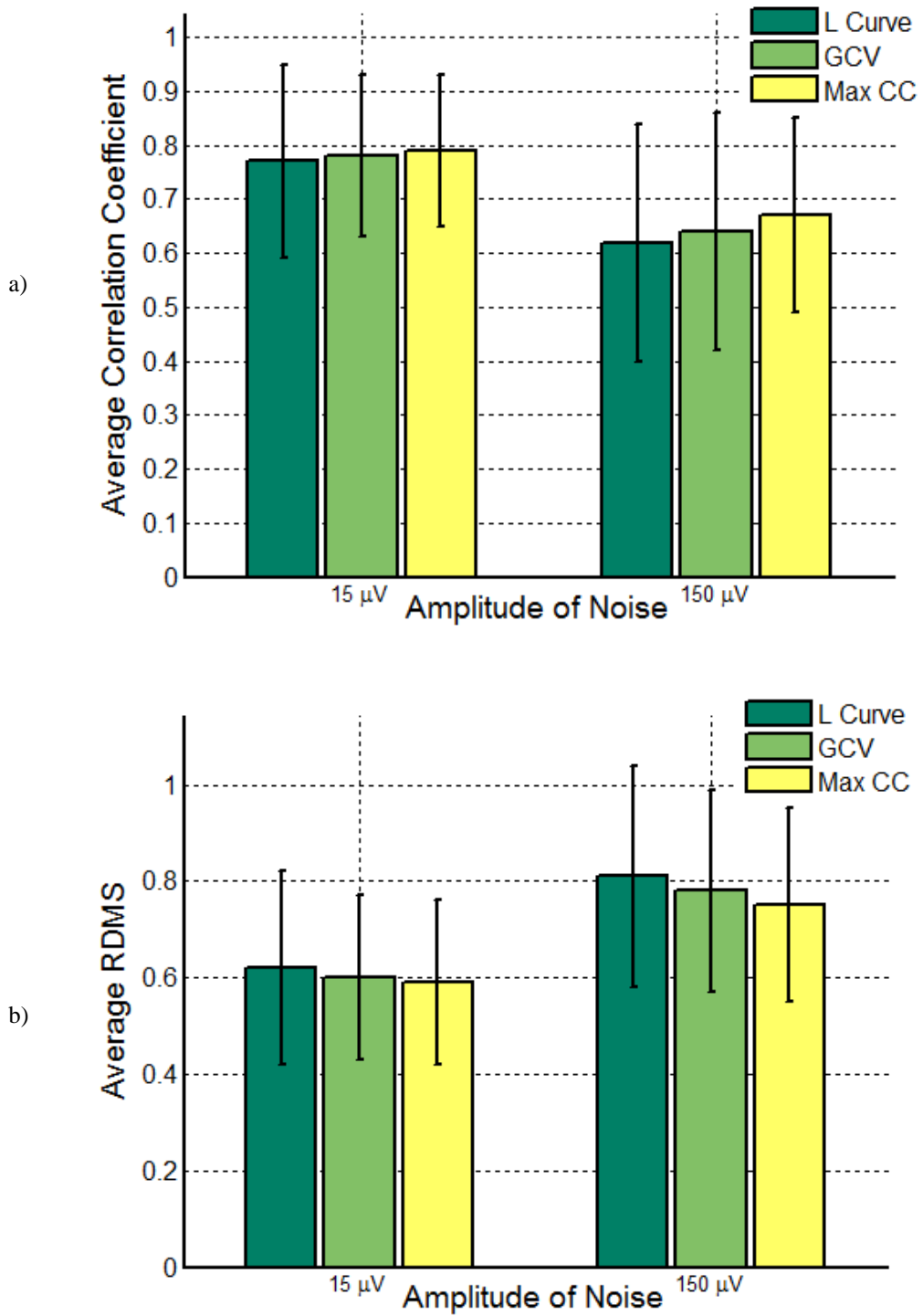
Figure 4.17: a) Average Correlation Coefficient vs Amplitude of noise graph of three regularization parameter selection methods for TTLS Method b) Average RDMS vs Amplitude of noise graph of three regularization parameter selection methods for TTLS Method

Table 4.4: Mean and standard deviation values of truncation, CC and RDMS values of different regularization parameter selection methods at 15 µV measurement noise

	Methods	Avg. Truncation Num.	CC Values	RDMS
15 µV measurement noise	L-curve	12 ± 2	0.71 ± 0.17	0.71 ± 0.20
	GCV	15 ± 5	0.72 ± 0.17	0.68 ± 0.19
	Max CC	15 ± 4	0.73 ± 0.16	0.68 ± 0.19
150 µV measurement noise	L-curve	4 ± 2	0.53 ± 0.20	0.93 ± 0.20
	GCV	4 ± 3	0.54 ± 0.22	0.90 ± 0.21
	Max CC	5 ± 3	0.59 ± 0.16	0.87 ± 0.18

In Figure 4.18, L-curve plot is given for the first time instant when the noise level is 15 µV. From this plot, it is seen that when TTLS method is used better L-curve plots are obtained at first time instants. However there is also a local corner, which may cause incorrect results.
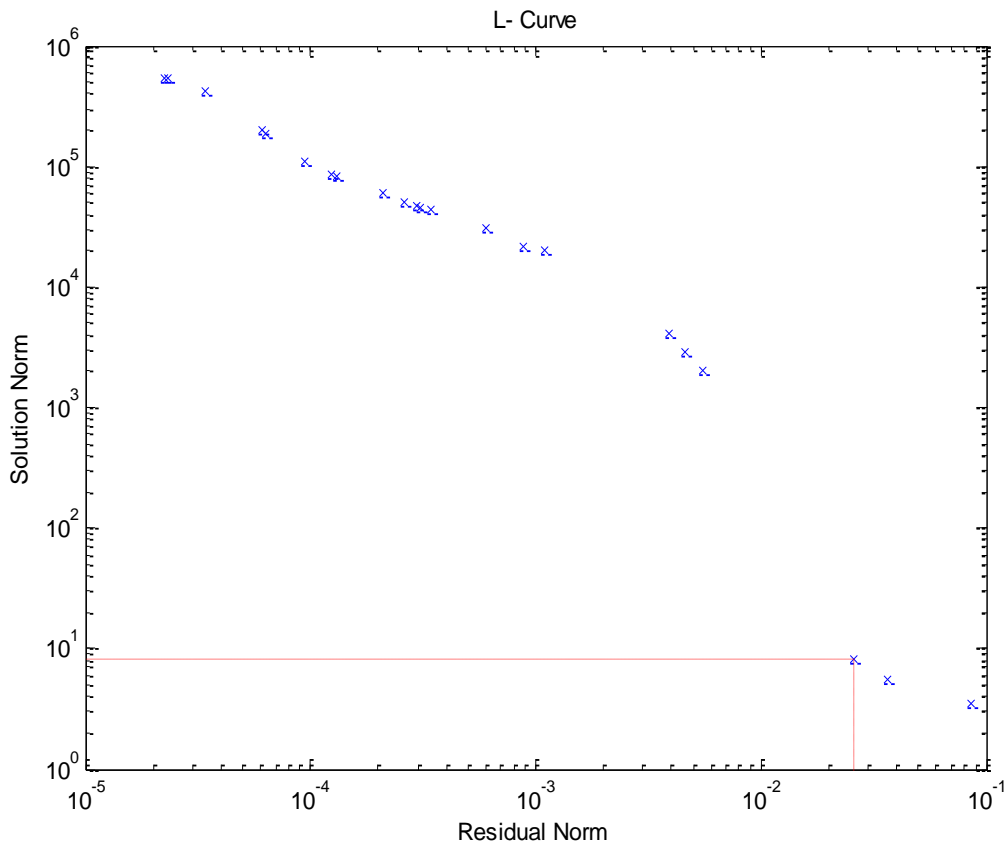
Figure 4.18: L-curve plot at time instant 1 for 15 µV case

4.4.4.1. Discussion on results of regularization parameter selection methods for TTLS Method

According to test results, it is seen that when noise is increased, performance difference between max CC and other methods is also increased as expected. For 15 μV and 150 μV cases, GCV gave slightly better results than L-curve, because of the smooth L-curve characteristics. When average truncation number of TTLS is compared with the parameters of the TSVD and LSQR methods, it is seen that, best solutions are obtained in smaller regularization parameters in TTLS.

4.4.5. Performances of Regularization Parameter Selection Methods for Lanczos TTLS Method

In this section, truncation number for Lanczos TTLS method is selected by different regularization methods for different noise levels. These methods are L-curve, GCV and max CC method. For comparison of performances, 15 μV (30 dB SNR) and 150 μV (10 dB SNR) Gaussian white noise is added to torso data and inverse ECG problem is solved using Lanczos TTLS method.
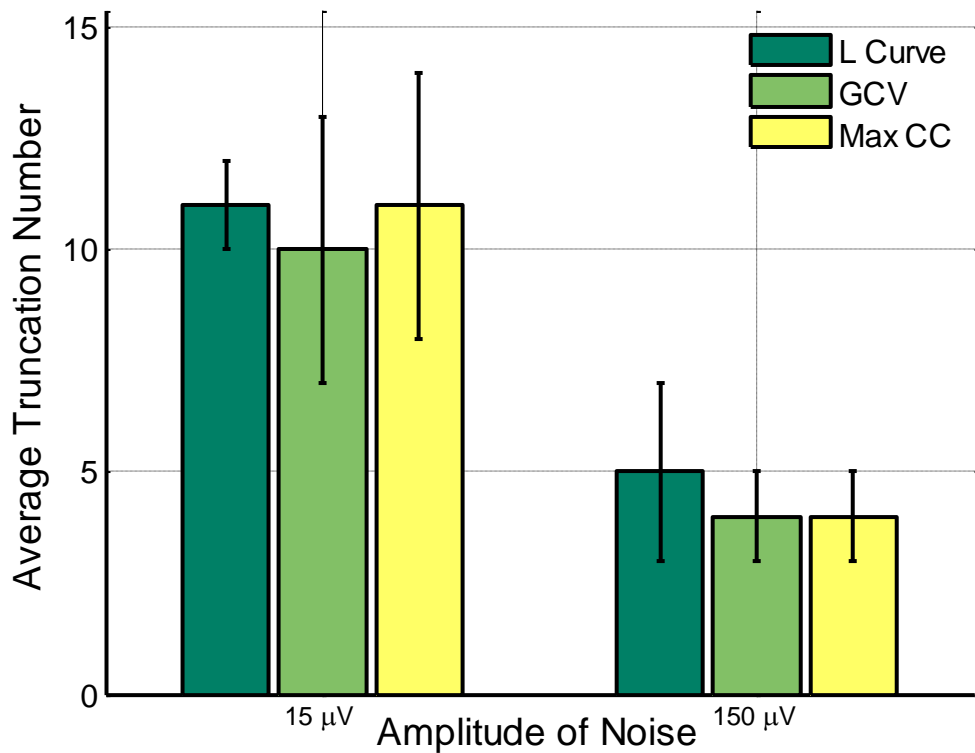
Figure 4.19: Average Truncation Number with respect to Amplitude of noise graph of four regularization parameter selection methods for Lanczos TTLS Method

In Figure 4.19, average truncation numbers for 15 and 150 μV noise levels are illustrated, since non-integer truncation number is meaningless, they are rounded to the nearest integer. In this figure, it is seen that for the 15 μV case average truncation numbers found by L-curve is similar to the max CC method and GCV obtained smaller average truncation numbers. When the noise level is increased to 150 μV, GCV obtained the same average truncation number with the max CC, and the L-curve method has under-smoothing (larger truncation values) effect. Average and standard deviations of truncation numbers is also given in Table 4.5.
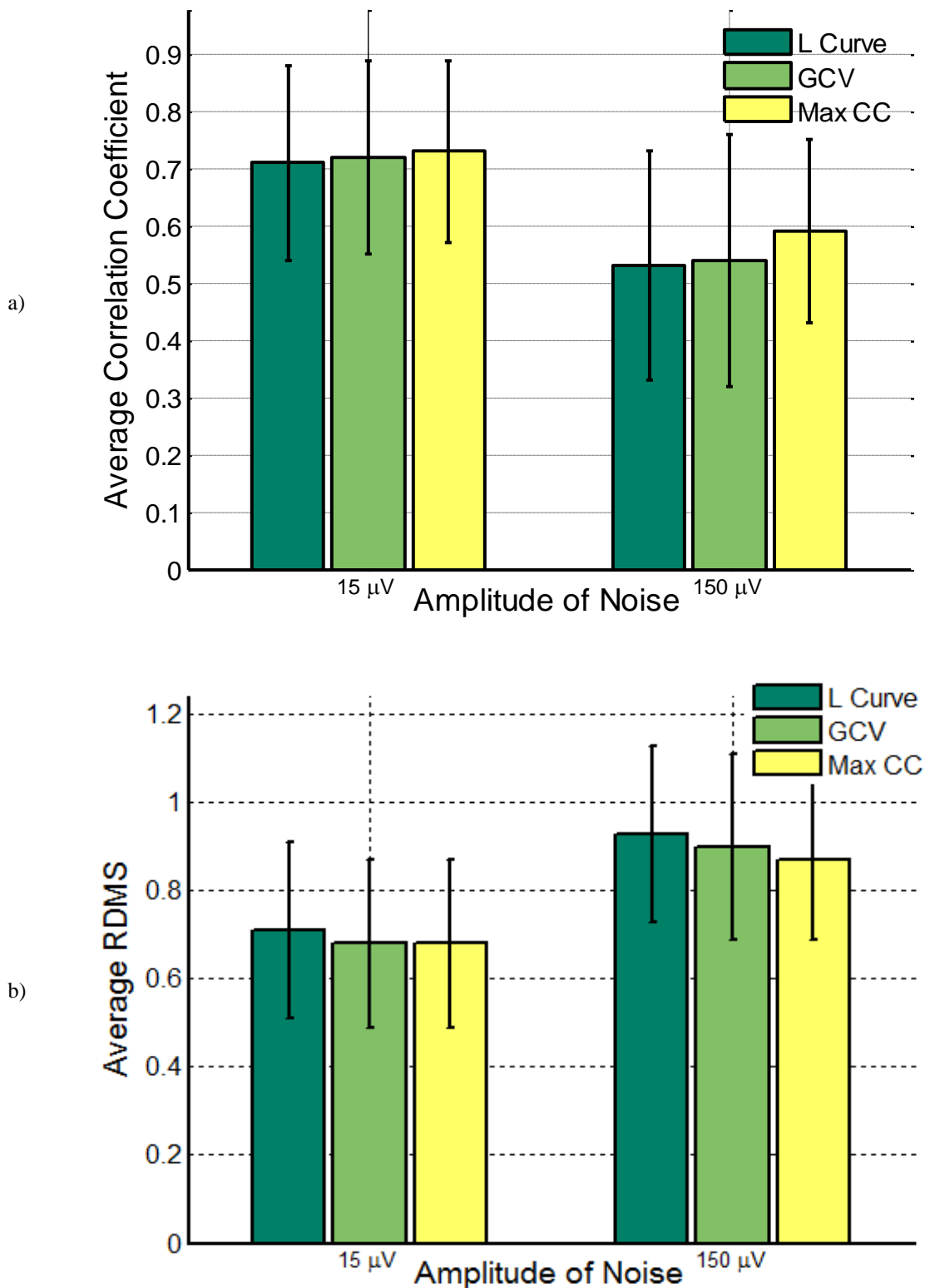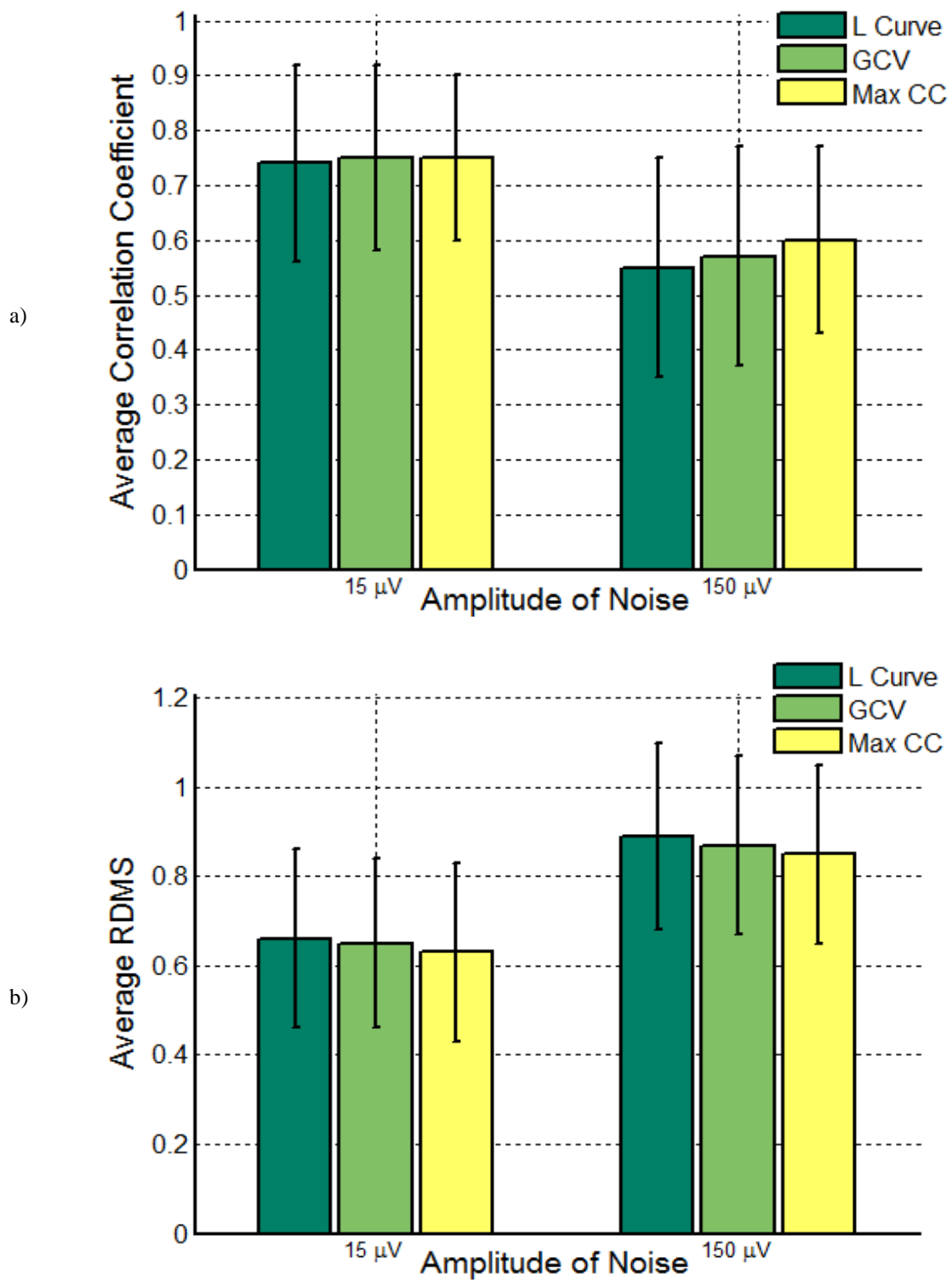
Figure 4.20: a) Average Correlation Coefficient vs Amplitude of noise graph of three regularization parameter selection methods for Lanczos TTLS Method b) Average RDMS vs Amplitude of noise graph of three regularization parameter selection methods for Lanczos TTLS Method

Table 4.5: Mean and standard deviation values of truncation number, CC and RDMS values of different regularization parameter selection methods at 15 and 150 µV measurement noise cases

	Methods	Avg. Truncation Num.	CC Values	RDMS
15 µV measurement noise	L-curve	11 ± 1	0.74 ± 0.18	0.66 ± 0.20
	GCV	10 ± 3	0.75 ± 0.17	0.65 ± 0.19
	Max CC	11 ± 3	0.77 ± 0.15	0.63 ± 0.20
150 µV measurement noise	L-curve	5 ± 2	0.55 ± 0.20	0.89 ± 0.21
	GCV	4 ± 1	0.57 ± 0.20	0.87 ± 0.20
	Max CC	4 ± 1	0.60 ± 0.17	0.85 ± 0.20

In Figure 4.20.a and Figure 4.20.b, the average CC and RDMS graphs are given respectively for the Lanczos TTLS problem when the truncation numbers are calculated by L-curve, GCV and max CC methods. From these graphs, it is seen that max CC gives better results than GCV and L-curve as expected and with increased noise level, the performance difference became more significant. GCV and L-curve give poor performances at the first 30 ms when average noise amplitude is 150 µV. There are some spikes at some later time instants for L-curve method, GCV gave more robust results for 15 and 150 µV cases. Average and standard deviation values are also given in Table 4.5. From this table, it can be seen that Lanczos TTLS showed a similar characteristic with the TTLS method and obtained solutions at smaller truncation numbers than the iteration number of the LSQR method and the truncation number of the TSVD. Upon examining the results, we observed that modified GCV (selecting rightmost minimum value) improved solutions when compared with the GCV method; it increased the average CC values by 10% when 150 µV measurement noise is added to the data.

4.4.5.1. Discussion on results of regularization parameter selection methods for Lanczos TTLS Method

According to test results, it is seen that when noise level is increased, performance difference between max CC and other methods also increased as expected. For 15 µV and 150 µV cases, modified GCV obtained better results than L-curve. Lanczos TTLS is also obtained better solutions for smaller truncation numbers as in the TTLS method. Smaller truncation number means fewer iterations and faster runtime.

4.5. Performances of Regularization Methods with Maximum CC Method

In this section, performances of regularization methods LSQR, Tikhonov, TSVD, TTLS and Lanczos TTLS are compared for different levels of measurement and geometrical errors. In these comparisons, the regularization parameter for Tikhonov regularization method, the iteration number for the LSQR method, and the truncation level of TSVD, TTLS and Lanczos TTLS methods are selected by using the maximum CC method, so maximum correlation coefficient values are achieved for each method. The ranges of these parameters that we use to seek for the one yielding maximum correlation coefficient value are defined according to observations during tests for Tikhonov, TSVD, LSQR and Lanczos TTLS methods and maximum truncation value of TTLS is defined by the algorithm, these ranges are given in Table 4.6 for each of the implemented methods.

Table 4.6: Parameter values of regularization methods

Methods	Regularization Parameter	Range
LSQR	k, iteration number	$k= 1,2,…,30$
Tikhonov	λ, regularization parameter	10^{-10} to 1 (100 logarithmically spaced points)
TSVD	k, truncation number	$k= 1,2,…,40$
Lanczos TTLS	k, truncation number	$k= 1,2,…,20$
TTLS	k, truncation number	$1\leq k \leq \min (n, \text{rank} (\mathbf{A},\mathbf{Y}))$

For comparison of the regularization methods, five different simulation noise scenarios are considered:

1. 15 µV Gaussian white measurement noise is added to body surface potentials simulated from real epicardial potentials. Signal to noise ratio corresponding to this amount of noise is equal to 30 dB.

2. 150 µV Gaussian white measurement noise is added to torso potentials simulated from epicardial potentials. Signal to noise ratio corresponding to this amount of noise is equal to 10 dB, which represents a larger amount of noise than the 15 µV case,

3. First type of geometric error is introduced into the model by assuming that the size of the heart geometry used in the forward matrix calculation is different from that used to simulate the body surface potential measurements. To simulate this noise, the coordinates of the heart geometry are multiplied by a scaling factor and an erroneous transfer matrix is obtained. Then, this transfer matrix is used for inverse solution. 15 µV measurement error is also added to torso potentials. To simulate this geometrical error, we used an extreme case, where the heart size very large when compared with the normal size and 1.4 is used as scaling factor.

4. A second type of geometric error is introduced into the model by assuming that the location of the heart is incorrectly estimated. To simulate this noise, the heart geometry can be shifted in x, y or z direction by different amounts. Here, as an example the heart geometry is shifted by 10 mm in the positive x-direction and an erroneous transfer matrix is obtained. Then, similar to the scale error case, this erroneous transfer matrix is used for inverse solution. Again, 15 µV measurement error is also added to torso potentials.

5. Both types of geometric errors, i.e., incorrect size of the heart geometry and shift in the heart axis, are combined. To combine the geometric errors used before, the heart is shifted by 10 mm in the positive x direction and the heart geometry coordinates are multiplied by a scaling factor of 1.4. The transfer matrix obtained using this erroneous geometry is then included in the inverse problem solutions. Similar to previous two cases, 15 µV measurement error is also added to torso potentials.
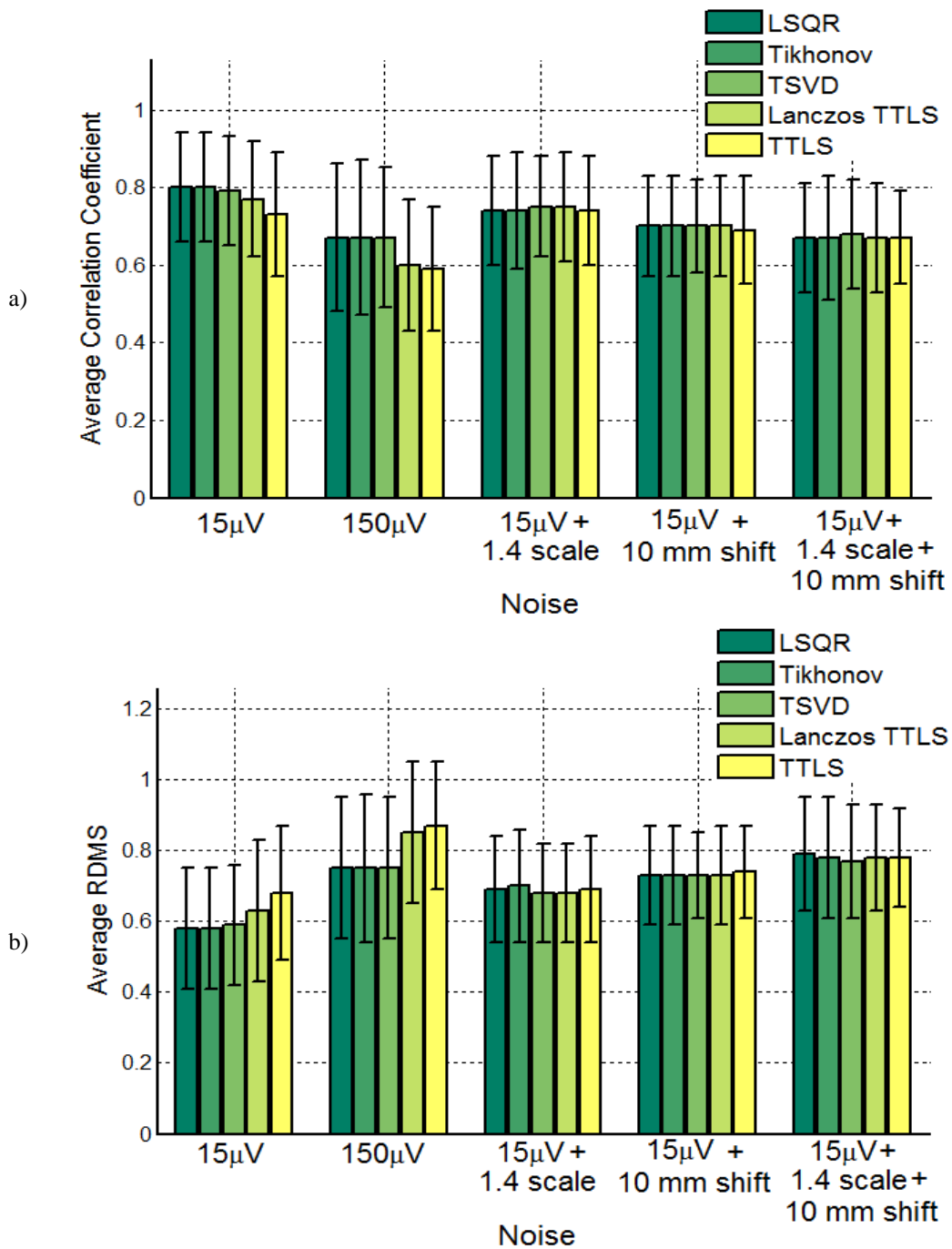
Figure 4.21: a) Average and standard deviations of CC values of five regularization methods for five different noise cases b) Average and standard deviations of RDMS values of five regularization methods for five different noise cases

In Figure 4.21.a, and Figure 4.21.b, averages and standard deviations of CC values and RDMS values obtained from the reconstructions corresponding to five regularization methods; LSQR, Tikhonov, TSVD, Lanczos TTLS and TTLS are shown, respectively. The y-axis of these plots (i.e. each group of bar charts) corresponds to five different simulation noise scenarios. In order to obtain these plots, first the CC and the RDMS values are calculated at each of 97 time instants within the QRS region. Then, the average and the standard deviation of these parameters are found. The bars in the plots correspond to the average values, and the error bars show the standard deviation values. As explained in Section 4.1, epicardial potentials have low amplitudes and the depolarized region is restricted to a small area on the epicardium, the measurement noise is much larger in the earlier

57

times than mid-QRS interval, compared to signal contents. Thus, the measurement noise is dominant compared to heart signals and corresponding SNR values for these time instants are smaller compared to mid-QRS interval. When time passes, the amplitudes of epicardial potentials increase and the effect of noise decreases. After 60 ms, amplitudes of the potentials start to decrease and noise becomes dominant again. For these reasons CC values between 30 ms and 60 ms are larger than other time instants for all methods.

The average and standard deviation values of CC and RDMS are also given in Table 4.7. Our observations on these results can be summarized as follows:

- 15 µV Gaussian white measurement noise case: For this case, it can be seen that LSQR, Tikhonov and TSVD give very similar results, Lanczos TTLS is a little worse (by 3%) when compared to the other three methods and TTLS gives the poorest performance (by 7%) among these methods. When performances at different time instants during the QRS cycle are considered, we observed that during the first 10 ms period after stimulation, all methods have poor performances, because epicardial voltage level is very low and effect of noise is dominant, but stimulation point is still visible as it can be seen in Figure 4.22. After 10 ms, RDMS values decrease and CC values increase for all methods as expected because epicardial potential levels increase. For the 15 µV Gaussian white measurement noise case, LSQR, Tikhonov and TSVD give very similar results and Lanczos TTLS also gives similar performance during 40 ms − 70 ms period, TTLS gives the worst performance among these methods at all time instant, its CC values are worse than others by 5% during 40 ms − 70 ms period and this difference increases up to 10% at other times.

- 150 µV Gaussian white measurement noise case: It is observed that LSQR, Tikhonov and TSVD give very similar results. The TTLS and Lanczos TTLS give poorer performances compared to the other methods (by approximately 7% decrease in CC values). When compared to the previous case of 15 µV − noise, there is approximately 13% decrease in the CC values of Tikhonov, LSQR and TSVD, but Lanczos TTLS has 17% decrease and TTLS has 14% decrease, which means TTLS based algorithms are less tolerant to measurement noise, because TTLS uses singular values of $(\mathbf{A},\mathbf{Y})$. Therefore, errors in the torso potentials have more effect on the solution. During the first 20 ms after stimulation, all methods have the same poor performances. After that time instant CC values increase and RDMS values decrease for all methods, but TTLS and Lanczos TTLS give worse performances when compared with the other methods.

- 1.4 scaling geometric error case with 15 µV Gaussian white measurement noise: It is seen that all methods give very similar results. Different from the measurement error cases, TTLS and Lanczos TTLS also showed similar performances to the other methods, because TSVD, LSQR and Tikhonov are not good methods for dealing with geometrical errors. When the results are examined in detail, we observed that all methods have similar results during the QRS cycle, especially between 30 and 70 ms.

- 10 mm shift geometric error case with 15 µV Gaussian white measurement noise: It is seen that all methods have similar average CC values, similar to the 1.4 scaling geometric error case. Again, this is consistent with observations reported in literature that TTLS based methods are less affected by geometrical errors. Detailed examination of the results during the QRS cycle shows that all methods have very similar performances.

- 1.4 scaling and 10 mm shift geometric error case with 15 µV Gaussian white measurement noise: It is seen that all methods give very similar results, but TTLS and TSVD are slightly better. During the QRS cycle, there are small performance differences at different time instants, but in average all methods obtained similar results.

Table 4.7: Averages and standard deviations of CC and RDMS values over time corresponding to five different simulation noise scenarios.

	Methods	CC Values	RDMS
15 µV measurement noise	LSQR	0.80 ± 0.14	0.58 ± 0.17
	Tikhonov	0.80 ± 0.14	0.58 ± 0.17
	TSVD	0.79 ± 0.14	0.59 ± 0.17
	Lanczos TTLS	0.77 ± 0.15	0.63 ± 0.20
	TTLS	0.73 ± 0.16	0.68 ± 0.19
150 µV measurement noise	LSQR	0.67 ± 0.19	0.75 ± 0.20
	Tikhonov	0.67 ± 0.20	0.75 ± 0.21
	TSVD	0.67 ± 0.18	0.75 ± 0.20
	Lanczos TTLS	0.60 ± 0.17	0.85 ± 0.20
	TTLS	0.59 ± 0.16	0.87 ± 0.18
15 µV meas. noise + 1.4 scaling Factor	LSQR	0.74 ± 0.14	0.69 ± 0.15
	Tikhonov	0.74 ± 0.15	0.70 ± 0.16
	TSVD	0.75 ± 0.13	0.68 ± 0.14
	Lanczos TTLS	0.75 ± 0.14	0.68 ± 0.14
	TTLS	0.73 ± 0.14	0.69 ± 0.15
15 µV meas. noise + 10 mm shift	LSQR	0.70 ± 0.13	0.73 ± 0.14
	Tikhonov	0.70 ± 0.13	0.73 ± 0.15
	TSVD	0.70 ± 0.13	0.73 ± 0.13
	Lanczos TTLS	0.70 ± 0.12	0.73 ± 0.15
	TTLS	0.69 ± 0.14	0.74 ± 0.15
15 µV meas. noise + 1.4 scaling Factor + 10 mm shift	LSQR	0.67 ± 0.14	0.79 ± 0.16
	Tikhonov	0.67 ± 0.16	0.78 ± 0.17
	TSVD	0.68 ± 0.14	0.77 ± 0.16
	Lanczos TTLS	0.67 ± 0.14	0.78 ± 0.15
	TTLS	0.67 ± 0.12	0.78 ± 0.14

Here, the performances of regularization methods will be visually evaluated. For this purpose, the quality and shape of the waveform will be evaluated by using the figures obtained with MAP3D.

Figure 4.22 and Figure 4.23 show the Map3d images of real and reconstructed epicardial potentials for the "15 µV – measurement noise" case at 6 ms and 50 ms after stimulation, respectively. The initial stimulation site (i.e., the ectopic focus) can be seen in the real epicardial potentials at 6 ms. LSQR, Tikhonov and TSVD methods detected the ventricular ectopic focus, but wavefront is smoother than the original. At this time instant, Lanczos TTLS and TTLS also detected the ectopic focus, but there are also some artifacts (regions that also appear to be stimulation sites). At 50 ms, the activation wavefront has propagated through most of the epicardial surface. All methods constructed similar epicardial potential maps and detected the depolarized regions and the general pattern of the wavefront correctly but the reconstructed wavefronts are smoother than the original, especially for TTLS and Lanczos TTLS solutions. It is also observed that after 34 ms, all methods produce similar wavefronts.
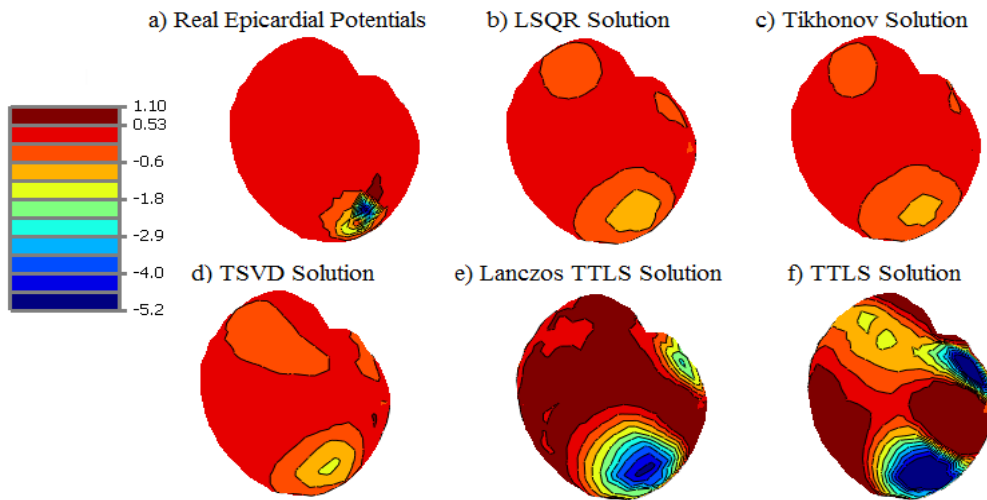
Figure 4.22: Epicardial Potential Maps of reconstructed solutions for 15 µV noisy data: a) Real Potential Distribution at the 6 ms b) LSQR Solution c) Tikhonov Solution d) TSVD Solution e) Lanczos TTLS Solution f) TTLS Solution

Figure 4.23: Epicardial Potential Maps of reconstructed solutions for 15 µV noisy data: a) Real Potential Distribution at the 50 ms b) LSQR Solution c) Tikhonov Solution d) TSVD Solution e) Lanczos TTLS Solution f) TTLS Solution

Figure 4.24 and Figure 4.25 show the Map3d images of real and reconstructed epicardial potentials for "150 µV – measurement noise" case at 40 ms and 50 ms after stimulation, respectively. For this case, stimulation site cannot be observed during the earlier time instants; therefore we look at later time instants. Figure 4.24 shows that LSQR, Tikhonov and TSVD find the depolarized region; however, LSQR and Tikhonov regularization reconstruct smoother waveforms. At this time instant, Lanczos TTLS and TTLS are unable to detect the region correctly. The general form of the solution looks similar with TTLS and Lanczos TTLS; the depolarized and resting regions and the wavefront have a similar spatial pattern, but the amplitudes of epicardial potentials are approximately 7, and 6 times higher by TTLS Lanczos TTLS, respectively, than the true potentials. This means that the effect of high noise cannot be suppressed. This amplification is observed during the first 45 and the last 10 ms, where the effective signal to noise ratio is much smaller than the overall signal to noise ratio. At 50 ms, excitation wavefront has propagated through most of the epicardial surface. All methods have produced similar smooth wavefronts, when compared with the previous 15 µV case.
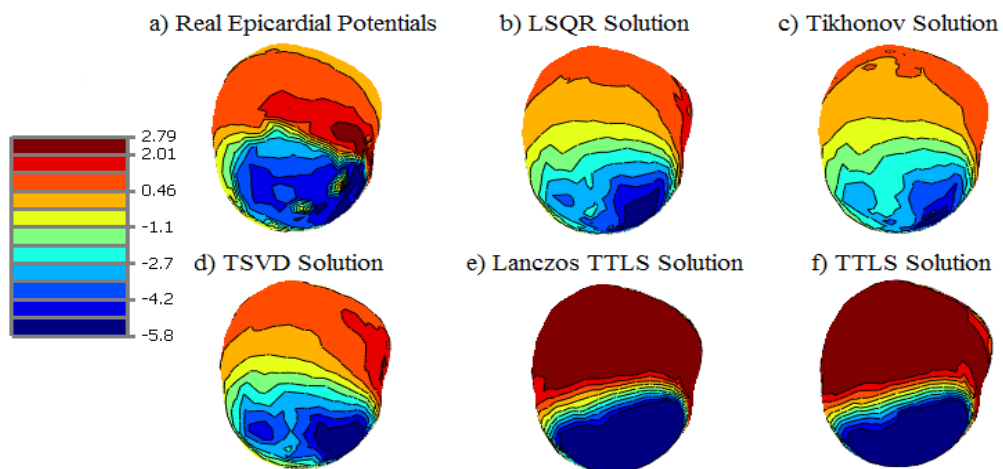
Figure 4.24: Epicardial Potential Maps of reconstructed solutions for 150 µV noisy data: a) Real Potential Distribution at the 40 ms b) LSQR Solution c) Tikhonov Solution d) TSVD Solution e) Lanczos TTLS Solution f) TTLS Solution

Figure 4.25: Epicardial Potential Maps of reconstructed solutions for 150 µV noisy data: a) Real Potential Distribution at the 50 ms b) LSQR Solution c) Tikhonov Solution d) TSVD Solution e) Lanczos TTLS Solution f) TTLS Solution

Figure 4.26, Figure 4.27and Figure 4.28 show the Map3d images of real and reconstructed epicardial potentials for the "15 µV – measurement noise and 1.4 scaling geometric error" case at 4 ms, 18 ms and 50 ms after stimulation, respectively. In Figure 4.26, initial activation point is seen on the epicardial surface. At this time instant, TTLS and Lanczos TTLS have detected the initial stimulation site, although it is smoothed. LSQR, TSVD and Tikhonov are unable to detect the initial activation at this early time instant. Between 12 and 25 ms, TTLS and Lanczos TTLS reconstruct wavefronts better than the other methods. In Figure 4.27, we observe that the wavefront has started to propagate over the epicardial surface. At this time instant, TTLS and Lanczos TTLS have better fidelity to the true potentials than other methods. After 25 ms, all methods start to give similar results as illustrated in Figure 4.28, but when compared with 15 µV measurement error case, the waveform is smoother but it is better than 15 µV measurement noise case.

Figure 4.26: Epicardial Potential Maps of reconstructed solutions for 15 µV measurement noise added data with 1.4 scaling geometric error: a) Real Potential Distribution at the 4 ms b) LSQR Solution c) Tikhonov Solution d) TSVD Solution e) Lanczos TTLS Solution f) TTLS Solution
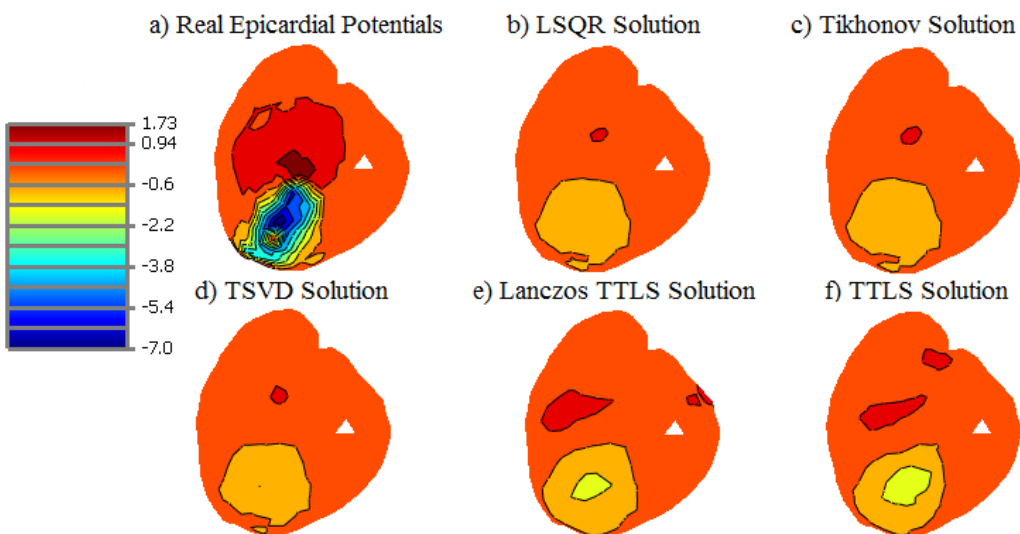
Figure 4.27: Epicardial Potential Maps of reconstructed solutions for 15 µV measurement noise added data with 1.4 scaling geometric error: a) Real Potential Distribution at the 18 ms b) LSQR Solution c) Tikhonov Solution d) TSVD Solution e) Lanczos TTLS Solution f) TTLS Solution
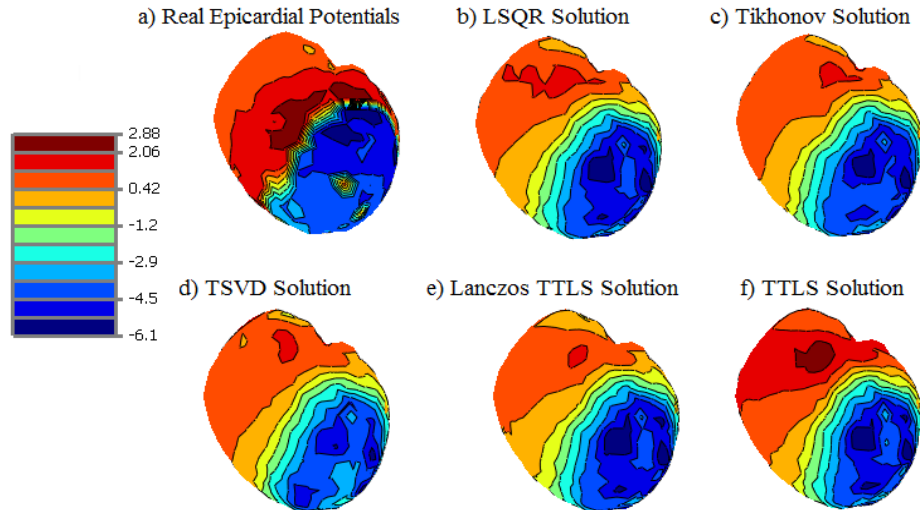
Figure 4.28: Epicardial Potential Maps of reconstructed solutions for 15 µV measurement noise added data with 1.4 scaling geometric error: a) Real Potential Distribution at the 50 ms b) LSQR Solution c) Tikhonov Solution d) TSVD Solution e) Lanczos TTLS Solution f) TTLS Solution

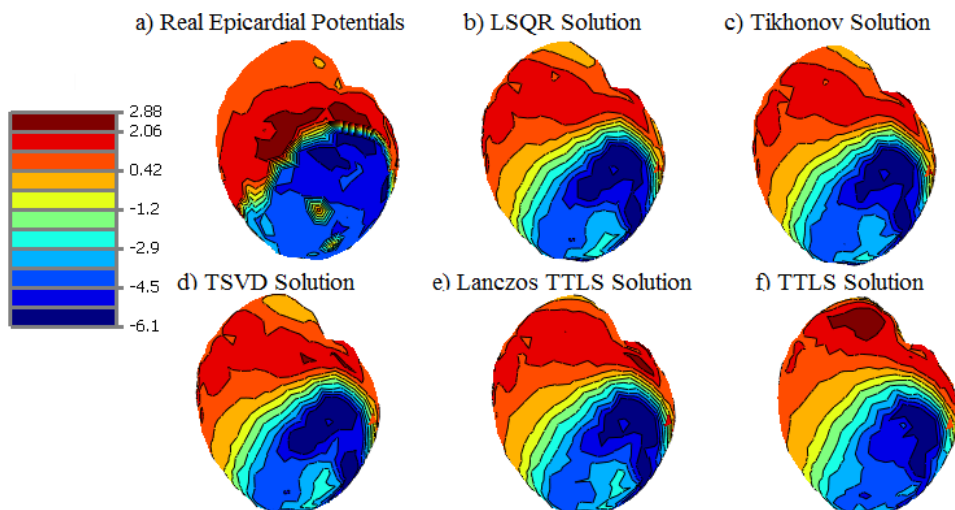Figure 4.29 and Figure 4.30 show the Map3d images of real and reconstructed epicardial potentials for the "15 µV – measurement noise and 10 mm shift geometric error" case at 6 ms and 50 ms after excitation respectively. At 6 ms, the initial activation site can be observed in the real epicardial potential distribution. LSQR, Tikhonov, TSVD and Lanczos TTLS methods detect the ventricular ectopic focus at this time instant, but wavefront is smoother than the original and the "15 µV – measurement noise" case. TTLS also detected the ectopic focus, but there are also some artifacts (regions that also appear to be stimulation sites). In Figure 4.30, it is seen that wavefront propagated through most of the ventricular region and there is only a small inactivated part. All of the methods detected the activated and the resting regions, but wavefronts are smoother compared to real epicardial distributions. For this time instant, the wavefronts are reconstructed better than the 150 µV measurement noise case and similar with 15 µV – measurement noise and 1.4 scaling geometric error case. It is also seen that, there is not much difference with 15 µV measurement noise case for this time instant.
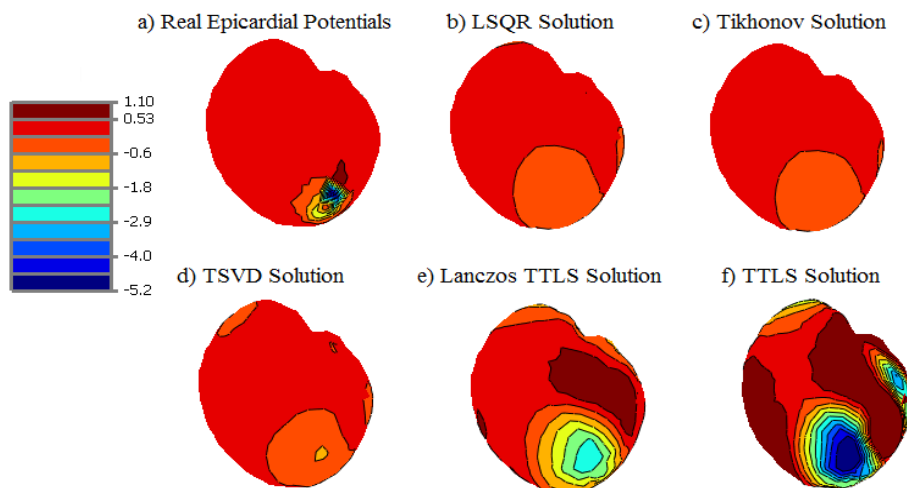
Figure 4.29: Epicardial Potential Maps of reconstructed solutions for 15 µV measurement noise added data with 10 mm shift geometric error: a) Real Potential Distribution at the 6th ms b) LSQR Solution c) Tikhonov Solution d) TSVD Solution e) Lanczos TTLS Solution f) TTLS Solution
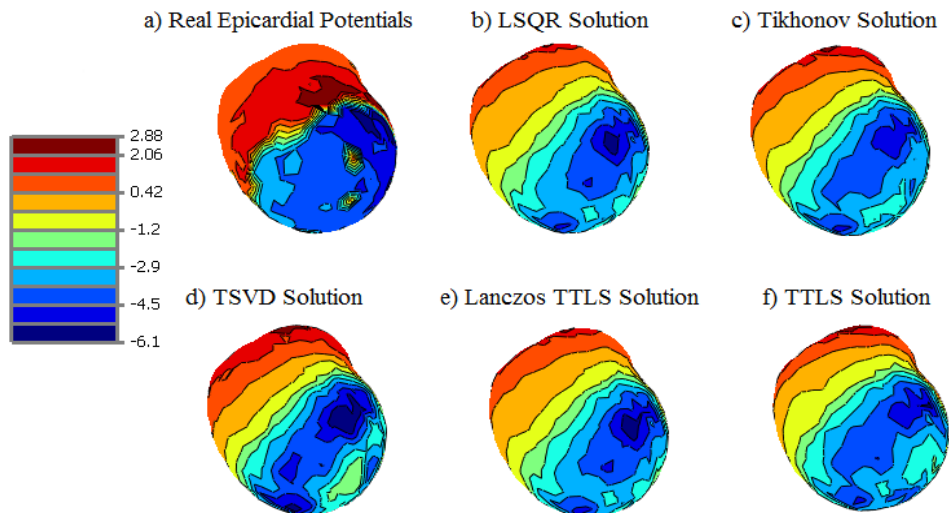
Figure 4.30: Epicardial Potential Maps of reconstructed solutions for 15 µV measurement noise added data with 10 mm shift geometric error: a) Real Potential Distribution at the 50 ms b) LSQR Solution c) Tikhonov Solution d) TSVD Solution e) Lanczos TTLS Solution f) TTLS Solution

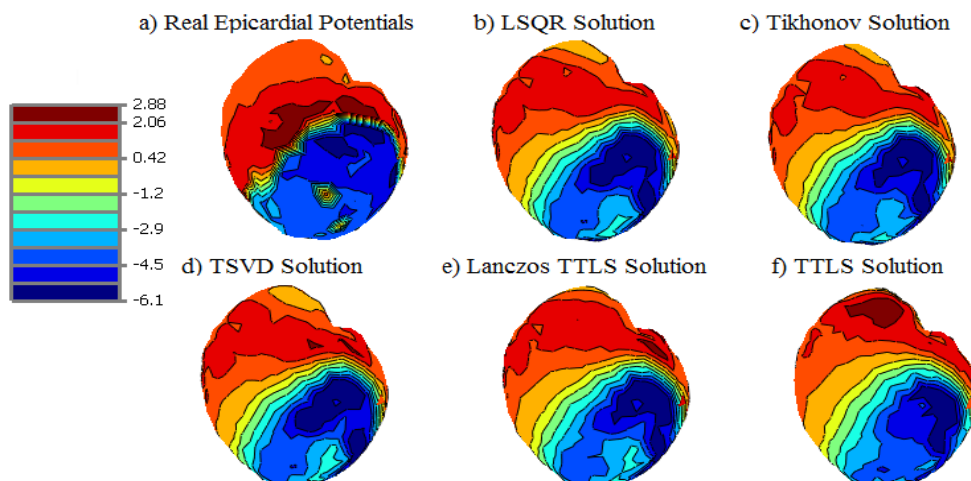Figure 4.31 and Figure 4.32 show the Map3d images of real and reconstructed epicardial potentials for the "15 µV – measurement noise, 1.4 scaling and 10 mm shift geometric error" case at 6 ms and 50 ms after excitation, respectively. In Figure 4.31, initial activation is seen on the epicardial surface. At this time instant, all methods detect the initial activation, but Lanczos TTLS and TTLS obtained better results than others. When compared with the 15 µV measurement error and 15 µV measurement noise with 10 mm shift geometric error cases, we do not observe artifacts such as sites appearing as false stimulation sites with TTLS and Lanczos TTLS solutions for this error case and these waveforms look better however they are very smooth and CC values of five regularization methods for this time instant is smaller than other two noise cases. This means larger CC does not mean better waveforms at very rare situations. When Figure 4.32 is also inspected, we observe that activation has propagated through most of the epicardial surface. At this time instant, all methods produce similar waveforms. These waveforms are very smooth when compared with the real epicardial potentials and they are also smoother than the measurement error and geometrical error cases.
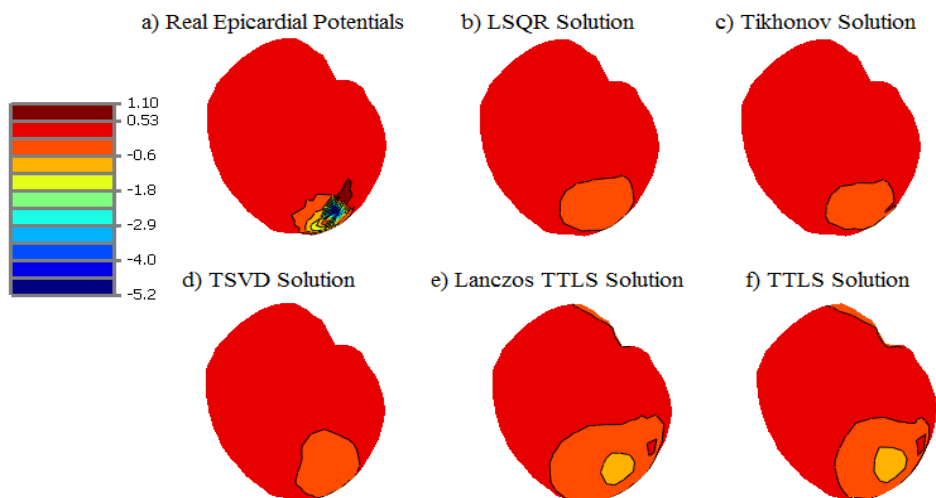
Figure 4.31: Epicardial Potential Maps of reconstructed solutions for 15 µV measurement noise added data with 1.4 scaling and 10 mm shift geometric error: a) Real Potential Distribution at 6 ms b) LSQR Solution c) Tikhonov Solution d) TSVD Solution e) Lanczos TTLS Solution f) TTLS Solution
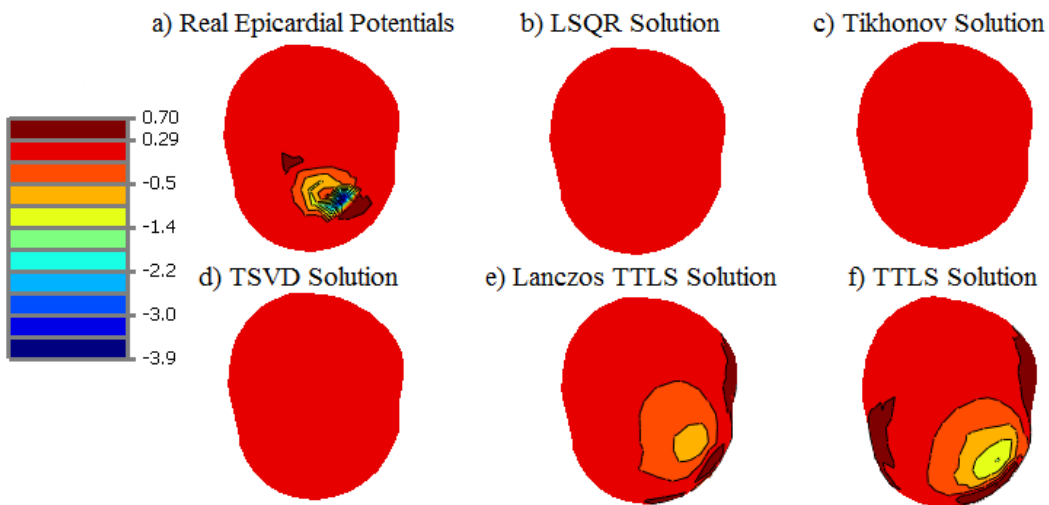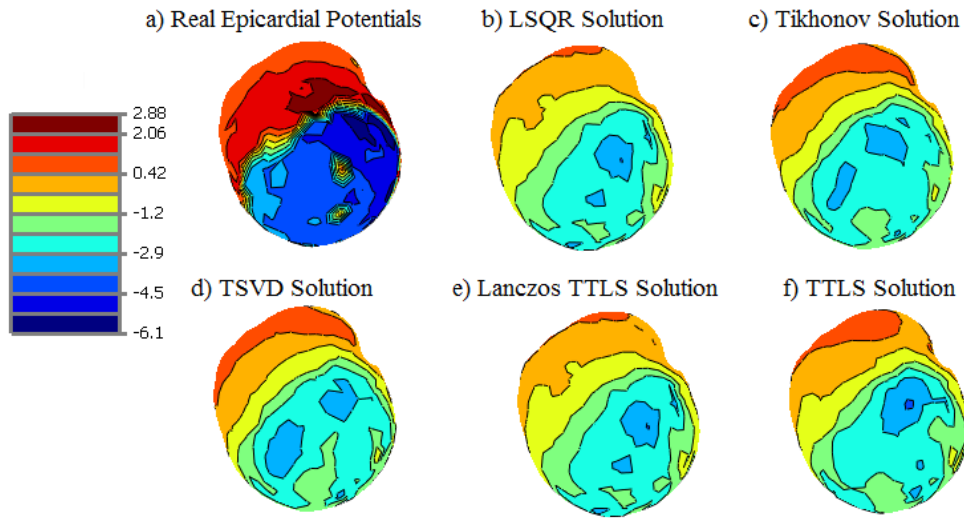
Figure 4.32: Epicardial Potential Maps of reconstructed solutions for 15 μV measurement noise added data with 1.4 scaling and 10 mm shift geometric error: a) Real Potential Distribution at 50 ms b) LSQR Solution c) Tikhonov Solution d) TSVD Solution e) Lanczos TTLS Solution f) TTLS Solution

4.6. Performances of Regularization Methods by using Results of Regularization Parameter Selection Methods

This section is organized as in the previous section; performances of regularization methods: LSQR, Tikhonov, TSVD, TTLS and Lanczos TTLS are compared for different levels of measurement and geometrical errors. The difference between this section and the previous one is that here the regularization parameters for each inverse solver are selected by using the most appropriate regularization parameter selection method, i.e., the modified GCV method, as proposed in Section 4.4. For obtaining the GCV curve, the same ranges of parameters given in Table 4.6 are used.

For comparison of five regularization methods, five different noise simulation cases are inspected; two different levels of measurement noise and three different types of geometrical errors are added to the system. These are the same noise levels used while testing performances of the regularization methods by using max CC method:

- 15 μV Gaussian white measurement noise,
- 150 μV Gaussian white measurement noise,
- 1.4 scaling geometric error case with 15 μV Gaussian white measurement noise,
- 10 mm shift geometric error case with 15 μV Gaussian white measurement noise,
- 1.4 scaling and 10 mm shift geometric error case with 15 μV Gaussian white measurement noise.

In Figure 4.33.a, and Figure 4.33.b, averages and standard deviations of CC and RDMS values obtained from the reconstructions corresponding to five regularization methods; LSQR, Tikhonov, TSVD, Lanczos TTLS and TTLS are shown, respectively. These values are calculated as explained in Section 4.5. The average and standard deviation values of CC and RDMS are also given atTable 4.8. Our observations on these results can be summarized as follows:

- 15 μV Gaussian white measurement noise: For this case, it can be seen that LSQR gives best performance among the five regularization methods. Tikhonov and TSVD give very similar results, Lanczos TTLS is a little worse when compared with the other three methods and TTLS gives the poorest performance among these methods. When performances during the whole QRS cycle are considered, at the start of the QRS cycle Lanczos TTLS gives the poorest performance, but after 25 ms, it obtains similar results with Tikhonov, TSVD and LSQR, especially between 40 and 60 ms. TTLS gives the worst performance among these methods after 15 ms. For this noise level, selecting the iteration number of LSQR by the

GCV method did not cause any difference from the max CC case in terms of average CC and average RDMS values, but for other methods, 2% decrease occurred in the average CC and average RDMS results.

- 150 µV Gaussian white measurement noise: LSQR gives the best performance among all methods at all time instants during the QRS cycle. Similar to most cases, Tikhonov and TSVD give very similar results and they are slightly worse than LSQR by only 1% for this case. The TTLS and Lanczos TTLS give poorer performances when compared with the other methods and they also give worst results among all test conditions. According to the results, similar to the max CC case, TTLS and Lanczos TTLS are more affected by increased measurement error. The average CC values of TTLS and Lanczos TTLS dropped by 18% with respect to the "15 µV – measurement noise" case and the average CC values of LSQR decreased by 15%. For the remaining methods (Tikhonov and TSVD), this drop is 14%. For this noise level, selecting the iteration number of TTLS by the GCV method caused the biggest drop in the average CC values (by 5%) when compared with the max CC case, but for other methods, 2% or 3% decrease occurred in the results.

- 1.4 scaling geometric error case with 15 µV Gaussian white measurement noise: It is seen that LSQR, TSVD and Lanczos TTLS are a slightly better than Tikhonov and TTLS in terms of the average CC and RDMS values. TTLS gives worst performance according to the average RDMS values by 75%. Different from "only measurement error" cases, TTLS and Lanczos TTLS also show the similar performance with the other methods, because TSVD, LSQR and Tikhonov are affected more from geometrical errors. All methods have similar results during the entire QRS cycle. When compared with the max CC case, there is approximately 4% decrease in the average CC values and 4% increase in the RDMS values.

- 10 mm shift geometric error case with 15 µV Gaussian white measurement noise: It is seen that, LSQR, Tikhonov and TSVD methods are obtained best results for the 10 mm shift case, they are still better than Lanczos TTLS by 1% and TTLS by 2%. However, performance difference is decreased between TTLS and Lanczos TTLS methods and others when compared with "only measurement error" cases. This is consistent with observations that TTLS based methods are affected less by geometrical errors. When compared with the max CC case, there is 3% decrease in the average CC values for Tikhonov, TSVD and LSQR and 4% decrease for TTLS and Lanczos TTLS, because TTLS based methods have smaller regularization parameters when compared with the others and small changes in the truncation number causes more differences in the results.

- 1.4 scaling and 10 mm shift geometric error case with 15 µV Gaussian white measurement noise: It is seen that all methods give very similar results, but Tikhonov is slightly worse than the other methods for this case. During the QRS cycle, TTLS is the best method during the first 40 ms but it is worse than the others between 60 ms and 90 ms. Tikhonov is the worst method during the first 40 ms. When compared with the max CC case, there are 2% or 3% decreases in the average CC values.
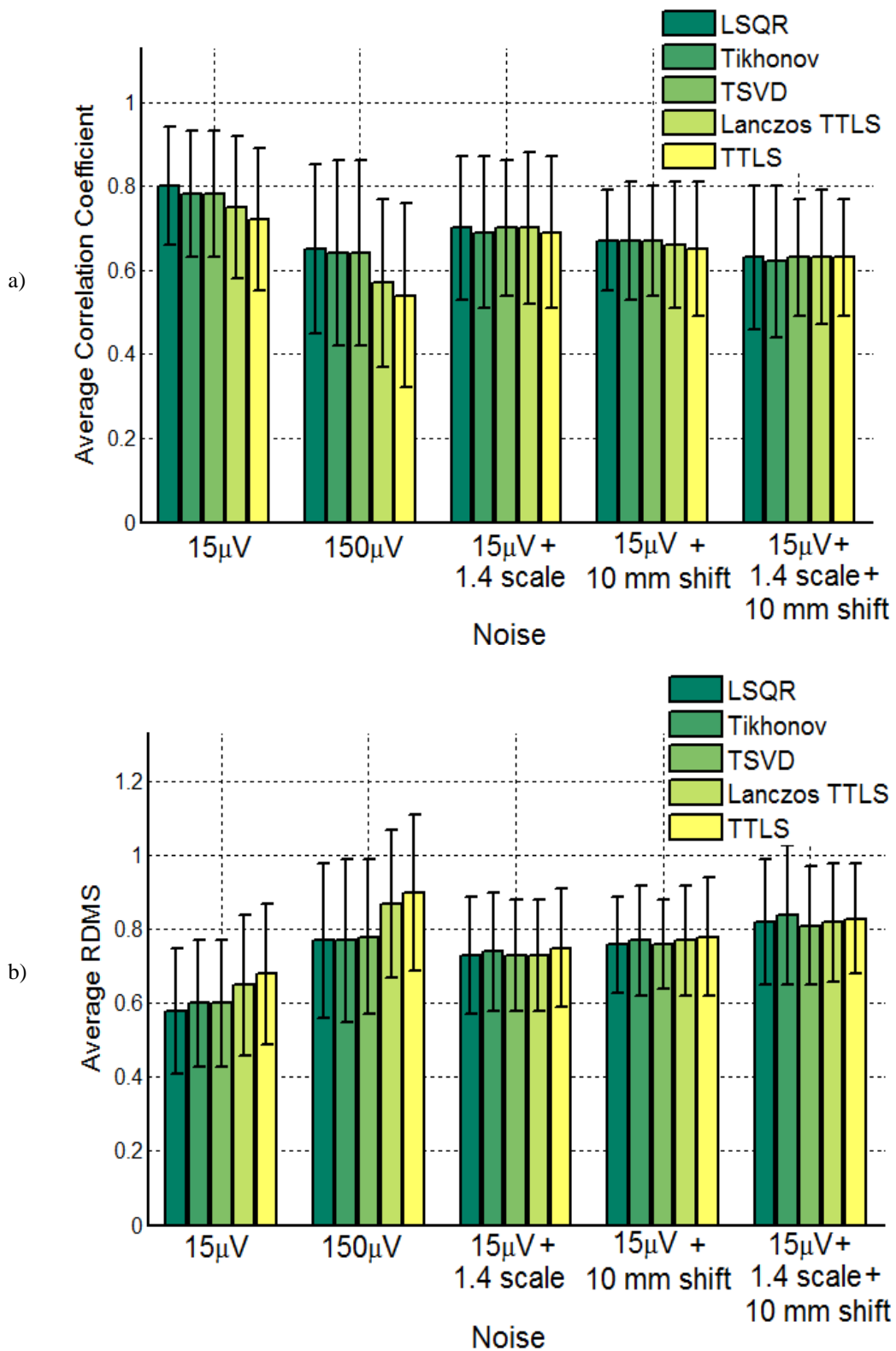
Figure 4.33: a) Average and standard deviations of CC values of five regularization methods for five different noise cases b) Average and standard deviations of RDMS values of five regularization methods for five different noise cases

Table 4.8: Mean and standard deviation values of iteration, CC and RDMS values of different regularization parameter selection methods for five different noise cases

	Methods	CC Values	RDMS
15 µV measurement noise	LSQR	0.80 ± 0.14	0.58 ± 0.17
	Tikhonov	0.78 ± 0.15	0.60 ± 0.17
	TSVD	0.78 ± 0.15	0.60 ± 0.17
	Lanczos TTLS	0.75 ± 0.17	0.65 ± 0.19
	TTLS	0.72 ± 0.17	0.68 ± 0.19
150 µV measurement noise	LSQR	0.65 ± 0.20	0.77 ± 0.21
	Tikhonov	0.64 ± 0.22	0.77 ± 0.22
	TSVD	0.64 ± 0.22	0.78 ± 0.21
	Lanczos TTLS	0.57 ± 0.20	0.87 ± 0.20
	TTLS	0.54 ± 0.22	0.90 ± 0.21
15 µV meas. noise + 1.4 scaling Factor	LSQR	0.70 ± 0.17	0.73 ± 0.16
	Tikhonov	0.69 ± 0.18	0.74 ± 0.16
	TSVD	0.70 ± 0.16	0.73 ± 0.15
	Lanczos TTLS	0.70 ± 0.18	0.73 ± 0.15
	TTLS	0.69 ± 0.18	0.75 ± 0.16
15 µV meas. noise + 10 mm shift	LSQR	0.67 ± 0.12	0.76 ± 0.13
	Tikhonov	0.67 ± 0.14	0.77 ± 0.15
	TSVD	0.67 ± 0.13	0.76 ± 0.12
	Lanczos TTLS	0.66 ± 0.15	0.77 ± 0.15
	TTLS	0.65 ± 0.15	0.78 ± 0.16
15 µV meas. noise + 1.4 scaling Factor + 10 mm shift	LSQR	0.63 ± 0.17	0.82 ± 0.17
	Tikhonov	0.62 ± 0.18	0.84 ± 0.19
	TSVD	0.63 ± 0.14	0.81 ± 0.16
	Lanczos TTLS	0.63 ± 0.16	0.82 ± 0.16
	TTLS	0.63± 0.14	0.83 ± 0.15

Here, the performances of regularization methods will be visually evaluated. For this purpose, the quality and shape of the waveform will be evaluated by using the figures obtained with MAP3D.

Figure 4.34 and Figure 4.35 show the Map3d images of real and reconstructed epicardial potentials for the "15 µV – measurement noise" case at 6 ms and 50 ms after excitation, respectively. The initial stimulation site can be seen in the real epicardial potentials at 6 ms. LSQR, Tikhonov and TSVD detected this ventricular ectopic focus, but wavefront is smoother than the original. At this time instant, TTLS also detected the ectopic focus, but there are also regions that also appear to be stimulation sites. However, different from the max CC case, at this time instant Lanczos TTLS could not detect the activated region. In Figure 4.35, activation has propagated through most of the epicardial surface at 50 ms after excitation. At this time instant, similar results are obtained with the max CC case; all methods have constructed similar epicardial potential maps and have detected activated and wavefront regions correctly, but wavefronts are smoother in the reconstructions than the original, especially for the TTLS and Lanczos TTLS solutions.
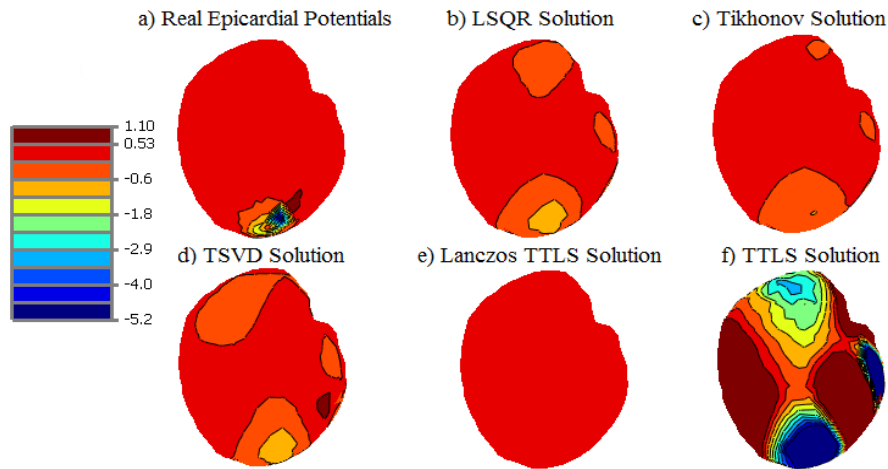
Figure 4.34: Epicardial Potential Maps of reconstructed solutions for 15 µV noisy data: a) Real Potential Distribution at the 6 ms b) LSQR Solution c) Tikhonov Solution d) TSVD Solution e) Lanczos TTLS Solution f) TTLS Solution
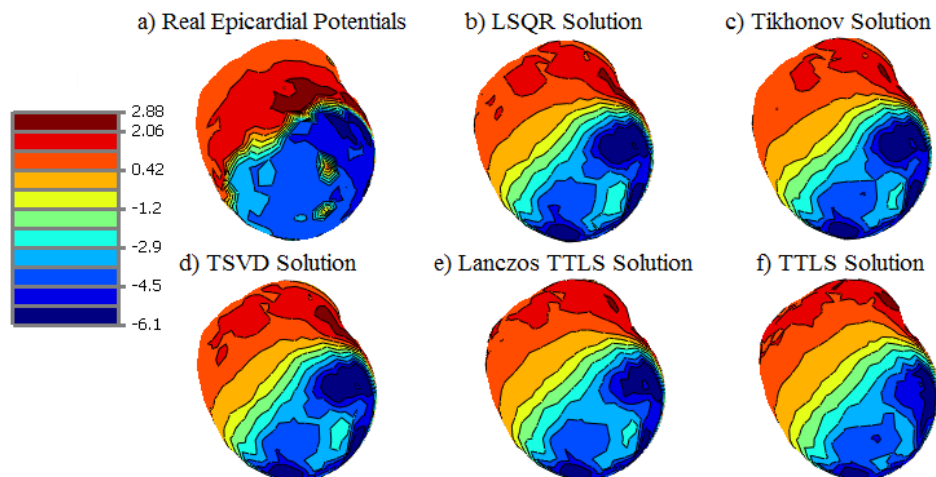
Figure 4.35: Epicardial Potential Maps of reconstructed solutions for 15 µV noisy data: a) Real Potential Distribution at the 50 ms b) LSQR Solution c) Tikhonov Solution d) TSVD Solution e) Lanczos TTLS Solution f) TTLS Solution

Figure 4.36 shows the Map3d images of real and reconstructed epicardial potentials for the "150 μV – measurement noise" case at 40 ms after excitation. From Figure 4.36, it is observed that similar results are obtained with the max CC case. LSQR, Tikhonov and TSVD find the excited region; among these, LSQR and Tikhonov construct smoother waveforms. At this time instant, Lanczos TTLS and TTLS are unable to detect the excited region correctly. When epicardial potentials are inspected for this time instant, these values are amplified 4 times by TTLS and 5 times by Lanczos TTLS. Different form the max CC case, TTLS has less amplification of estimated voltages, because smaller truncation number is selected by the GCV method for this time instant. This seems inconsistent with max CC approach, because the voltages amplified more at max CC case, but at CC computation the mean of the estimated potential is subtracted from itself. Therefore the effect of high voltage values is decreased.
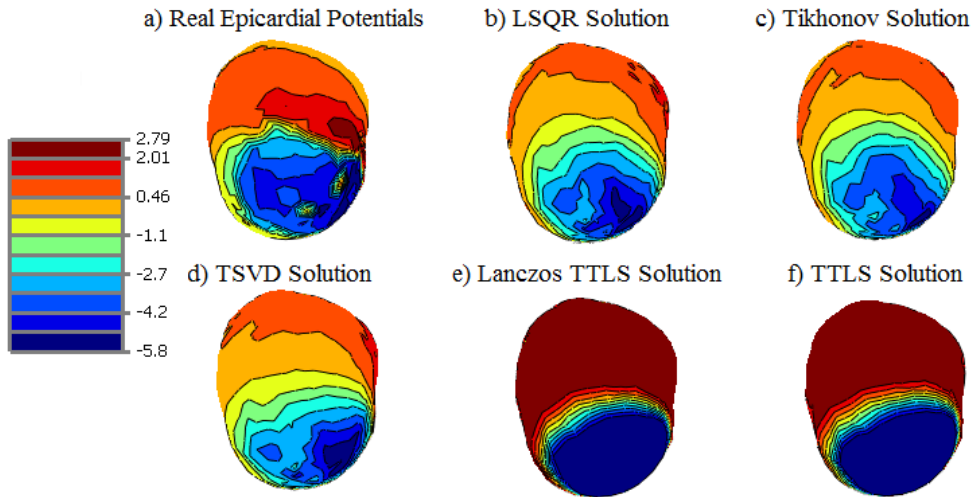
Figure 4.36: Epicardial Potential Maps of reconstructed solutions for 150 μV noisy data: a) Real Potential Distribution at the 40 ms b) LSQR Solution c) Tikhonov Solution d) TSVD Solution e) Lanczos TTLS Solution f) TTLS Solution
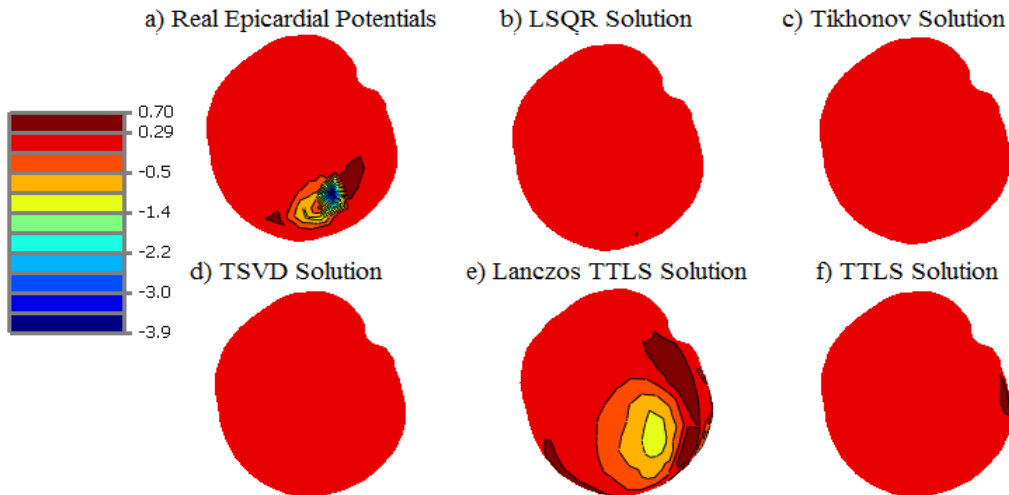
Figure 4.37: Epicardial Potential Maps of reconstructed solutions for 15 μV measurement noise added data with 1.4 scaling geometric error: a) Real Potential Distribution at the 4 ms b) LSQR Solution c) Tikhonov Solution d) TSVD Solution e) Lanczos TTLS Solution f) TTLS Solution

Figure 4.37 shows the Map3d images of real and reconstructed epicardial potentials for the "15 μV measurement noise and 1.4 scaling geometric error" case at 4 ms after excitation. In this figure, initial activation point can be observed on the real epicardial potential map. However, only Lanczos TTLS has detected this initial activation, although it is smoothed. LSQR, TSVD, TTLS and Tikhonov are unable to detect the initial activation. Different from the max CC case, TTLS could not

detect the initial activation region, which is caused by selection of a smaller truncation number. For later time instants, similar waveforms are observed with the max CC case.

Figure 4.38 shows the Map3d images of real and reconstructed epicardial potentials for the "15 µV - measurement noise and 10 mm shift geometric error" case at 6 ms after excitation. In this figure, initial activation is seen in the real epicardial potential. All methods detect the initial activation, but LSQR, TSVD, Lanczos TTLS and Tikhonov give smoother results than TTLS. TTLS focus to the activated site better than the others for this time instant. When compared with the max CC case, the wavefront generated by TTLS and Lanczos TTLS are smoother. At later time instants, there are not important differences with the max CC case.
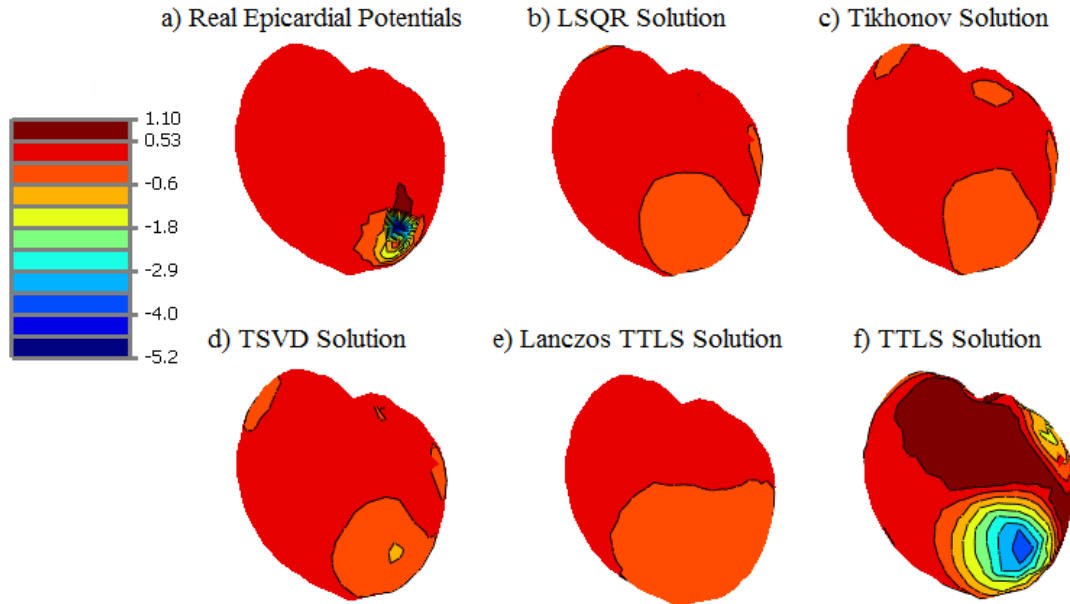
Figure 4.38: Epicardial Potential Maps of reconstructed solutions for 15 µV measurement noise added data with 10 mm shift geometric error: a) Real Potential Distribution at the 10th ms b) LSQR Solution c) Tikhonov Solution d) TSVD Solution e) Lanczos TTLS Solution f) TTLS Solution

4.7. Run Time Analysis of Regularization Methods

In this section, run time comparison of regularization methods is given. Run times are compared by using a computer with 2.7 GHz i7 processor and 4 GB RAM. To make a fair comparison between methods, 20 different lambda values are used by Tikhonov regularization method; maximum truncation numbers used by TSVD, TTLS and Lanczos TTLS are selected as 20; and LSQR is iterated 20 times and regularization parameter is selected by GCV method. The results obtained by this analysis are given in Figure 4.39 for one time instant during the QRS cycle. As it can be seen from this figure, regularization methods using SVD such as Tikhonov regularization, TSVD and TTLS take longer time than the other two. However, Lanczos bidiagonalization based methods LSQR and Lanczos TTLS take shorter time when compared with other three regularization methods. Lanczos TTLS also uses singular value decomposition but with this method, only the SVD of the smaller sized matrix obtained by Lanczos bidiagonalization is calculated. The reason for the time difference is that Lanczos bidiagonalization method is computationally more efficient than SVD when transfer matrix is large or sparse.

71
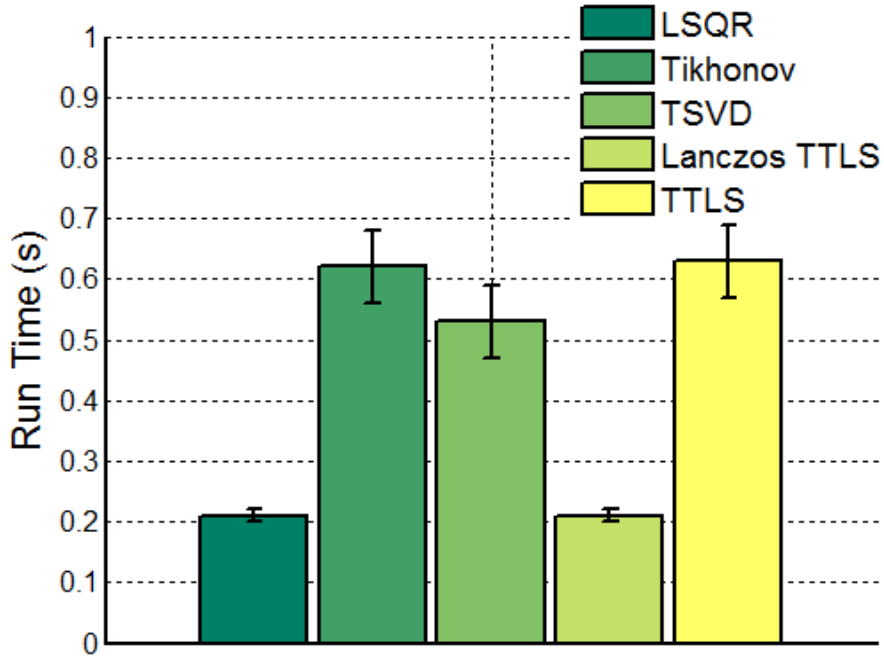
Figure 4.39: Average and Standard deviation of run time of five regularization methods

Total run times of these algorithms during QRS cycle (97 time instants) are also given in Table 4.9. During this test, 20 parameters are tried for all of the regularization methods as explained before. According to this table, Lanczos TTLS and LSQR are the fastest methods among these regularization methods, whereas Tikhonov regularization and TTLS are the slowest ones.

Note that, for this comparison, 20 iteration number or lambda samples are used. However, appropriate truncation or iteration number, or the lambda value yielding the maximum CC value is different for all methods and noise levels. As, we have found before Lanczos TTLS finds its best solutions with smaller truncation numbers when compared with other methods. Therefore, we can say Lanczos TTLS is the fastest regularization method among LSQR, TTLS, TSVD and Tikhonov regularization.

Table 4.9: Total run time of regularization methods

Methods	Total Run Time (s)
LSQR	21
Tikhonov	60
TSVD	51
Lanczos TTLS	20
TTLS	61

CHAPTER 5

CONCLUSION

In this study, we have used five different methods for solving the inverse problem of ECG. These methods are Tikhonov regularization, Least Squares QR method, Truncated Singular Value Decomposition, Truncated Total Least Squares method and Lanczos Truncated Total Least Squares method. The reconstructed solutions of these methods are compared with each other and with the real epicardial potentials. In these comparisons, the regularization parameters are selected by using the maximum correlation coefficient method and most preferable regularization parameter selection method.

In our results, we observe that TSVD and Tikhonov regularization methods produced very similar results, because as explained in the theory section, the filter factors used by each method to decrease error in the system are very similar; Tikhonov regularization adds a damping factor to the SVD components and thus filters the effect of smaller singular values. On the other hand, TSVD ignores the components related with the smaller singular values. In other words, TSVD has a sharper filter and Tikhonov has a smoother filter. The consequence of the difference between these filter factors is that the Tikhonov regularization yields smoother inverse solutions than the TSVD. Moreover, TSVD result changes significantly with every truncation parameter change, however Tikhonov is a continuous method and smoothly converges to the estimated epicardial potentials. When Tikhonov regularization and TSVD are compared in terms of run time, it is seem that TSVD is a bit faster than Tikhonov because, it directly truncates smaller singular values but Tikhonov adds a damping factor to all singular values as explained before.

TSVD and TTLS algorithms work similarly, they both try to neglect the effects of smaller singular values and try to obtain a better posed matrix. The main difference between these methods is that TTLS algorithm tries to make changes in the transfer matrix and in the body surface potentials but TSVD only uses the transfer matrix. For this reason, TTLS is proposed as a good method for dealing with geometrical errors in the system. In our simulations with using real epicardial potentials and realistic torso model, in the case with only the measurement error, TTLS gives worse results than the other approaches. When geometric error is also added to the system, the performance of TTLS is comparable to the other methods. Thus, TTLS may only be a good method for the solution of inverse ECG problem when there is geometrical error but not a large amount of measurement noise in the system. In terms of run time, TTLS gives similar result with SVD based methods such as TSVD and Tikhonov regularization.

The LSQR algorithm is an iterative method based on the bidiagonalization procedure by using Krylov subspace, which can be used as the regularization method for the solution of inverse electrocardiography problem at early iterations. Bidiagonalization procedure used by LSQR algorithm does not change the transfer matrix, it only multiplies the transfer matrix by itself and/or its transpose, therefore sparsity of the transfer matrix is not destroyed. However, matrix factorization such as SVD used by Tikhonov regularization, TSVD or TTLS destroys the sparsity of the transfer matrix. For this reason, LSQR is faster than the SVD based methods as shown in run time comparisons. When the performance of LSQR is compared with other methods, it can produce better or the same results for all of the error types. Therefore it seems to be the best method among the compared methods.

Lanczos TTLS is a modified version of the TTLS method. Like the LSQR method, Lanczos bidiagonalization procedure is used instead of SVD. For this reason, it is computationally more efficient than the TTLS, because SVD takes longer time, especially when transfer matrix is large as explained before. When the performance of Lanczos TTLS is compared with other methods for the

max CC case, it is seen that CC values of Lanczos TTLS is 2% smaller than those obtained by TSVD method, and 3% smaller than those obtained by Tikhonov regularization and LSQR methods when only "15 µV – measurement error" is considered. For the "150 µV – measurement error" case, Lanczos TTLS's performance is 7% worse than Tikhonov regularization, TSVD and LSQR methods. For the geometric error cases, there is not much difference from other methods. By using run time comparisons, it is seen that Lanczos TTLS is one of the fastest regularization methods along with LSQR, and it gives better results than TTLS in most cases, therefore it can be an alternative method for solving the inverse ECG problem, especially when there is geometric error in the system.

All of the regularization methods have their own advantages or disadvantages, but regularization process is not complete without selecting a regularization parameter selection method. The accuracy of the regularization methods directly depend on the determination of correct regularization parameter. Some methods such as Tikhonov regularization method needs continuous regularization parameter like lambda to control the trade-off between the residual error and the constraint norm. Others, such as TSVD, TTLS and Lanczos TTLS methods need a discrete regularization parameter to decrease the effects of noise by truncating smaller singular values. LSQR method needs a discrete optimum iteration number to find the estimated solutions. For these reasons, the performances of regularization parameter selection methods; L-curve method, generalized cross-validation and maximum correlation coefficient are compared for all of the regularization methods. In addition, composite residual and smoothing operator is also tested for only Tikhonov method, because it is applicable for only continuous methods. These methods give similar results at low noise levels, but when noise level is high, GCV method becomes more stable than the others. L-curve method also needs to detect the corner of the curve, so it increases computational work, but it is observed that GCV gives good results by selecting the rightmost low value on the curve. CRESO does not have a wide usage area because most of the regularization methods are not continuous; for this reason it is not preferable.

5.1. Future Work

- We implemented spatial methods to solve Inverse ECG problem and compared their performances. These methods can be compared with spatio-temporal regularization methods.
- Some optimization techniques such as the genetic algorithm can also be used to determine the regularization parameter for the regularization methods used here.

REFERENCES

[1] World Health Organization, The top 10 causes of death, http://www.who.int/mediacentre/factsheets/fs310/en/index.html, last visited on 23 September 2012.

[2] Malmivuo, J., and Plonsey, R., Bioelectromagnetism, New York, Oxford University Press, 1995.

[3] Ramanathan, C., Ghanem, R.N., Jia, P., Ryu, K., and Rudy, Y., Noninvasive electrocardiographic imaging for cardiac electrophysiology and arrhythmia, Nature Medicine, 10 (4):422–428, 2004.

[4] AETNA, Clinical Policy Bulletin: Body Surface Potential Mapping, http://www.aetna.com/cpb/medical/data/700_799/0705.html, last visited on 15 September 2012.

[5] Ambroggi, L.D., and Corlan, A.D., Clinical use of body surface potential mapping in cardiac arrhythmias, Anatol J Cardiol: 7 Suppl 1; 8-10, 2007.

[6] Johnston, P.R., and Gulrajani, R.M., A New Method for Regularization Parameter Determination in the Inverse Problem of Electrocardiography, IEEE Transactions on Biomedical Engineering, Vol. 44, No 1, January 1997.

[7] Shou, S., Jiang, M., Xia, L., Wei, Q., Liu, F., and Crozier, S., A comparison of different choices for the regularization parameter in inverse electrocardiography models, Proceedings of the 28th IEEE EMBS Annual International Conference New York City, USA, Aug 30-Sept 3, 2006

[8] Throne, R.D., Olson, L.G., Hrabik, T.J., and Windle, J.R., Generalized Eigensystem Techniques for the Inverse Problem of Electrocardiography Applied to a Realistic Heart-Torso Geometry, IEEE Transactions on Biomedical Engineering, Vol. 44, No. 6, June 1997

[9] Shou, G., Xia, L., and Jiang, M., Solving the Electrocardiography Inverse Problem by Using an Optimal Algorithm Based on the Total Least Squares Theory, Third International Conference on Natural Computation, IEEE, 2007.

[10] Paige, C.C., and Saunders M.A., LSQR: An algorithm for sparse linear equations and sparse least squares, ACM Transactions on Mathematical Software, Vol. 8, No. 1, March 1982.

[11] Jiang, M., Xia, L., Shou, G., and Tang, M., Combination of the LSQR method and a genetic algorithm for solving the electrocardiography inverse problem, Phys. Med. Biol. 52, 1277–1294, 2007.

[12] Shou, G., Xia, L., Jiang, M., Wei, Q., Liu, F., and Crozier, S., Truncated Total Least Squares: A New Regularization Method for the Solution of ECG Inverse Problems, IEEE Transactions on Biomedical Engineering, Vol. 55, No. 4, April 2008.

[13] Fierro, R.D., Golub, G.H., Hansen, P.C., and O'Leary, D. P., Regularization by Truncated Total Least Squares, SIAM J. Sci. Comput., Vol. 18, No. 4, pp. 1223- 1241, July 1997.

[14] Brooks, D.H., Ahmad, G.F., Macleod, R.S., and Maratos, G.M., Inverse Electrocardiography by simultaneous imposition of multiple constraints. IEEE Trans. Biomed. Eng., 46-1:3–18, 1999.

[15] Berrier, K.L., Sorensen, D.C., and Khoury, D.S., Solving the inverse problem of electrocardiography using a duncan and horn formulation of the kalman filter. IEEE Trans. Biomed. Eng., 51:507–515, 2004.

[16] El-Jakl, J., Champagnat, F., and Goussard, Y., Time-space regularization of the inverse problem of electrocardiography. IEEE EMBC and CMBEC, pages 213– 214, 1995.

[17] Joly, D., Goussard, Y., and Savard, P., Time-recursive solution to the inverse problem of electrocardiography a model-based approach. Proc. IEEE-EMBS, pages 767–768, 1993.

[18] Aydin, U., and Serinagaoglu, Y., Use of activation time based kalman filtering in inverse problem of electrocardiography. IFMBE Proceedings, 22:1200–1203, 2008.

[19] Aydin, U., and Serinagaoglu, Y., Comparison of bayesian map estimation and kalman filter methods in the solution of spatio-temporal inverse ecg problem. Proc. WC, 2009.

[20] Serinagaoglu, Y., Brooks, D.H., and MacLeod, R.S., Bayesian solutions and performance analysis in bioelectric inverse problems. IEEE Trans. Biomed. Eng., 52-6:1009–1020, 2005.

[21] Onal, M., and Serinagaoglu, Y., Spatio-temporal solutions in inverse electrocardiography. IFMBE Proceedings, 22:180–183, 2008.

[22] Farina, D., Jiang, Y., Skipa, O., Dossel, O., Kaltwasser, C., and Bauer, W.R., The use of the simulation results as a priori information to solve inverse problem of ECG for a patient. Computers in Cardiology, 32:571–574, 2005.

[23] He, B., Li, G., and Zhang, X., Noninvasive imaging of cardiac transmembrane potentials within three-dimensional myocardium by means of a realistic geometry anisotropic heart model. IEEE Transactions on Biomedical Engineering Vol. 50, No. 10, 1190- 1202, 2003.

[24] Hansen, P.C., Regularization Tools, Numerical Algorithms 6, pp 1-34, 1994.

[25] Hansen, P.C., Rank- deficient and Discrete Ill- Posed Problems, SIAM, 1997.

[26] Hansen, P.C., Regularization Tools, March 1998.

[27] Colli-Franzone, P., Gueri, L., Taccardi, B., and Viganotti, C., Finite element approximation of regularized solutions of the inverse potential problem of electrocardiography and applications to experimental data. Calcalo 1985.

[28] Johnston, P.R., and Gulrajani, R.M., Selecting the Corner in the L-Curve Approach to Tikhonov Regularization, IEEE Transactions on Biomedical Engineereing, Vol. 47, No. 9, September 2000.

[29] MacLeod, R.S., and Johnson, C.R., Map3d: Interactive scientific visualization for bioengineering data. IEEE EMBS 1993, pages 30–31, 1993.

[30] Hansen, P.C., and O'Leary, D.P., The Use of L Curve in the Regularization of Discrete Ill Posed Problems, SIAM J. Sci,. Comput. Vol. 14, No. 6, pp. 148-1503, November 1993.

[31] Wikipedia, Heart, 2012. http://en.wikipedia.org/wiki/Heart, last visited on 12 September 2012.

[32] Texas Heart Institute, Anatomy of the heart, http://texasheart.org/HIC/Anatomy/anatomy2.cfm, last visited on 2 August 2012.

[33] Health Information, Anatomy of the Heart, http://healthinformation1. 4arabs.com/heart/2.html, last visited on 3 September 2012.

[34] Wikipedia, Cardiac action potential, http://en.wikipedia.org/wiki/Cardiac_action_ potential, last visited on 7 September 2012.

[35] Understanding cardiovascular diseases, Open University Course Team, Milton Keynes: Open University Worldwide, http://www3.open.ac.uk/study/undergraduate/ course/sk121.htm, last visited on 17 November 2012.

[36] Homoud, M.K., and Tufts, M.D., Introduction to Electrocardiography New England Medical Center Spring, 2008.

[37] Wikipedia, Electrocardiography, http://en.wikipedia.org/wiki /Electrocardiography, last visited on 5 August 2012.

[38] Healthy Heart, The electrical activity of the heart, http://www.healthyheart.nhs.uk/heart_works/heart03.shtml, last visited on 8 August 2012.

[39] Gulrajani R.M., The forward and inverse problems of electrocardiography. IEEE Eng Med Biol Mag., 17:84–101,122, 1998.

[40] Plonsey, R., and Barr, R.C., Bioelectricity A Quantitative Approach, Boston, MA: Springer Science+Business Media, LLC, 2007.

[41] Oosterom, V., Source models in inverse electrocardiography. International Journal of Bioelectromagnetism, Sept.:211–214, 2003.

[42] Nyssen, E., Muynck, P.D., Mechele, E., and Comelis, J., ECG Signal Information and diagnostic information in multipoles, 1998.

[43] MacLeod, R.S., and Brooks, D.H., Recent progress in inverse problems in electrocardiology. IEEE Eng Med Biol Magazine, 17 (1):73–83, 1998.

[44] Pullan, A.J., Paterson, D., and Greensite, F., Noninvasive imaging of cardiac electrophysiology. Phil. Trans. R. Soc. Lond. A, 359:1277–1286, 2001.

[45] Pullan, A.J., Cheng, L.K., Nash, M. P., Bradley, C.P., and Paterson, D.J., Noninvasive electrical imaging of the heart: Theory and model development. Annals of Biomedical Engineering, 29:817836, 2001.

[46] Nash, M.P., and Pullan, A.J., Challenges facing validation of noninvasive electrical imaging of the heart. A. N. E, 10-1:73–82, 2005.

[47] Mesnarz, B., Tilg, B., Modre, R., Fischer, G., and Hanser, F.A., new spatio-temporal regularization approach for reconstruction of cardiac transmembrane potential patterns. IEEE Trans. Biomed. Eng., 51-2:273–281, 2004.

[48] Arthur, R.M., Evaluation and Use of a Human Dipole plus Quadrupole Equivalent Cardiac Generator. PhD.Thesis, Univ Pennsylvania; 1968.

[49] Farina, D., Forward and inverse problem of electrocardiography clinical investigations, Karisruhe Transactions on Biomedical Engineering, 2008.

[50] Jiang, Y., Solving the inverse problem of electrocardiography in a realistic environment, Karisruhe Transactions on Biomedical Engineering, 2010.

[51] Bradley, C.P., Pullan, A.J., and Hunter, P.J. Effects of material properties and geometry on electrocardiographic forward simulations. Annals of Biomedical Engineering, 28:721–741, 2000.

[52] Cheng, L.K., Bradley, C.P., and Pullan, A.J., Effects of experimental and modeling errors on electrocardiographic inverse formulations. IEEE Trans. Biomed. Eng., 50:23–32, 2003.

[53] Babaeizadeh, S., and Brooks, D.H., Using electrical impedance tomography for inverse electrocardiography. CDSP, NEU, Boston, MA, USA, 2004.

[54] Cheng L.K., Sands G.B., French R.L., Withy S.J., Wong S.P., Legget M.E., Smith W.M., and Pullan A.J., Rapid construction of apatient-specific torso model from 3D ultrasound for non-invasive imaging of cardiac electrophysiology. Med Biol Eng Comput46(3):325–330, 2005.

[55] Shou, G., and Xia, L Solving the ECG Forward Problem by Means of Standard h- and h-Hierarchical Adaptive Linear Boundary Element Method: Comparison With Two Refinement Schemes, IEEE Transactions on Biomedical Engineering, Vol. 56, No. 5, May 2009.

[56] Shou, G., Xia, L., Jiang, M., Liu, F., and Crozier, S., Forward and Inverse Solutions of Electrocardiography Problem Using an Adaptive BEM Method, Springer-Verlag Berlin Heidelberg, 2007.

[57] Kauppinen, P., Hyttinen, J., Laarne, P., and Malmivuo, J., A software implementation for detailed volume conductor modelling in electrophysiology using finite difference method, Ragnar Granit Institute, Tampere University of Technology, 1998.

[58] Kurt, A., Boundary Element Formulation and its solution in Forward Problem of Electrocardiography by using a realistic torso model, April 2006.

[59] Li, Z., Zhang, Y., Zhu, S., and He, B., Comparison of Meshless FEM and Conventional FEM for Solving ECG Forward Problem: A Simulation Study, IEEE, 2007.

[60] Rosenfeld, M., Tanami, R., and Abboud, S., Numerical Solution of the Potential Due to Dipole Sources in Volume Conductors With Arbitrary Geometry and Conductivity, IEEE, 1996.

[61] Gavgani, A.M., and Serinagaoglu, Y., Use of Genetic Algorithm for Selection of Regularization Parameters in Multiple Constraint Inverse ECG Problem, 33rd Annual International Conference of the IEEE EMBS, 2011.

[62] Ghandi, F.A., Brooks, D.H., and Macleod, R.S., An admissible solution approach to inverse electrocardiography, annals of biomedical engineering. Annals of Biomedical Engineering, 26:278–292, 1998.

[63] Twomey, S., On the numerical solution of Fredholm integral equations of the first kind by the inversion of the linear system produced by quadrature. JACM 10: 97-101, 1963.

[64] Phillips, D.L., A technique for the numerical solution of certain integral equations of the first kind, J. ACM 9, 84-97, 1962.

[65] Jiang, M., Xia, L., and Shou, G., The Use of Genetic Algorithms for Solving Inverse Problem of Electrocardiography, EMBS Annual International Conference, 2006.

[66] Jiang, M., Xia, L., and Shou, G., The use of Genetic Algorithms for optimizing the regularized solutions of the ill-posed problems, Second International Symposium on Intelligent Information Technology Application, IEEE, 2008.

[67] Jiang, M., Xia, L., Shou, G., and Tang, M., Combination of the LSQR method and a genetic algorithm for solving the electrocardiography inverse problem, Phys. Med. Biol. 52, 1277-1294, 2007.

[68] Sarıkaya, S., Weber, G.W., and Serinagaoglu, Y., Combination of Conventional Regularization Methods and Genetic Algorithm for Solving the Inverse Problem of Electrocardiography, The International Symposium on Health Informatics and Bioinformatics, 13 -20, 2010.

[69] He, B., and Wu, D., Imaging and visualization of 3-d cardiac electrical activity. IEEE Trans. Inf. Tech. in Biomedicine, 5-3:181–186, 2001.

[70] Throne, R.D., and Olson, L.G., A Generalized Eigensystem Approach to the Inverse Problem of Electrocardiography, IEEE Transactions on Biomedical Engineering Vol. 41, No. 6, 592- 600, 1994.

[71] Throne, R.D., Olson, L.G, Hrabik, T.J., and Windle, J.R., Generalized Eigensystem Techniques for the Inverse Problem of Electrocardiography Applied to Realistic Heart-Torso Geometry, IEEE Transactions on Biomedical Engineering Vol. 46, No. 6, 447 - 454, 1997.

[72] Nash, M.P., Bradley, C.P., Kardos, A., Pullan, A.J., and Paterson, D.J., An experimental model to correlate simultaneous body surface and epicardial electropotential recordings in vivo. Chaos, Solutions and Fractals, 13:1735–1742, 2002.

[73] Tikhonov, A.N., and Arsenin V.Y., Solutions of ill- posed problem, Winston&Sons, New York, 1977.

[74] Colli-Franzone, P., Gueri, L., Taccardi, B., and Viganotti, C., Finite element approximation of regularized solutions of the inverse potential problem of electrocardiography and applications to experimental data. Calcalo 1985.

[75] Hansen, P.C., Rank-deficient and discrete ill-posed problems, Numerical Aspects of Linear Inversion, SIAM, 1998.

[76] Golub, G., and Kahan, W., Calculating the singular values and pseudo inverse of a matrix, SIAM J. Number. Analy. 2, pp. 205-224, 1965.

[77] Golub, G., and Loan, C.F.V., Matrix Computations (2nd Edition), The Johns Hopkins University Press, 1989.

[78] Huffel, S.V., and Vandewalle, J., The Total Least Squares Problem: Computational Aspects and Analysis, Frontiers in Applied Mathematics, Society for Industrial Mathematics, Philadelphia, Pa, USA, 1991.

[79] Golub, G., and Loan, C.F.V., "An analysis of the total least squares problem," SIAM Journal on Numerical Analysis, vol. 17, no. 6, pp. 883–893, 1997.

[80] Hansen, P.C., The L-curve and its use in the numerical treatment of inverse problems, Department of Mathematical Modeling, Technical University of Denmark, DK-2800 Lyngby, Denmark, 2000.

[81] MacLeod, R.S., Lux, R.L., and Taccardi. B., A possible mechanism for electrocardiographically silent changes in cardiac repolarization. J. Electrocardiol., 30:114–121, 1997.

[82] MacLeod, R.S., Lux, R.L., and Taccardi. B., Electrocardiographic mapping in a realistic torso tank preparation. Proceedings of IEEE Engineering in Medicine and Biology Society in 17th Annual Conference, IEEE Press, 1:245–246, 1995.

[83] Ramanathan, C., and Rudy, Y., Electrocardiographic imaging: I. Effect of torso inhomogeneities on body surface electrocardiographic potentials. Journal of Cardiovascular Electrophysiology, 12:229–240, 2001.

[84] Messinger-Rapport, B. J., and Rudy. Y., The inverse problem in electrocardiography: A model study of the effects of geometry and conductivity parameters on the reconstruction of epicardial potentials. IEEE Trans. Biomed. Eng., 33- 7:667–676, 1986.

[85] Hansen, P.C., and Jenses, T.K., An Adaptive Pruning Algorithm for the Discrete L-Curve Criterion, Elsevier Science, 2004

[86] Oosterom, A.V., and Huiskamp, G.J., Implicit and explicit constraints in inverse electrocardiography. J. Electrocardiol., 25:87–92, 1992.

[87] Gulrajani, R.M., The forward and inverse problem of electrocardiography: Gaining a better qualitative and quantitative understanding of the heart's electrical activity. IEEE Engineering in medicine and biology, 17:84–122, 1998.

[88] Rodriguez, G., and Theis, D., An algorithm for estimating the optimal regularization parameter by the L-curve Rendiconti di Matematica, Serie VII Volume 25, Roma, 2005.

[89] Stanley P C , Pilkington T C, Morrow M N, The effects of thoracic inhomogeneities on the relationship between epicardial and torso potentials, IEEE Trans Biomed Eng., vol. 33(3), pp. 273-284, 1986.

[90] Kauppinen P, Hyttinen J, Heinonen T, Malmivuo J, A detailed model of the thorax as a volume conductor based on the visible human man data, Ioumal of Medical Engineering, 22: 1.26-733, 1998.

APPENDIX A

MEASUREMENT OF EPICARDIAL POTENTIALS AND DETERMINATION OF BODY SURFACE POTENTIALS

The true epicardial potentials used for simulation of the body surface potentials and for validation of reconstructed solution of the inverse problem were measured from an isolated dog heart. The measurements were taken by a team at University of Utah Nora Eccles Harrison Cardiovascular Research and Training Institute (CVRTI) [81, 82]. The isolated dog heart was suspended in an electrolytic filled human thorax shaped fiberglass tank, and perfused by the circulatory system of a second dog under anesthesia. To place an appropriate electric load on the isolated heart, the electrolyte was a mixture of isotonic saline and sucrose with a bulk resistivity of 500 Ω-cm, similar to the human thorax. The epicardial potentials were recorded from 490 points with 1000 samples/s sampling rate using a nylon sock electrode with silver wires, slipped over the ventricles. During measurements, the heart was stimulated from the ventricles to simulate ventricular arrhythmias and the epicardial potentials were recorded for 97 time instants. These recordings contain measurement errors, however during this study; measurements obtained by sock electrode are accepted as real and performance of regularization methods are compared with these measured epicardial potentials.

The forward transfer matrix relating the measured epicardial potentials to the body surface potentials was calculated using BEM [56]. The code was developed previously in our laboratory as part of a research project funded by TÜBİTAK (Grant number: 105E070). Theoretical derivation of the forward transfer matrix is presented in the rest of this chapter.

To solve the forward problem of ECG in an inhomogeneous torso model, a similar approach with Stanley *et al.* [89] is used. In this study, potentials on the heart are represented by epicardial potentials.
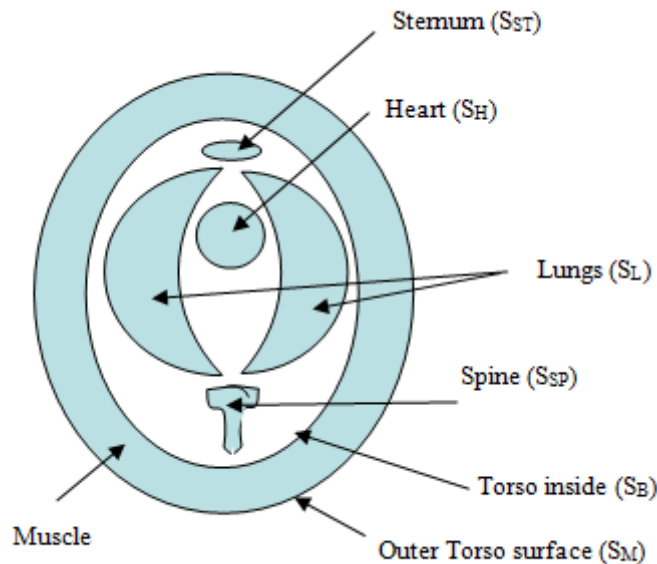

Figure A.1: Torso model used in Forward solution

Torso model used in forward solution is shown in Figure A.1. Here, tissues and organs included in the model are the heart (outer surface: S_H), the lungs (outer surface: S_L), the spine (outer surface:

S_{SP}), the sternum (outer surface: S_{ST}), inside of torso surface surrounding these organs (S_B), and muscle tissue at outside of torso surface (S_M). Muscle tissue is defined as the outer surface of the body. BEM formulation is done by using this torso model and fat tissue is not included in formulation.

By using Green's second identity, a relationship between position dependent scalars A and B can be written as:

$$\int_S (A\nabla B - B\nabla A)\cdot \mathbf{n}\, dS = \int_V (A\nabla^2 B - B\nabla^2 A)\, dV,$$
(A.1)

Here, $\mathbf{n}$ is the unit normal vector defined in the outward direction from surface S. For forward problem formulation, A can be defined as $1/r$ (r: distance from observation point to any point on surface S), B can be written as $\sigma\Phi$ (σ: conductivity at the observation point, Φ: potential at the observation point), then Equation A.1 can be written as:

$$\int_S \left(\frac{1}{r}\nabla(\sigma\Phi) - \sigma\Phi\nabla\left(\frac{1}{r}\right)\right)\cdot \mathbf{n}\, dS = \int_V \left(\frac{1}{r}\nabla^2(\sigma\Phi) - \sigma\Phi\nabla^2\left(\frac{1}{r}\right)\right) dV$$
(A.2)

Since there is no current source between epicardium and torso surface, Equation A.2 can be simplified as:

$$\int_S \left(\left(\frac{1}{r}\right)\nabla(\sigma\Phi) - \sigma\Phi\nabla\left(\frac{1}{r}\right)\right)\cdot \mathbf{n}\, dS = -\int_V \sigma\Phi\nabla^2\left(\frac{1}{r}\right) dV = 4\pi\sigma_o\Phi_o$$
(A.3)

The surface integral at the left side of Equation A.3 can be written by using surfaces defined in the torso model:

$$\int_S \left(\frac{1}{r}\nabla(\sigma\Phi) - \sigma\Phi\nabla\left(\frac{1}{r}\right)\right)\cdot \mathbf{n}\, dS$$

$$= -\int_{S_H} \left(\frac{1}{r_{OH}}\sigma_B\nabla\Phi_H - \sigma_B\Phi_H\nabla\left(\frac{1}{r_{OH}}\right)\right)\cdot \mathbf{n}_H\, dS_H$$

$$-\int_{S_L} \left(\frac{1}{r_{OL}}(\sigma_B-\sigma_L)\nabla\Phi_L - (\sigma_B-\sigma_L)\Phi_L\nabla\left(\frac{1}{r_{OL}}\right)\right)\cdot \mathbf{n}_L\, dS_L$$

$$-\int_{S_{ST}} \left(\frac{1}{r_{OST}}(\sigma_B-\sigma_{ST})\nabla\Phi_{ST} - (\sigma_B-\sigma_{ST})\Phi_{ST}\nabla\left(\frac{1}{r_{OST}}\right)\right)\cdot \mathbf{n}_{ST}\, dS_{ST}$$

$$-\int_{S_{SP}} \left(\frac{1}{r_{OSP}}(\sigma_B-\sigma_{SP})\nabla\Phi_{SP} - (\sigma_B-\sigma_{SP})\Phi_{SP}\nabla\left(\frac{1}{r_{OSP}}\right)\right)\cdot \mathbf{n}_{SP}\, dS_{SP}$$

$$-\int_{S_B} \left(\frac{1}{r_{OB}}(\sigma_M-\sigma_B)\nabla\Phi_B - (\sigma_M-\sigma_B)\Phi_B\nabla\left(\frac{1}{r_{OB}}\right)\right)\cdot \mathbf{n}_B\, dS_B$$

$$+\int_{S_M} \left(\frac{1}{r_{OM}}\sigma_M\nabla\Phi_M - \sigma_M\Phi_M\nabla\left(\frac{1}{r_{OM}}\right)\right)\cdot \mathbf{n}_M\, dS_M = 4\pi\sigma_o\Phi_o$$
(A.4)

Here, r_{OX} defines distance from observation point O to surface X. Since there is only air at the outside of the torso and its conductivity can be assumed as 0 ($\sigma_{air} << \sigma_M$), following boundary conditions can be written:

$$\sigma_M \nabla \Phi_M \cdot \mathbf{n}_M = 0$$

$$\sigma_L \nabla \Phi_L \cdot \mathbf{n}_L = \sigma_B \nabla \Phi_L \cdot \mathbf{n}_L$$

$$\sigma_{ST} \nabla \Phi_{ST} \cdot \mathbf{n}_{ST} = \sigma_B \nabla \Phi_{ST} \cdot \mathbf{n}_{ST} \qquad \text{(A.5)}$$

$$\sigma_{SP} \nabla \Phi_{SP} \cdot \mathbf{n}_{SP} = \sigma_B \nabla \Phi_{SP} \cdot \mathbf{n}_{SP}$$

$$\sigma_B \nabla \Phi_B \cdot \mathbf{n}_B = \sigma_M \nabla \Phi_B \cdot \mathbf{n}_B$$

$$\nabla \left(\frac{1}{r} \right) = -\frac{\mathbf{r}}{r^2} \cdot \mathbf{n}$$

Here, $\mathbf{r}$ is the unit vector pointing from the source point to the observation point. Then,

$$d\Omega_{ef} = \frac{\mathbf{r}_{ef} \cdot \mathbf{n}_f}{r_{ef}^2} dS_f$$

is an element of solid angle subtended at an observation point of i'th location on surface "e" by an area element on surface "f"). By using boundary conditions and given equations Φ_o can be written for an observation point inside the torso volume as:

$$\Phi_o = -\frac{1}{4\pi} \frac{\sigma_B}{\sigma_o} \int_{S_H} \frac{1}{r_{OH}} \nabla \Phi_H \cdot \mathbf{n}_H dS_H - \frac{1}{4\pi} \frac{\sigma_B}{\sigma_o} \int_{S_H} \Phi_H d\Omega_{OH} - \frac{1}{4\pi} \frac{(\sigma_B - \sigma_L)}{\sigma_o} \int_{S_L} \Phi_L d\Omega_{OL}$$

$$- \frac{1}{4\pi} \frac{(\sigma_B - \sigma_{ST})}{\sigma_o} \int_{S_{ST}} \Phi_{ST} d\Omega_{OST} - \frac{1}{4\pi} \frac{(\sigma_B - \sigma_{SP})}{\sigma_o} \int_{S_{SP}} \Phi_{SP} d\Omega_{OSP} - \frac{1}{4\pi} \frac{(\sigma_M - \sigma_B)}{\sigma_o} \int_{S_B} \Phi_B d\Omega_{OB} \quad \text{(A.6)}$$

$$- \frac{1}{4\pi} \frac{\sigma_M}{\sigma_o} \int_{S_M} \Phi_M d\Omega_{OM}$$

When the observation point is selected on only defined surfaces at the torso model, we obtain equations to solve the forward problem. For these surfaces, Equation A.6 can be written as:

$$\Phi_H = -\frac{1}{4\pi} \int_{S_H} \frac{1}{r_{HH}} \nabla \Phi_H \cdot \mathbf{n}_H dS_H - \frac{1}{4\pi} \int_{S_H} \Phi_H d\Omega_{HH} - \frac{1}{4\pi} \frac{(\sigma_B - \sigma_L)}{\sigma_B} \int_{S_L} \Phi_L d\Omega_{HL}$$

$$- \frac{1}{4\pi} \frac{(\sigma_B - \sigma_{ST})}{\sigma_B} \int_{S_{ST}} \Phi_{ST} d\Omega_{HST} - \frac{1}{4\pi} \frac{(\sigma_B - \sigma_{SP})}{\sigma_B} \int_{S_{SP}} \Phi_{SP} d\Omega_{HSP} - \frac{1}{4\pi} \frac{(\sigma_M - \sigma_B)}{\sigma_B} \int_{S_B} \Phi_B d\Omega_{HB} \quad \text{(A.7.a)}$$

$$- \frac{1}{4\pi} \frac{\sigma_M}{\sigma_B} \int_{S_M} \Phi_M d\Omega_{HM}$$

$$\Phi_L = -\frac{1}{4\pi} \int_{S_H} \frac{1}{r_{LH}} \nabla \Phi_H \cdot \mathbf{n}_H dS_H - \frac{1}{4\pi} \int_{S_H} \Phi_H d\Omega_{LH} - \frac{1}{4\pi} \frac{(\sigma_B - \sigma_L)}{\sigma_B} \int_{S_L} \Phi_L d\Omega_{LL}$$

$$- \frac{1}{4\pi} \frac{(\sigma_B - \sigma_{ST})}{\sigma_B} \int_{S_{ST}} \Phi_{ST} d\Omega_{LST} - \frac{1}{4\pi} \frac{(\sigma_B - \sigma_{SP})}{\sigma_B} \int_{S_{SP}} \Phi_{SP} d\Omega_{LSP} - \frac{1}{4\pi} \frac{(\sigma_M - \sigma_B)}{\sigma_B} \int_{S_B} \Phi_B d\Omega_{LB} \quad \text{(A.7.b)}$$

$$- \frac{1}{4\pi} \frac{\sigma_M}{\sigma_B} \int_{S_M} \Phi_M d\Omega_{LM}$$

$$\Phi_{ST} = -\frac{1}{4\pi}\int\limits_{S_H}\frac{1}{r_{STH}}\nabla\Phi_H\cdot\mathbf{n}_H dS_H -\frac{1}{4\pi}\int\limits_{S_H}\Phi_H d\Omega_{STH} -\frac{1}{4\pi}\frac{\left(\sigma_B-\sigma_L\right)}{\sigma_B}\int\limits_{S_L}\Phi_L d\Omega_{STL}$$

$$-\frac{1}{4\pi}\frac{\left(\sigma_B-\sigma_{ST}\right)}{\sigma_B}\int\limits_{S_{ST}}\Phi_{ST}d\Omega_{STST} -\frac{1}{4\pi}\frac{\left(\sigma_B-\sigma_{SP}\right)}{\sigma_B}\int\limits_{S_{SP}}\Phi_{SP}d\Omega_{STSP} -\frac{1}{4\pi}\frac{\left(\sigma_M-\sigma_B\right)}{\sigma_B}\int\limits_{S_B}\Phi_B d\Omega_{STB} \quad\text{(A.7.c)}$$

$$-\frac{1}{4\pi}\frac{\sigma_M}{\sigma_B}\int\limits_{S_M}\Phi_M d\Omega_{STM}$$

$$\Phi_{SP} = -\frac{1}{4\pi}\int\limits_{S_H}\frac{1}{r_{SPH}}\nabla\Phi_H\cdot\mathbf{n}_H dS_H -\frac{1}{4\pi}\int\limits_{S_H}\Phi_H d\Omega_{SPH} -\frac{1}{4\pi}\frac{\left(\sigma_B-\sigma_L\right)}{\sigma_B}\int\limits_{S_L}\Phi_L d\Omega_{SPL}$$

$$-\frac{1}{4\pi}\frac{\left(\sigma_B-\sigma_{ST}\right)}{\sigma_B}\int\limits_{S_{ST}}\Phi_{ST}d\Omega_{SPST} -\frac{1}{4\pi}\frac{\left(\sigma_B-\sigma_{SP}\right)}{\sigma_B}\int\limits_{S_{SP}}\Phi_{SP}d\Omega_{SPSP} -\frac{1}{4\pi}\frac{\left(\sigma_M-\sigma_B\right)}{\sigma_B}\int\limits_{S_B}\Phi_B d\Omega_{SPB} \quad\text{(A.7.d)}$$

$$-\frac{1}{4\pi}\frac{\sigma_M}{\sigma_B}\int\limits_{S_M}\Phi_M d\Omega_{SPM}$$

$$\Phi_B = -\frac{1}{4\pi}\frac{\sigma_B}{\sigma_M}\int\limits_{S_H}\frac{1}{r_{BH}}\nabla\Phi_H\cdot\mathbf{n}_H dS_H -\frac{1}{4\pi}\frac{\sigma_B}{\sigma_M}\int\limits_{S_H}\Phi_H d\Omega_{BH} -\frac{1}{4\pi}\frac{\left(\sigma_B-\sigma_L\right)}{\sigma_M}\int\limits_{S_L}\Phi_L d\Omega_{BL}$$

$$-\frac{1}{4\pi}\frac{\left(\sigma_B-\sigma_{ST}\right)}{\sigma_M}\int\limits_{S_{ST}}\Phi_{ST}d\Omega_{BST} -\frac{1}{4\pi}\frac{\left(\sigma_B-\sigma_{SP}\right)}{\sigma_M}\int\limits_{S_{SP}}\Phi_{SP}d\Omega_{BSP} -\frac{1}{4\pi}\frac{\left(\sigma_M-\sigma_B\right)}{\sigma_M}\int\limits_{S_B}\Phi_B d\Omega_{BB} \quad\text{(A.7.e)}$$

$$-\frac{1}{4\pi}\int\limits_{S_M}\Phi_M d\Omega_{BM}$$

$$\Phi_M = -\frac{1}{4\pi}\frac{\sigma_B}{\sigma_M}\int\limits_{S_H}\frac{1}{r_{MH}}\nabla\Phi_H\cdot\mathbf{n}_H dS_H -\frac{1}{4\pi}\frac{\sigma_B}{\sigma_M}\int\limits_{S_H}\Phi_H d\Omega_{MH} -\frac{1}{4\pi}\frac{\left(\sigma_B-\sigma_L\right)}{\sigma_M}\int\limits_{S_L}\Phi_L d\Omega_{ML}$$

$$-\frac{1}{4\pi}\frac{\left(\sigma_B-\sigma_{ST}\right)}{\sigma_M}\int\limits_{S_{ST}}\Phi_{ST}d\Omega_{MST} -\frac{1}{4\pi}\frac{\left(\sigma_B-\sigma_{SP}\right)}{\sigma_M}\int\limits_{S_{SP}}\Phi_{SP}d\Omega_{MSP} -\frac{1}{4\pi}\frac{\left(\sigma_M-\sigma_B\right)}{\sigma_M}\int\limits_{S_B}\Phi_B d\Omega_{MB} \quad\text{(A.7.f)}$$

$$-\frac{1}{4\pi}\int\limits_{S_M}\Phi_M d\Omega_{MM}$$

By solving integral equations given in Equation A.7, potential on the heart surface (Φ_H) can be defined by potentials on body surface (Φ_M). Analytical solution of these equations is possible for spherical or cylindrical torso model, but it is not possible for a realistic torso model. Therefore, integrals in Equation A.7 should be discretized, and ultimately, Φ_M can be written as:

$$\Phi_M = A\,\Phi_H \qquad\qquad\qquad\qquad\qquad\qquad\qquad\qquad\qquad\qquad\qquad\text{(A.8)}$$

where **A** is the forward transfer matrix that we want to calculate. To find this relationship between Φ_H and Φ_M, surface elements should be defined on all of the surfaces represented in Equation A.7 and these surface integrals should be written in terms of summations. For BEM solution, we need geometrical models of organs and tissues. For all of the defined surfaces S_H, S_L, S_{SP}, S_{ST}, S_B and S_M, number of the nodes on these surfaces are N_H, N_L, N_{SP}, N_{ST}, N_B and N_M respectively and triangular surface elements are used. Below, the discretization process is given for Equation A.7.a, and similar approach is used for other equations in Equation A.7.

$$-\Phi_H^i - \frac{1}{4\pi}\int_{S_H}\Phi_H^i d\Omega_{HH}^{ji} = \sum_j P_{HH}^{ji}\Phi_H^i$$

$$-\frac{1}{4\pi}\int_{S_H}\frac{1}{r_{HH}^{ji}}\nabla\Phi_H^i\cdot\mathbf{n}_H dS_H^i = \sum_j G_{HH}^{ji}\Gamma_H^i$$

$$-\frac{1}{4\pi}\frac{(\sigma_B-\sigma_L)}{\sigma_B}\int_{S_L}\Phi_L^i d\Omega_{HL}^{ji} = \sum_j P_{HL}^{ji}\Phi_L^i$$

$$-\frac{1}{4\pi}\frac{(\sigma_B-\sigma_{ST})}{\sigma_B}\int_{S_{ST}}\Phi_{ST}^i d\Omega_{HST}^{ji} = \sum_j P_{HST}^{ji}\Phi_{ST}^i \qquad\text{(A.9)}$$

$$-\frac{1}{4\pi}\frac{(\sigma_B-\sigma_{SP})}{\sigma_B}\int_{S_{SP}}\Phi_{SP}^i d\Omega_{HSP}^{ji} = \sum_j P_{HSP}^{ji}\Phi_{SP}^i$$

$$-\frac{1}{4\pi}\frac{(\sigma_M-\sigma_B)}{\sigma_B}\int_{S_B}\Phi_B^i d\Omega_{HB}^{ji} = \sum_j P_{HB}^{ji}\Phi_B^i$$

$$-\frac{1}{4\pi}\frac{\sigma_M}{\sigma_B}\int_{S_M}\Phi_M^i d\Omega_{HM}^{ji} = \sum_j P_{HM}^{ji}\Phi_M^i$$

Here j defines the node index; for the heart it starts from 1 and changes up to N_H and i is node index on the observation surface. Γ_H^i used in Equation A.9 is the gradient value of Φ_H^i. Equation A.7.a can be written in matrix form as:

$$P_{HH}\Phi_H + G_{HH}\Gamma_H + P_{HL}\Phi_L + P_{HST}\Phi_{ST} + P_{HSP}\Phi_{SP} + P_{HB}\Phi_B + P_{HM}\Phi_M = 0 \qquad\text{(A.10.a)}$$

When the same process is used for other equations in a.7, they can be written as:

$$P_{LH}\Phi_H + G_{LH}\Gamma_H + P_{LL}\Phi_L + P_{LST}\Phi_{ST} + P_{LSP}\Phi_{SP} + P_{LB}\Phi_B + P_{LM}\Phi_M = 0 \qquad\text{(A.10.b)}$$

$$P_{STH}\Phi_H + G_{STH}\Gamma_H + P_{STL}\Phi_L + P_{STST}\Phi_{ST} + P_{STSP}\Phi_{SP} + P_{STB}\Phi_B + P_{STM}\Phi_M = 0 \qquad\text{(A.10.c)}$$

$$P_{SPH}\Phi_H + G_{SPH}\Gamma_H + P_{SPL}\Phi_L + P_{SPT}\Phi_{ST} + P_{SPSP}\Phi_{SP} + P_{SPB}\Phi_B + P_{SPM}\Phi_M = 0 \qquad\text{(A.10.d)}$$

$$P_{BH}\Phi_H + G_{BH}\Gamma_H + P_{BL}\Phi_L + P_{BST}\Phi_{ST} + P_{BSP}\Phi_{SP} + P_{BB}\Phi_B + P_{BM}\Phi_M = 0 \qquad\text{(A.10.e)}$$

$$P_{MH}\Phi_H + G_{MH}\Gamma_H + P_{ML}\Phi_L + P_{MST}\Phi_{ST} + P_{MSP}\Phi_{SP} + P_{MB}\Phi_B + P_{MM}\Phi_M = 0 \qquad\text{(A.10.f)}$$

These matrices can then be combined into a single matrix equation:

$$\begin{bmatrix} \begin{bmatrix} P_{HH} \\ \begin{bmatrix} P_{LH} \\ P_{STH} \\ P_{SPH} \\ P_{BH} \end{bmatrix} \\ P_{MH} \end{bmatrix} & \begin{bmatrix} G_{HH} \\ \begin{bmatrix} G_{LH} \\ G_{STH} \\ G_{SPH} \\ G_{BH} \end{bmatrix} \\ G_{MH} \end{bmatrix} & \begin{bmatrix} \begin{bmatrix} P_{HL} & P_{HST} & P_{HSP} & P_{HB} \end{bmatrix} \\ \begin{bmatrix} P_{LL} & P_{LST} & P_{LSP} & P_{LB} \\ P_{STL} & P_{STST} & P_{STSP} & P_{STB} \\ P_{SPL} & P_{SPST} & P_{SPSP} & P_{SPB} \\ P_{BL} & P_{BST} & P_{BSP} & P_{BB} \end{bmatrix} \\ \begin{bmatrix} P_{ML} & P_{MST} & P_{MSP} & P_{MB} \end{bmatrix} \end{bmatrix} & \begin{bmatrix} P_{HM} \\ \begin{bmatrix} P_{LM} \\ P_{STM} \\ P_{SPM} \\ P_{BM} \end{bmatrix} \\ P_{MM} \end{bmatrix} \end{bmatrix} \begin{bmatrix} \Phi_H \\ \Gamma_H \\ \begin{bmatrix} \Phi_L \\ \Phi_{ST} \\ \Phi_{SP} \\ \Phi_B \end{bmatrix} \\ \Phi_M \end{bmatrix} = \mathbf{0} \qquad\text{(A.11)}$$

Since, we are trying to obtain a relationship between Φ_H and Φ_M, Φ_L, Φ_{ST}, Φ_{SP} and Φ_B can be combined as a single vector Φ_T and Equation A.11 can be written as:

$$\begin{bmatrix} P_{HH} & G_{HH} & P_{HT} & P_{HM} \\ P_{TH} & G_{TH} & P_{TT} & P_{TM} \\ P_{MH} & G_{MH} & P_{MT} & P_{MM} \end{bmatrix} \begin{bmatrix} \Phi_H \\ \Gamma_H \\ \Phi_T \\ \Phi_M \end{bmatrix} = \mathbf{0} \qquad\text{(A.12)}$$

Finally, Γ_H can be written in terms of Φ_T, Φ_H and Φ_M and a single equation is obtained:

$$\Phi_M = \left[\left(P_{MM} - G_{MH}G_{HH}^{-1}P_{HM} \right) + \left(P_{MT} - G_{MH}G_{HH}^{-1}P_{HT} \right) \left(P_{TT} - G_{TH}G_{HH}^{-1}P_{HT} \right)^{-1} \left(G_{TH}G_{HH}^{-1}P_{HM} - P_{TM} \right) \right]^{-1}$$

$$* \left[\left(G_{MH}G_{HH}^{-1}P_{HH} - P_{MH} \right) + \left(G_{MH}G_{HH}^{-1}P_{HT} \right) \left(P_{TT} - G_{TH}G_{HH}^{-1}P_{HT} \right)^{-1} \left(G_{TH}G_{HH}^{-1}P_{HH} - P_{TH} \right) \right] \Phi_H$$

(A.13)

When Equation A.8 and Equation A.13 are compared, it is seen that A matrix is equal to the matrix multiplying Φ_H. When this equation and Equation A.9 are carefully inspected, it can be seen that A is only dependent on torso geometry and conductivity values and it is independent of potentials on the heart surface. Thus, it can be used to relate epicardial potentials and potentials on the body surface. The torso geometry can be obtained by using CT and MRI images [90]. The conductivity values of lungs and thorax are selected as reported in literature [83]. The part of the torso volume not occupied by the heart and lungs was assigned an average conductivity of 0.002 $\Omega^{-1}cm^{-1}$ and average lung conductivity is selected as 0.005 $\Omega^{-1}cm^{-1}$. By using these conductivity values, transfer matrix relating torso potentials to epicardial potentials is formed. This forward transfer matrix obtains body surface potential recordings at 771 nodes on the body surface form epicardial potential measurements taken from 490 points on the heart surface.